NASA Research Announcement NNH06ZEA001N-SSRW2
Fundamental Aeronautics: Subsonic Rotary Wing Project 2

Texas Engineering Experiment Station Project # 32525/39600/ME
Prediction of Foil Bearing Performance: A Computational Model Anchored to Test Data

Thermohydrodynamic Analysis of Bump Type Gas Foil Bearings: A Model Anchored to Test Data

Final Project Report

Luis San Andrés

Mast-Childs Professor, Principal Investigator

Tae Ho Kim

Research Associate

Keun Ryu

Research Assistant

August 31, 2009

Texas A&M University
Mechanical Engineering Department
Turbomachinery Laboratory Tribology Group

NASA Agreement NNH06ZEA001N-SSRW2

Approved SOW – Main Objective

The objective of the proposed work is to develop a detailed, physics-based computational model of gas-lubricated foil journal bearings including thermal effects to predict bearing performance. The result of this work shall include a fully tested and experimentally verified design tool for predicting gas foil journal bearing torque, load, gas film thickness, pressure, flow field, temperature distribution, thermal deformation, foil deflections, stiffness, damping, and any other important parameters.

EXECUTIVE SUMMARY

Thermohydrodynamic Analysis of Bump Type Gas Foil Bearings: A Model Anchored to Test Data

Project Final Report
August 31, 2009
Luis San Andrés, Principal Investigator

The final report presents extensive measurements of bearing and rotor temperatures in the test rotor supported on Foster-Miller foil bearings. The test data, including rotordynamic measurements, aid to benchmark the computational physics based GFB predictive model. Demonstrated gas foil bearing (GFB) operation at high temperature is fundamental to enable implementation of these bearings into gas turbine applications. **Sections 1** and **2** of this Final report reproduce original research material released on the 7th Quarter report (May 2009).

In **Section 1,** tests on a hollow test rotor (1.1 kg, 38.1 mm OD, and 25.4 mm ID) supported on two GFBs, 2nd generation, are performed to evaluate the rotordynamic performance of the hot rotor-GFB system while operating at increasing shaft temperatures. While coasting down from 30 krpm to ~11 krpm, the rotor speed decays exponentially, as is typical in systems with viscous drag. As the rotor and bearing temperatures increase, the air becomes more viscous and the bearing clearances decrease; hence the coastdown time somewhat decreases. The temperatures on the bearing cartridges rise as the rotor temperature increases and also as the operating speed increases. At the hottest test condition, a forced cooling flow stream (at ~23ºC) significantly reduces the bearing temperatures. On the other hand, for operation at ambient or moderately low shaft temperature conditions, a cooling stream is of limited effectiveness. Thermal management with axial cooling streams is beneficial at high temperatures and with large flow rates ensuring turbulent flow conditions.

In **Section 2,** THD GFB model predictions reproduce with accuracy the recorded bearing temperatures. Operating conditions include increasing rotor speeds to 30 krpm, shaft OD hot temperature to 125 °C above ambient, and with increasing strength of cooling flow rates to 150 L/min into each test GFB. As the shaft temperature increases, the test foil bearing temperature increases accordingly. As the heater temperature increases, the journal attitude angle, drag

torque, peak film temperature, and shaft thermal growth increase, but the journal eccentricity decreases. The net-shaft thermal growth is most significant at the highest heater temperature and decreases the minimum film thickness at high rotor speeds, due to the reduction in the bearing operating clearance Note that the decrease in the bearing operating clearance reduces the bearing load capacity and increases the likelihood of thermal seizure and bearing failure.

A finite element (FE) model of the hot rotor supported on GFBs is developed in XLTRC^2 ©. An eigenvalue analysis predicts the system critical speeds and damping ratios for increasing shaft temperatures. In general, the rotor synchronous responses based on predicted linearized bearing coefficients show good agreement with test measurements during the rotor speed coastdown test. The rotor amplitude peak decreases and the system rigid-mode critical speed increases as the shaft temperature increases. The predicted rotor bending critical speed is above 28 krpm in reasonable agreement with the measurements.

In **Section 3,** static load tests to estimate the structural stiffness of two MiTi® FBs are detailed. Two configurations pairing the test rotor with a respective foil bearing, at the drive end or free end sides, show an actual clearance, i.e. the rotor OD is smaller than the FB top foil ID. A third configuration pairs a FB with a larger OD shaft resulting in an assembly interference. The static load measurements conducted at room temperature show different FB deflection versus load characteristics depending on whether the system has an actual clearance or a preload. The FB structural stiffness increases nonlinearly as the bearing deflection increases. Predictions of FB stiffness, derived from single bump stiffness formulas, agree very well with the measurements.

Presently, further rotordynamic performance and bearing/rotor temperature measurements in the test hot rotor supported on the MiTi® FBs are being performed. The measurement results will aid to determine experimental rotordynamic force coefficients for the test foil bearings. An upcoming technical report[1] will present further comparisons of measurements to predictions in order to further benchmark the computational GFB predictive model.

Appendices **A, B** and **C** reproduce material provided originally in the 1st, 2nd and 5th Quarter research progress reports, respectively. **Appendices A, B, C** and **J** detail the THD GFB model, numerical solution procedure, GFB temperature predictions compared against published test data, and predicted TAMU GFB force coefficients, respectively.

[1] Part of ongoing research funded by the Turbomachinery Research Consortium

Appendices D-I detail the characterization of the drive motor and flexible coupling and effectiveness of the cartridge heater in heating the test rotor.

Appendix K presents the THD GFB model predictions of the top foil temperature compared to published test data for various rotor speeds, static loads, and cooling flow rates.

Appendix L presents the measured shaft deflection versus static load corresponding to the foil bearing-shaft systems described in Section 3.

Appendix M details the list of components, and their cost, for the high temperature hollow rotor foil bearing test rig constructed during the life of the project.

The THD GFB software (2DXLGFBTH®) was delivered to Dr. Samuel Howard in June 2009. The delivery included FORTRAN sources and executable, MS Excel GUI, User manual, and examples.

TABLE OF CONTENTS

Thermohydrodynamic Analysis of Bump Type Gas Foil Bearings, Final Report

COMPLETED PLAN OF WORK AND ACCOMPLISHMENTS

Table A shows the approved work tasks and accomplished work during the 24 months of the project (8 Quarters). The hatched cells indicate work accomplished as planned, while the red arrows denote delays. The computational tool, benchmarked against laboratory test measurements, was delivered to the sponsor in June 2009.

Table A. Planned and accomplished work during life of project

Task	Q1	Q2	Q3	Q4	Q5	Q6	Q7	Q8
Computational analysis GFBS								
Development physical model for thermal transport in foil bearings								
Implementation thermal model (Finite Element Based) and coupling to existing STRUCTURAL MODEL								
Integration of thermal model with GFB FD computational code (gas film)								
Predictions of GFB performance for parametric studies								
Comparison of GFB predictions to measured performance from TAMU test rig								
Nonlinear analysis GFBS								
Development simple NONLINEAR physical model for foil bearings								
Prediction of performance and comparisons to available rotordynamic test data								
Test rig for identification of FB structure (High Temperature)								
Planning of modification, selection of instrumentation and cartridge heater, design of insulation cover								
Reception of parts and assembly of components, troubleshooting, connection to static loader and shaker								
Measurements of load & bearing deflection for increasing shaft temperatures (max 500 C), identification of FB structural parameters								
Rotordynamic-GFBs Test rig (High Temperature)								
Planning of modifications to existing, selection of instrumentation and cartridge heater, design of insulation cover and rotor								
Reception of parts and assembly of components, troubleshooting, connection to static loader and shaker								
Rotordynamic Measurements for increasing shaft temperatures (max 500 C), identification of GFB synchronous force coefficients								

Table B sums the major accomplishments of the project. The only delay relates to the measurement of rotordynamic responses in the test rig with Kololon™ coated MiTi foil bearings. This task will be accomplished in the next few months.

Table B. Major accomplishments of project

Task	Planned & Actual	comment
Thermohydrodynamic Analysis of GFBS		
Physical model for thermal transport in foil bearings. Integration of thermal model with GFB FD computational code (gas film). Prediction of GFB performance: parametric study	✓	Analysis completed. Code delivered on June 10, 2009
Validation of GFB predictions with measured temperatures from NASA & TAMU published research	✓	See Q4 & Q7 reports
Nonlinear structural analysis of GFBS		
Development simple NONLINEAR physical model for foil bearings. Prediction of performance and comparisons to rotordynamic test data	✓	Implementation in XLTRC2 for ready rotordynamic analyses
Test rig for identification of FB structure (High Temperature)		
Design & construction; selection & procurement of instrumentation and bearings; assembly, troubleshooting and operation at high temperature. Measurements of static load performance & comparison to predictions	✓	See Q4, Q7 reports
Rotordynamic-GFBs Test rig (High Temperature)		
Design & construction; selection & procurement of instrumentation and bearings; assembly, troubleshooting and operation at high temperature rotor-bearing test rig. Measurements of temperatures and rotordynamic performance with Foster-Miller GFBs completed (see Q7). Tests with MiTi® bearings at higher temperatures in progress. Validation of computational model also in progress.	✓ 85%	**In progress** – will complete by December 2009.

PUBLICATIONS FROM PROJECT

During the course of the sponsored research, the PI and students prepared seven quarter progress reports and the current final report. Table C shows other technical publications released to the Turbomachinery Research Consortium and several journal and conference (peer reviewed) archival publications. All references acknowledge the support of NASA NRA - Subsonic rotary Wing, SSRW2-1.3 Oil-Free Engine Technology (Foil Gas Bearing Modeling) Grant Cooperative Agreement NNX07P98A.

The table lists additional papers related to the project but not directly sponsored by NASA. More technical papers will be prepared in the future.

Table C. Other technical papers and reports prepared during project
(Quarterly progress reports not listed)

Journal	year	Title	Authors
ASME/STLE IJTC	**2009**	Experimental Structural Stiffness and Damping of a 2nd Generation Foil Bering for Increasing Shaft Temperatures	Luis San Andres, Keun Ryu
ASME Paper GT2008-59919 (accepted for ASME J of Eng for Gas Turbines and Power)	**2009**	**Thermohydrodynamic Analysis of Bump Type Gas Foil Bearings: A Model Anchored to Test Data**	Luis San Andres, Tae Ho Kim
ASME Paper GT2009-59920 (IGTI Education Committee)	**2009**	Gas Bearing Technology for Oil-Free Microturbomachinery – Research Experience for Undergraduate (REU) Program at Texas A&M University	Luis San Andres, Tae-Ho Kim, Keun Ryu, Thomas Chirathadam, Wayne Hung, Michael Johnson, Kat Hagen, Alejandro Martinez, Brain Rice, Nick Niedszwaki
American Helicopter Society 65th Annual Forum (submitted for review at ASME Journal of Tribology)	**2009**	Thermohydrodynamic Model Predictions and Performance Measurements of Bump-type Foil Bearing for Oil-Free Turboshaft Engines in Rotorcraft Propulsion Systems	Luis San Andres, Tae-Ho Kim, Keun Ryu

Publication	year	Title
Turbomachinery Research Consortium **TRC-B&C-2-09**	**2009**	Measurements of Rotordynamic Performance in a Hot Rotor-Gas Foil Bearing System
Turbomachinery Research Consortium **TRC-B&C-2-08**	2008	Thermohydrodynamic Analysis of Bump Type Gas Foil Bearings: Model and Predictions
Turbomachinery Research Consortium **TRC-B&C-2308**	2008	Rotordynamic Measurements on a High Temperature Rotor Supported on Gas Foil Bearings

Journal	year	Title
World Tribology Conference	**2009**	**Modeling of a Gas Foil Bearing for Microturbine Applications: Predictions versus Experimental Stiffness and Damping Force Coefficients**
ASME Paper GT2009-59315 (J)	**2009**	Measurements of Structural Stiffness and Damping Coefficients in a Metal Mesh Foil Bearing
American Helicopter Society 65th Annual Forum	**2009**	Measurements of Drag Torque, Lift-Off Journal Speed and Temperature in a Metal Mesh Foil Bearing
Tribology Transactions IJTC 2008-71195	**2009** **2008**	Effects of a Mechanical Preload on the Dynamic Force Response of Gas Foil Bearings - Measurements and Model Predictions
Tribology International	**2009**	Analysis of Gas Foil Bearings Integrating FE Top Foil Models
ASME Journal of Engineering for Gas Turbines and Power **ASME Paper GT2008-50571**	**2009** **2008**	**Effect of Side Pressurization on the Performance of Gas Foil Bearings – A Model Anchored to Test Data** **2008 Best PAPER Rotordynamics IGTI Structures and Dynamics Committee**
Tribology International	**2009**	Analysis of Gas Foil Bearings Integrating FE Top Foil Models
US-Korea Conference (UKC) 2008 on S, T & E	**2008**	Gas Foil Bearings for Oil-Free Microturbomachinery: Effect of Mechanical Preloads on the Rotordynamic Performance

PROPOSED BUDGET AND ACTUAL EXPENDITURES

Table D details the proposed budget and actual expenditures during the life of the project. At the end of the project there is only a few hundred dollars not spent. TEES will send a closing balance to NASA in a few weeks. Note that about $20k in equipment was purchased with TRC funds and donations from KIST and Honeywell Turbocharging Technologies.

Table D. Budget for project (proposed and actual expenditures)

ALL	08/27/07-08/26/09	
	Budget	Actual
Salaries & Wages	148,916	148,916
Travel	6252	6252
Capital equipment	33,445	33,445
Other equipment	5,182	5,060
Tuition & fees (F&A exempt)	17,835	17,835
F&A Cost	72,959	71,828
Total	284,588	280,973

No $$ left for salaries in AUGUST 09

TE09 Conference $2,363 encumbered

About $$ 20k purchased with TRC funds

See Appendix M for details on the cost of the instrumentation and equipment purchased for this project.

PERSONNEL WORKING IN PROJECT, QUARTER 8

Table E details the personnel working in the project during the last quarter (June 1, 2009 – August 26, 2009) and the responsibilities for each member of the research team. During the last quarter, project funds covered the salary of one graduate student (Keun Ryu) during two months only. TRC funds covered the salary of students C. Mao and K. Janica. The P.I did not have salary support from this project during the last quarter. On the other hand, NSF REUP supported generously two undergraduate students working with KIST foil bearings.

During the Summer REUP the students produced two research posters available upon request (files too long).

Table E. Research personnel and responsibilities in 8th Quarter
(June 1, 2009 – August 26, 2009)

Name	Position	Hours /week	Source of support	Description of duties
Luis San Andrés (H)	Principal Investigator	4	NASA	Oversees progress and provide guidance. Edits technical reports and papers. Verifies accuracy of predictions and other findings. Prepares final technical presentation and final report
Keun Ryu	Ph.D. student	20	NASA (100%)	Operates rotordynamic test rig and bearings. Oversees test cell and instructs other students
Chunliu Mao[F]	M.S. student	20	TRC	Measurements for identification of KIST bearings structural properties.
Katherine Janica[F]	Undergraduate Mechanical Engineering	20	TRC	Models nonlinear rotordynamics of simple foil bearings
José Camero[H]	Undergraduate Mechanical Engineering	40	NSF-REUP	UT-SanAntonio Torque during start up and shutdown with KIST foil bearings
Shane Muller	Undergraduate Mechanical Engineering	40	NSF-REUP	Calvin College. Structural stiffness and damping of KIST foil bearings

H: Hispanic, F: Female

CLOSING WORDS

The P.I., Dr. Tae-Ho Kim and Ph.D. student Keun Ryu thank NASA for the opportunity to conduct meaningful engineering research. The students and I delivered to the level expected and and even more. We strive *to do right the first time* and *do more with less.* We appreciate the leadership provided by Dr. Samuel Howard. Thanks to Dr. Chris DellaCorte for his interest in our work and his indefatigable efforts towards maturing the field of oil-free MTM.

Dr. San Andrés is presently on faculty development leave at the National University of Singapore. He is teaching a freshman seminar on modern engineering skills and practices and his traditional graduate class in modern lubrication. His duties at Texas A&M still form a major part of his overworked daily schedule.

Teaching freshman from a foreign cultural environment and educational background is proving to be a challenge. Hence, contrary to common perception, instead of having time to pursue gratifying intellectual pursuits, Dr. San Andrés is so far working two full time jobs. He expects his schedule to be less constraining with A&M duties in the next two months. Nonetheless, he is actually enjoying the challenges, in particular learning first-hand the cultural and educational differences between practices in the US and a fast changing Oriental world.

The P.I. looks forward to work with NASA in future developments encompassing, for example, advancing predictive modeling tools and performing tests with thrust foil bearings for oil-free MTM. The figure below shows an existing test rig constructed with Air Force funds under the USET (Upper Stage Engine Technology) Program. The program finished in August 2009. The test rig is available for further developments. When constructing the test rig, Dr. San Andrés had in mind its ulterior use as a thrust foil bearing test rig. For more information and detailed descriptions please request paper:

San Andrés, L., Phillips, S., and Childs, D., 2008, "Static Load Performance of a Hybrid Thrust Bearing: Measurement and Validation of Predictive Tool," 6th Modeling and Simulation Subcommittee / 4th Liquid Propulsion Subcommittee / 3rd Spacecraft Propulsion Subcommittee Joint Meeting. December 8-12, Orlando, Florida, JANNAF-120 Paper (Paper of restricted distribution – Joint Army, Navy, Nasa, Air Force Interagency Propulsion Committee)

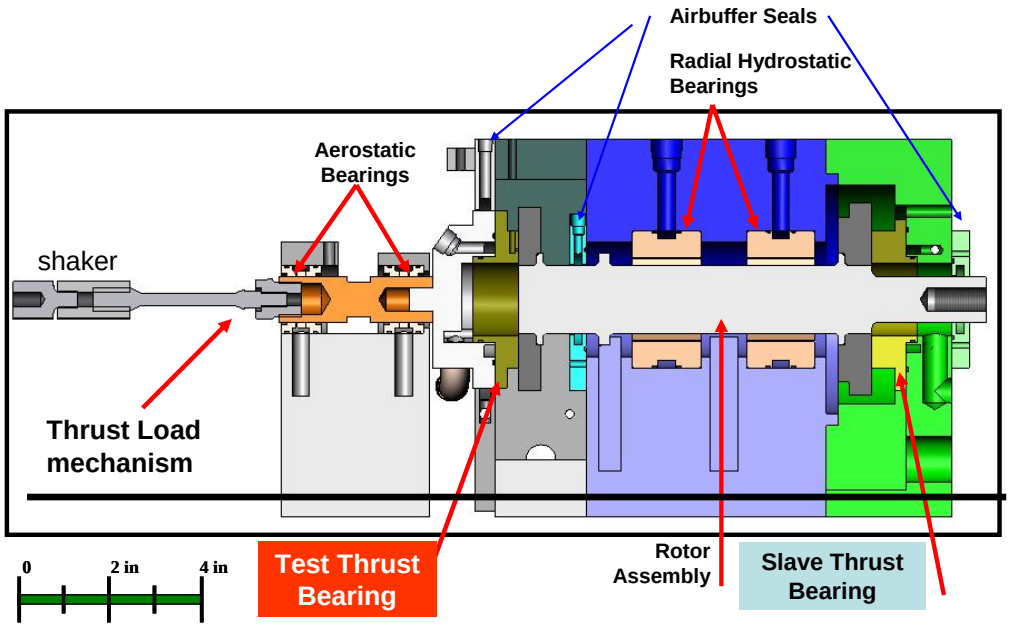

Test Fluids: **WATER, AIR**
0-50 krpm, 50-250 psi supply pressure,
Range of static + dynamic axial load: 1000 lbf, frequency range: 0-600 Hz
Cost estimated at $250k

Fig. 1. High speed, high pressure thrust bearing test rig at Texas A&M University

LIST OF TABLES

LIST OF FIGURES

SECTION 1.
MEASUREMENTS OF ROTORDYNAMIC PERFORMANCE IN A HOT ROTOR-GAS FOIL BEARING SYSTEM

By RA: Keun Ryu, Edited by P.I Luis San Andrés

INTRODUCTION

Gas foil bearings (GFBs) enable micro-turbomachinery (MTM) operating at extreme conditions in rotational speed and temperature. These are compact units with reduced maintenance costs and operating with better mechanical efficiency and improved reliability [1]. Gas foil bearings offer distinct advantages over rolling elements bearings including no *DN* value limit, reliable high temperature operation, and large tolerance to debris and rotor motions (rubbing and misalignment) [2]. Current applications, commercialized or under development, include aircraft gas turbine engines, auxiliary power units, microturbines, pumps, compressors, cryogenic turboexpanders, and turbochargers, for example [3].

However, GFBs have demerits of excessive power losses and wear of protective coatings during frequent rotor startup and shutdown events. In addition, expensive developmental costs and, until recently, inadequate predictive tools have restricted the widespread deployment of GFBs into gas turbines, for example. Particularly, at high temperature conditions, reliable operation of GFB supported rotor systems relies on adequate engineered thermal management. The heat conducted from a hot turbine, for example, degrades the material properties and changes the bearing operating clearance[1] [4,5]. A cooling gas flow aids to carry away heat and prevent GFBs from encountering thermal seizure, thus maintaining an adequate load capacity and thermal stability [6]. High temperature endurance with wear resistance using solid lubricant coatings on the shaft and/or the top foil surface further aids to prevent bearing failure [7].

Since 2003, the gas foil bearing research program at TAMU has advanced experimentally validated computational tools predicting the static and dynamic forced performance of GFBs in high-speed turbomachinery. References [8-12] detail the research progress to date. In 2008, Kim and San Andrés [13] detail rotordynamic measurements in a GFB test rig revamped for hot operation (max. heater temperature of 132ºC). An electric cartridge heater, rated at 250 W with

[1] An excessive decrease in the operating clearance of the bearings increases the bearing power loss and decreases the bearing load capacity.

120 V, loosely installed inside the hollow rotor acts as a heat source. The shaft temperature increases with the heater temperature. Without heating, rotor speed-up tests show an abrupt drop in rotor amplitude of motion just above its critical speed, thus demonstrating a nonlinear system forced response attributed to a strong hardening effect of the GFB elastic support structure. As the heater temperature increases, due to the increase in the gas viscosity, the rotor motion peak amplitude decreases dramatically without amplitude jump for operation above the critical speed. Rotor speed coastdown tests from 26 krpm show the system critical speed increases and the peak motion amplitude decreases significantly with shaft temperature. In spite of delivering large rates of cooling streams, up to ~56 L/min per bearing, the overall bearing temperature decreases just a few degrees (~5% less temperature that when operated without a cooling flow stream).

TAMU archival references [13-16] review past work, experimental and analytical, on the performance of GFBs operating at high temperature. This section presents further rotordynamic tests on a hot rotor-GFB system operating to 30 krpm. The cartridge heater operates at a larger temperature, up to 360 ºC. A mass flow meter (max. 500 L/min) measures the forced cooling air stream into the test bearings. Steady state tests at a fixed rotor speed quantify the effect of the cooling flow strength on the bearing and rotor temperatures. Rotor speed coastdown tests evidence the effect of shaft temperature on the rotordynamic performance of the GFB supported rotor.

EXPERIMENTAL FACILITY

The GFB rotordynamic test rig detailed in Refs. [10, 17] is revamped for operation at high rotor speeds (max. 50 krpm) and with shaft temperatures to a max. of 400ºC. Figure 1 depicts the current configuration of the GFB test rig and its instrumentation. A pair of GFBs, housed in a massive steel base, supports a hollow rotor. The 210 mm long AISI 4140 rotor, 1.064 kg in mass and 4.8 mm thick, has a nominal outer diameter of 38.07 mm at the bearing locations (at room temperature). A thin dense Chrome coating[2] (3 μm thick), withstanding up to 500ºC, covers the rotor at the bearing locations.

A slender rod at one end of the rotor and a flexible coupling connect the rotor to a drive motor. The drive electric motor has two electromagnetic poles to produce 9.5 kW at its maximum operating speed of 65 krpm using a supply voltage of 400~460 VAC (3 phase, 50-60

[2] Multichrome/Microplate Certified Processing Lab, Inc deposited the coating at no cost.

Hz). According to the electric motor performance map, the motor has a torque of ~85 N-cm at a low speed of 6 krpm. The flexible coupling (35 mm in length, 25 mm in outer diameter, and 5.08 mm inner diameter) consists of a steel bellow and aluminum clamping hubs. The coupling rated (maximum service) torque and torsional stiffness are 2.0 N-m and 1200 N-m/rad, respectively. Note that the maximum operating temperature of the inexpensive coupling is 120°C.

An electric cartridge heater, fitting loosely inside the hollow rotor, acts as a steady source of thermal energy to heat the test rotor-bearing system. The cartridge heater has a nominal diameter of 15.875 mm and overall length of 254 mm, and is rated at 1600 W when supplied with 240 VAC. Note that the heater does not warm evenly the rotor and test bearings, thus giving a significant axial temperature gradient along the rotor. See **Appendix F** for details.

An aluminum casing (7 mm thick) covers the whole test system and acts as a heat shield and safety enclosure to the test rig. Ceramic fiber paper (3.2 mm thick) insulates the inside walls of the casing. Fire-resistance mortar attaches the fiber paper to the casing walls. A gas flow meter, max. 500 L/min, records airflow streams into both foil bearings.

Figure 2 shows photographs of one of the test GFBs, 2nd generation, obtained from Foster-Miller Technologies. Table 1 lists the dimensions of the test bearings, each with uncoated top foil for high temperature operation. The test FB consists of a single arcuate top foil and five arcuate bump strip layers around the bearing circumference. Note that there are five other bump strip layers along the bearing axial length. Each bump strip, with five bumps, is spot welded at one end, and free at the other and. A bump strip spans 72° around the inner circumference of the bearing cartridge. The top foil is a conformed thin metal sheet welded to the bearing sleeve at one end, and free at the other end. The total number of bumps equals 125, i.e. 25 in the circumference of the bearing times 5 along its axial plane. The bearing cartridge is made of AISI 304 stainless steel, and the bump foils and top foils are made of Cr-Mb steel.

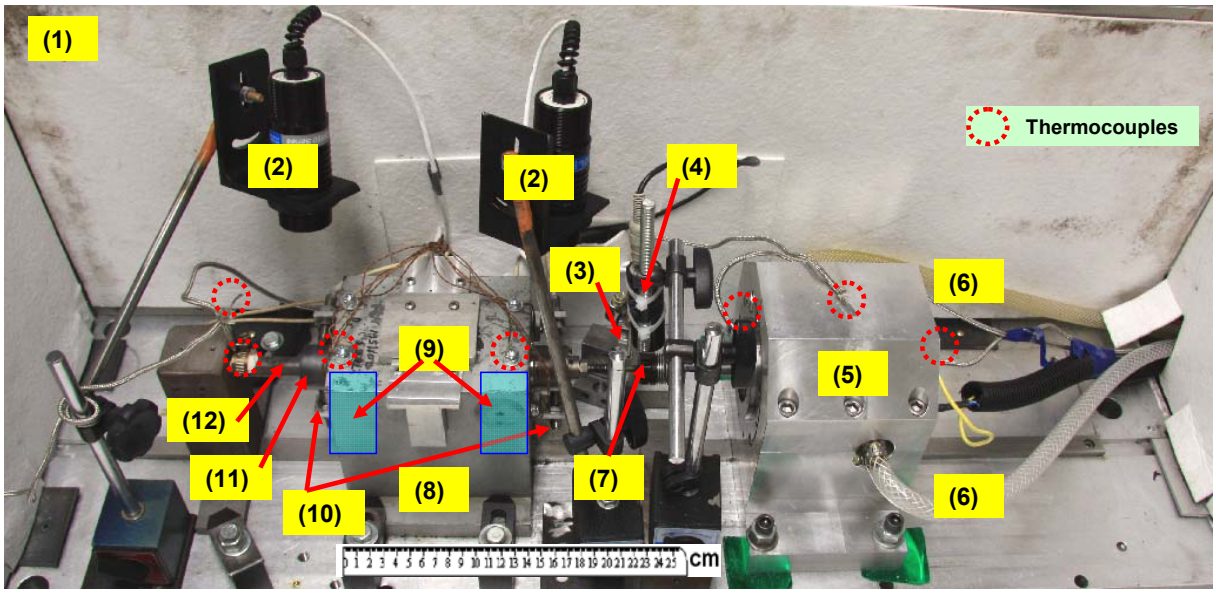

(1) Insulated safety cover
(2) Infrared thermometer
(3) Flexible coupling cooling air supply
(4) Infrared Tachometer
(5) Drive motor
(6) Motor cooling water supply
(7) Flexible coupling
(8) GFB support housing
(9) Test GFBs
(10) Displacement sensors
(11) Test hollow shaft
(12) Cartridge heater

(a) Major components and instrumentation

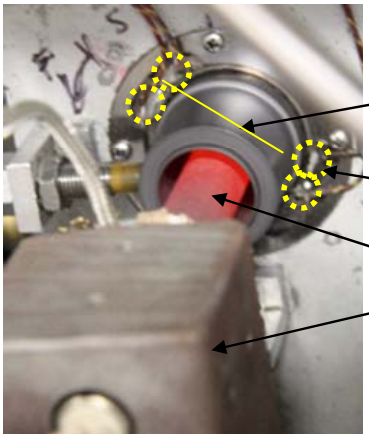

(b) Hot cartridge heater (T_{hs}=360ºC) and rotor spinning at 30 krpm

Fig. 1 Photograph of high temperature GFB rotordynamic test rig. (a) Major components and instrumentation, (b) Hot cartridge heater at 360ºC and rotor spinning at 30 krpm.

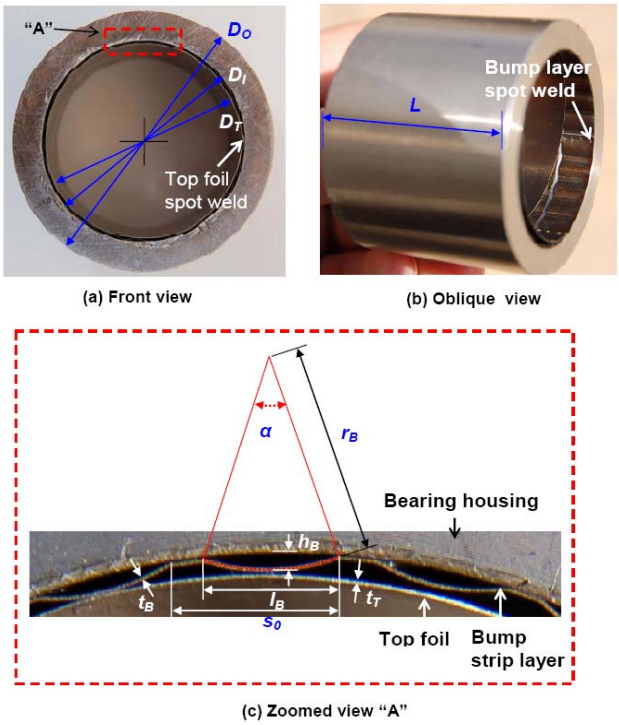

Fig. 2 Photograph of 2nd generation bump type test GFB with uncoated top foil and its dimensions. Taken from Ref. [13]

Table 1. Test foil bearing nominal dimensions (Unit: mm) [13]

Parameters	Drive end (DE) GFB	Free end (FE) GFB
Bearing cartridge outer diameter, D_O	50.85	50.82
Bearing cartridge wall thickness, t_{BC}	5.746	5.776
Bearing cartridge inner diameter, $D_I = D_O - 2\ t_{BC}$	39.36	39.27
Bearing axial length, L	38.2	38.14
(bare top foil) Top foil thickness, t_T	0.10	0.10
Bump foil thickness, t_B	0.10	0.10
Number of Bumps, N_B	25	25
Bump pitch, s_0 (deg)	4.581 (13)	4.581 (13)
Bump length, l_B	3.742	3.742
Bump height, h_B	0.468	0.468
Bump arc radius, r_B	5.581	5.581
Bump arc angle, α (deg)	36.5	36.5
Top foil inner diameter, $D_T = D_I - 2(t_T + h_B)$.	38.190	38.135
Poisson's Ratio	0.29	0.29
Modulus of Elasticity (GPa)	213736	213736

1) Manufacturer: Foster-Miller Technologies
2) Material: Cr-Mb steel (bump strip and top foil), AISI 304 stainless steel (bearing cartridge)

Infrared thermometers measure the rotor surface temperatures at each end of the test rotor. The uncertainty and response time of the transmitter are 1.7°C (3°F) and 250 ms, respectively. Note that the sensor has an adjustable emissivity setting.

Two pairs of eddy current sensors (Bently Nevada 7200 Series), orthogonally positioned and facing the rotor ends, measure lateral displacements of the test rotor along the vertical and horizontal planes. Table 2 shows the calibrated sensitivity of the eddy current sensors installed. An infrared tachometer, mounted on the test table and targeting one end of the flexible coupling, is a keyphasor signal for data acquisition.

Table 2 List of sensors gains

Name	**Location**	Sensitivity	**Unit**
Displacement eddy current sensors	Drive end, vertical direction (DV)	7.97	mV/μm
	Drive end, horizontal direction (DH)	8.31	mV/μm
	Free end, vertical direction (FV)	8.04	mV/μm
	Free end, horizontal direction (FH)	8.06	mV/μm

Commercial DAQ systems (*Bentley Nevada ADRE® for Windows* and *LabVIEW®*) collect and record the test data from coast down rotor speed experiments. Table 2 shows the sampling size and acquisition rate of the *ADRE®* DAQ system.. The sampling size and rate for *LabVIEW®* are 2048 (2^{11}) and 10,000 samples/sec, respectively. A custom *LabVIEW®* graphical user interface (GUI) shows both time domain and frequency-domain representations of each signal during real time monitoring and data logging. A two-channel dynamic signal analyzer displays the frequency content of selected motion signals.

Appendix N details the components of the test rig, including commercial designations, their cost and assigned source for payment.

EXPERIMENTAL PROCEDURE

Figure 3 shows a schematic view of the high temperature GFB rotordynamic test rig with the cartridge heater and temperature measurement locations of the test rig components: T_1~T_{16}, T_{amb} and T_h. Recall that the electric heater is inserted loosely into the hollow portion of the shaft. The radial gap between these two components is 4.75mm.

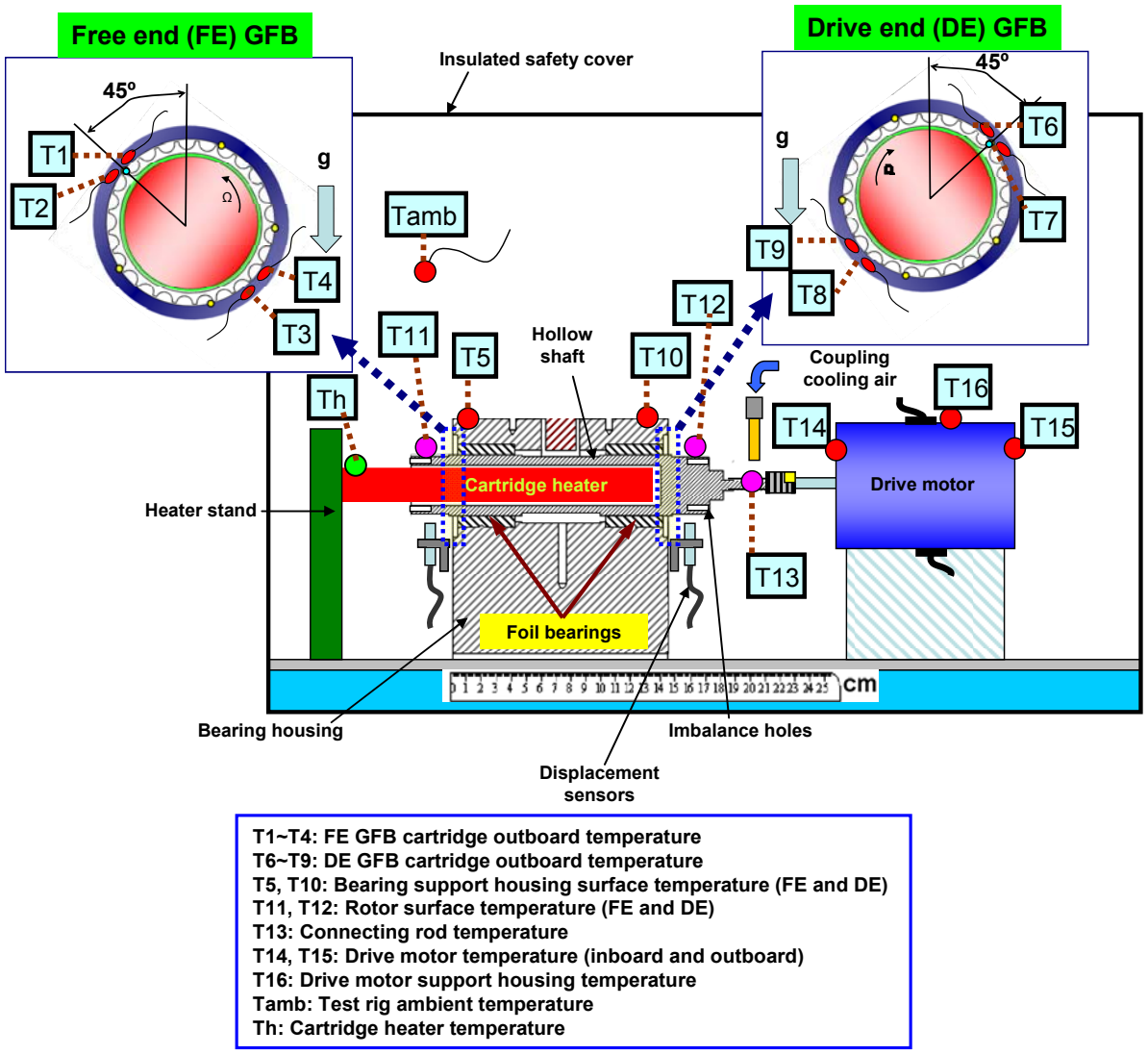

Fig. 3 Schematic view of GFB rotordynamic test rig with cartridge heater. T_1~T_{16}, T_{amb}, T_h represent locations of temperature measurement.

Table 3 presents the matrix of test conditions for increasing heater set temperatures (T_{hs}=100º, 200º, 300º, and 360ºC), without and with increasing axial cooling air flow rates (100, 200, and 300 L/min). Note that the flow rates quoted distribute (evenly) into the two bearings, drive end (DE) and free end (FE), thereby supplying 50, 100, and 150 L/min per each bearing.

Table 3 also lists the time elapsed for the (whole) test rig to reach thermal equilibrium, i.e. temperatures in the components not changing any longer with time (steady state). For test conditions 4 through 12, the sides of the (insulating) enclosure remain open to reduce the operating time for thermal equilibrium condition of the test system and to minimize thermal induced damage of the instrumentation and drive motor.

Table 3 Matrix of experimental test conditions in high temperature GFB rotordynamic test rig[3]

Test condition #		Rotor speed condition	Imbalance conditions	Axial cooling flow conditions*	Heater set temperature conditions	Test hours	Rig enclosure
Cond. 1	Rotor imbalance response measurement test (**Room temperature**)	Fixed speed of 0, 10, 15, 20, 25, 30 krpm	Baseline	No cooling	No heating	9h 9'	Closed
Cond. 2				100L/min		5h 52'	
Cond. 3		Coast down from 30 krpm	Baseline	No cooling		5 '	
			60mg in phase				
			110mg in phase				
			184mg in phase				
Cond. 4	Rotor imbalance response test (**High temperature**)	Coast down from 30 krpm	Baseline	No cooling	No heating	1h 15'	Open
					100ºC	1h 37'	
					200ºC	1h 40'	
					300ºC	1h 32'	
					360ºC	1h 35'	
Cond. 5			60mg in phase		No heating	1h 37'	
					100ºC	1h 41'	
					200ºC	1h 24'	
					300ºC	1h 21'	
					360ºC	1h 30'	
Cond. 6			110mg in phase		No heating	1h 38'	
					100ºC	1h 48'	
					200ºC	1h 40'	
					300ºC	1h 50'	
					360ºC	1h 41'	
Cond. 7	Temperature measurement for **increasing rotor speed**	Fixed rotor speed of 10, 20, 30 krpm	Baseline	No cooling	No heating	1h	
Cond. 8				100L/min			
Cond. 9	Temperature measurement for **increasing heater temperature**	Fixed rotor speed of 30 krpm		No cooling	No heating, 100, 200, 300, 360ºC		
Cond. 10				100L/min			
Cond. 11				200L/min	No heating, 100, 200 ºC		
Cond. 12				300L/min	No heating, 100, 165ºC		

(*) Total flow splits in ½ into each foil bearing

In the experiments, the rotor speed reaches a maximum of 30 krpm. Over the speed range (2-30 krpm), the test rotor is not regarded as a rigid body. Details on the natural frequencies and mode shapes of the test rotor-bearing system follow later.

For **test conditions 3, 5 and 6,** added masses (m_i) are inserted in the holes located at the rotor ends and at a radial distance (r) of 15.11 mm. The imbalance displacement (u), i.e. distance from rotor center of mass, is

$$u = \frac{m_i r}{m_i + M_{DE\ or\ FE}} \tag{1}$$

[3] Prior to each test condition, the whole rotor-bearing system is at room temperature, i.e., the drive motor and cartridge heater are turned off for ~ 24 hours.

where M_{DE} and M_{FE} are fractions of the test rotor weight acting on each bearing: M_{DE} =0.698 kg (6.844 N) and M_{FE} =0.366 kg (3.589 N), respectively[4]. Table 4 shows the imbalance mass and its location, as well as the displacements u for each condition. The imbalance masses are positioned at the same angular location at each rotor end, i.e., in phase imbalance condition.

Table 4. Imbalance mass magnitudes and location

Imbalance name (In phase)	Mass m_i (g)[5]		Displacement u (μm)	
	Drive end (-22º)	Free end (-22º)	Drive end	Free end
U_1	0.060	0.060	1.30	2.48
U_2	0.110	0.110	2.38	4.54
U_3	0.184	0.184	3.98	7.60

Over the whole set of test conditions, while the rotor operates, a stream of compressed shop air (20 psig, 23ºC) cools the flexible coupling[6] through a plastic hose and nozzle. In the following, the designations DV and DH correspond to the rotor responses at the drive end bearing side, vertical and horizontal plane, respectively. The same notation follows for the free end bearing, FV and FH.

EXPERIMENTAL RESULTS

Verification of rotor-bearing system response linearity: Test condition 3.

Test condition # 3	Rotor speed condition	Imbalance conditions	Axial cooling flow conditions	Heater set temperature conditions	Test time	Rig enclosure
Rotor imbalance response measurement test (**Room temperature**)	Coast down from 30 krpm	Baseline	No cooling	No heating	5'	Closed

For test condition 3 (without heating and forced cooling), rotor speed coast down measurements from 30 krpm are conducted with the rotor at its baseline condition and with added imbalance masses. Figure 4 shows the normalized rotor amplitudes of the measured

[4] The force acting on the flexible coupling is not considered for the static load distribution.
[5] Uncertainty in mass is ±0.001g
[6] The flexible coupling consists of a steel bellow and aluminum clamping hubs. The coefficient of thermal expansion of aluminum (coupling clamp hub material) and Inconel 718 (rotor material) are 24.0 μm/m°C and 13.0 μm/m°C, respectively [18]. Hence, temperature management of the coupling is mandatory for high temperature operation.

synchronous responses. In the figures, the baseline response is subtracted (amplitude and phase) from the measured imbalance response and normalized by multiplying the ratio of the added mass $U_{2 \text{ or } 3}/U_1$. In this manner, the linearity of the test rotor-GFBs system response can be easily verified.

The three response curves in Figure 4 are nearly identical, thus denoting the rotor amplitude of synchronous response is proportional to the added mass imbalance. This implies that a rotordynamic model that integrates linearized GFB force coefficients will predict the rotor behavior correctly. The speeds at which discernible rotor response amplitude peaks at the DH and FH are 13.4 krpm and 12 kprm, respectively.

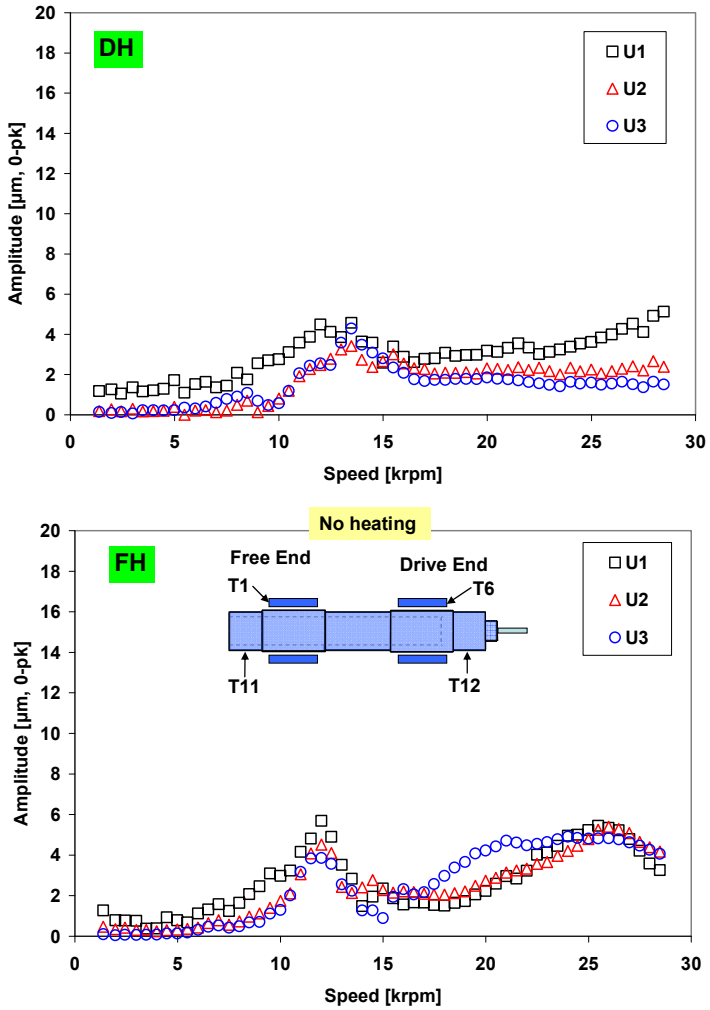

Fig. 4 Test condition 3: Normalized amplitude of synchronous response for in-phase imbalance masses of 60mg (U1), 110mg (U2), and 184mg (U3). Measurements at rotor drive end horizontal (DH) and rotor free end horizontal (FH) planes with baseline subtraction.

Effect of shaft temperature on rotordynamic performance of GFB supported rotor: Test conditions 4-6

Test condition #		Rotor speed condition	Imbalance conditions	Axial cooling flow conditions	Heater set temperature conditions	Test hours	Rig enclosure
Cond. 4	Rotor imbalance response test (**High temperature**)	Coast down from 30 krpm	Baseline	No cooling	No heating	1h 15'	Open
					100ºC	1h 37'	
					200ºC	1h 40'	
					300ºC	1h 32'	
					360ºC	1h 35'	
Cond. 5	Rotor imbalance response test (**High temperature**)	Coast down from 30 krpm	60mg in phase	No cooling	No heating	1h 37'	
					100ºC	1h 41'	
					200ºC	1h 24'	
					300ºC	1h 21'	
					360ºC	1h 30'	
Cond. 6	Rotor imbalance response test (**High temperature**)	Coast down from 30 krpm	110mg in phase	No cooling	No heating	1h 38'	
					100ºC	1h 48'	
					200ºC	1h 40'	
					300ºC	1h 50'	
					360ºC	1h 41'	

For test condition 4, Fig. 5 depicts the recorded amplitudes of synchronous rotor response during a rotor speed coastdown test from 30 krpm. Slow roll compensation is at 2 krpm[7]. This response is regarded as baseline since it does not include any added imbalance mass. The rotor amplitudes are well damped at speeds around the system first critical speed region (11~13 krpm), gradually increasing as the rotor speed approaches 30 krpm. Rap tests demonstrate the flexible mode natural frequency of the test system at 29 krpm (480 Hz). Multiple peaks in rotor synchronous responses are evident and reveal the different forced response characteristics along the vertical and horizontal directions. There are no noticeable differences in rotor responses for both the shaft without heating and with heater at T_{hs}=360ºC conditions. The figures show insets denoting the measured rotor end temperatures. Note in particular the large axial thermal gradient (~50ºC) for the hot rotor condition.

[7] The slow roll speed is typically less than 10% of the full operating speed of the rotor [19].

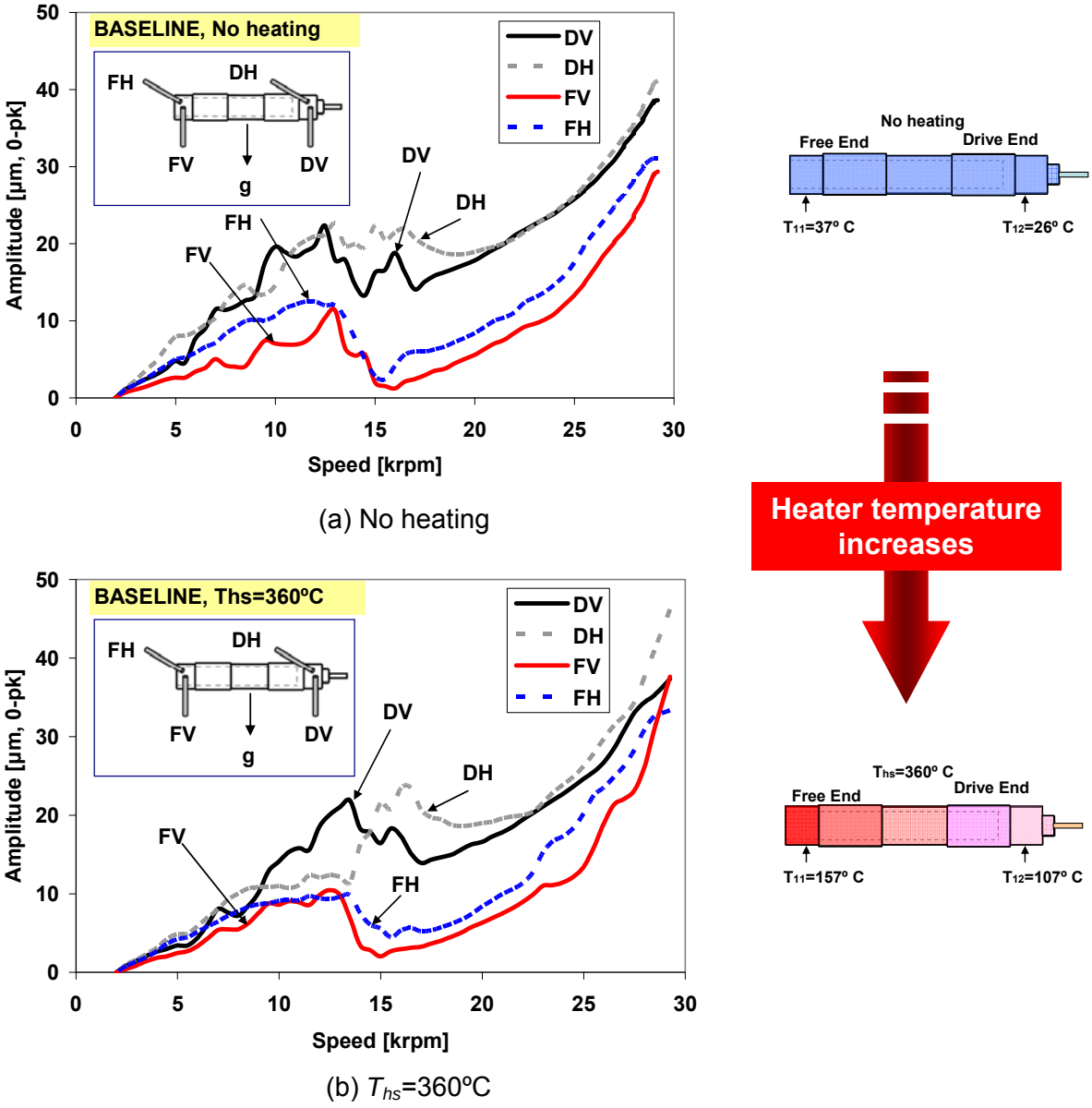

(a) No heating

(b) T_{hs}=360°C

Fig. 5 Test condition 4: Amplitude of rotor synchronous response versus rotor speed. Slow roll compensation at 2 krpm. No axial cooling flow into bearings. Baseline imbalance. Tests at room temperature and with heater at T_{hs}=360°C.

The mode shape of the rotor response can be readily determined by subtracting the phase angles of the measure motions at the drive and free end of the rotor. Note that the rotor is rigid at low speeds, below 15 krpm. On the other hand, as the speed increases beyond 20 krpm, the rotor shows a distinctive flexural mode due to the softness of the coupling and connecting rod. For test condition 4 (without shaft heating), Fig. 6 depicts the phase angle difference (∠FH - ∠DH) ~180° denoting a conical mode at speeds around the system first critical speed range, 11~13 krpm. Note

that this phase difference abruptly drops at ~15 krpm and ranges between 110º and 180º at 15~10 krpm. The figure also displays the ratio of amplitudes (drive end/free end) of the rotor. This ratio determines the relative amplitude of the major amplitude rotor (end) motion at the measurement locations. The rotor moves in a conical mode shape at speeds below 13 krpm. In particular, when the rotor operates between 15 and 20 krpm, the overall amplitude of rotor motion at the drive end rotor is 2~9 times larger than those at free end rotor.

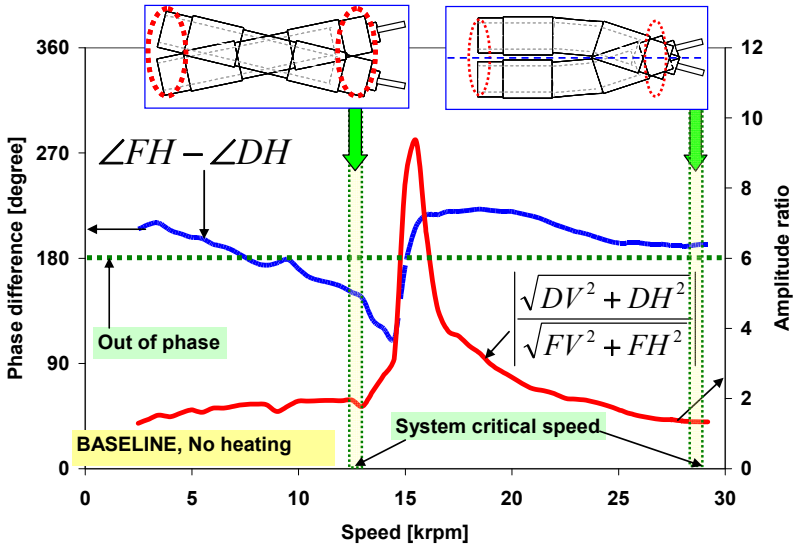

Fig. 6 Test condition 4: Phase difference ($\angle FH - \angle DH$) and major amplitude ratio ($\left|\sqrt{DV^2+DH^2}/\sqrt{FV^2+FH^2}\right|$) of recorded imbalance response. No rotor heating. No axial cooling flow into bearings. Baseline imbalance.

For operation at four heater set temperatures (T_{hs}=100º, 200º, 300º, 360ºC) and also while at room temperature (heater off), equivalent to test condition 4, Fig. 7 depicts the synchronous rotor amplitude and lag phase angles recorded during rotor speed coastdown tests. Recall that no cooling flow is supplied. In general, as T_{hs} increases to 360ºC, the peak amplitudes[8] between 7~15 krpm decrease significantly. The phase angles, over the whole speed range, slightly decrease with increasing heater temperatures. Recall that thermally induced mechanical changes in the shaft and bearing can noticeably affect the operating clearance and gas film properties in GFBs [11]. Note the phase angle ranges 0~360º since the test rotor-bearing system crosses two

[8] Note that the displacement peak amplitude is not evident (multiple peaks as well as a too broad band due to high damping) to identify a *true* system critical speed.

natural modes, rigid and flexural. The figure shows insets denoting the measured rotor end temperatures.

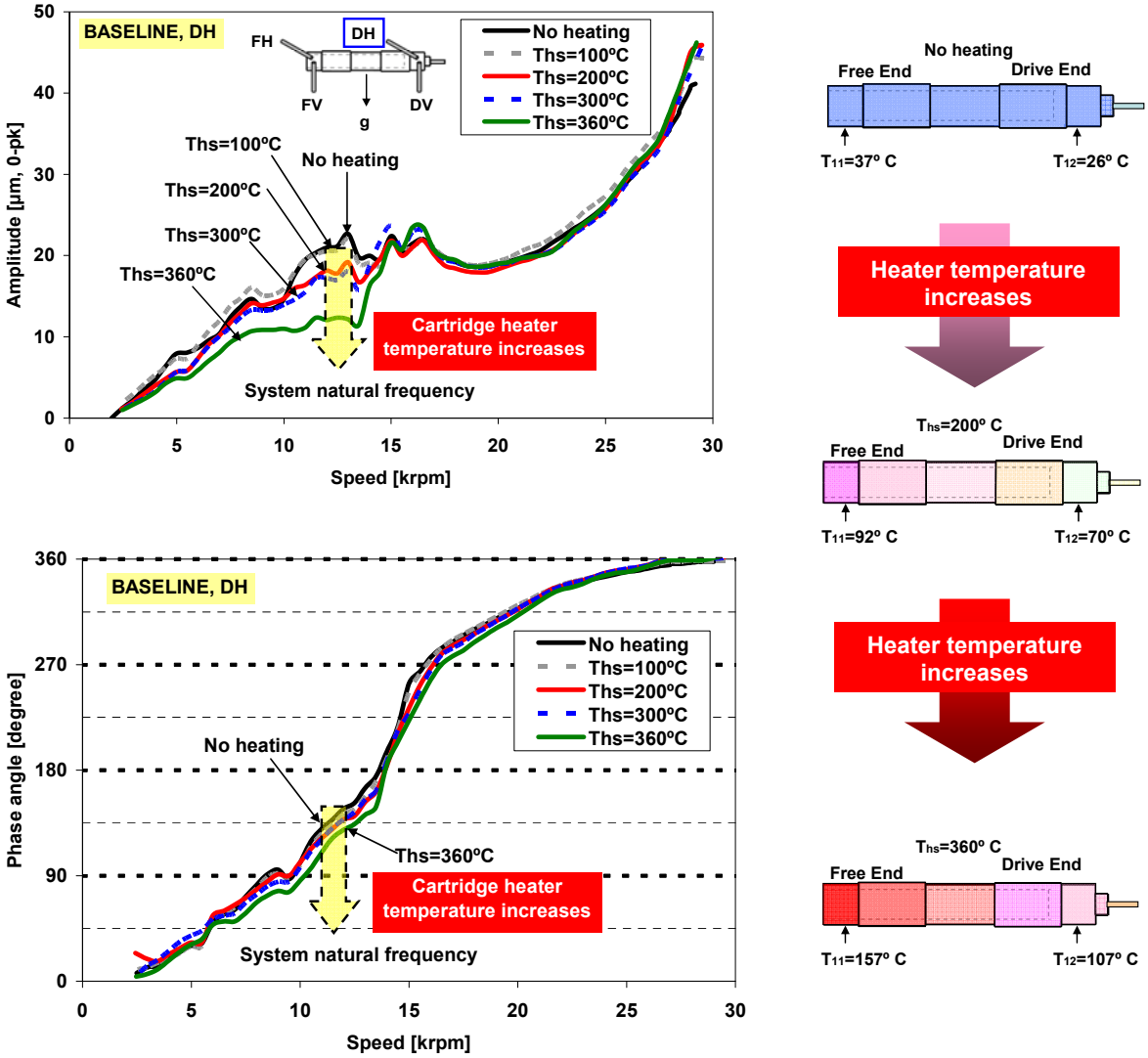

Fig. 7 Test condition 4. Effect of shaft temperature on rotor response: Rotor amplitude and lag phase angle of synchronous response for four cartridge heater set temperatures (T_{hs}). No axial cooling flow into bearings. Slow roll compensation at 2 krpm. Baseline imbalance. Rotor drive end, horizontal plane (DH).

Figure 8 shows waterfall plots depicting the amplitude and frequency contents (1X and 2X) of the rotor motions as the rotor coast downs from 30 krpm. The measurement corresponds to test condition 4, i.e., baseline without axial forced cooling into the bearings. Note that, for all test conditions, no subsynchronous whirl motions appear over the whole speed range. From the top

speed to ~16 krpm, there is dominance of synchronous rotor motions and small amplitude super-synchronous frequencies (2X and 3X).

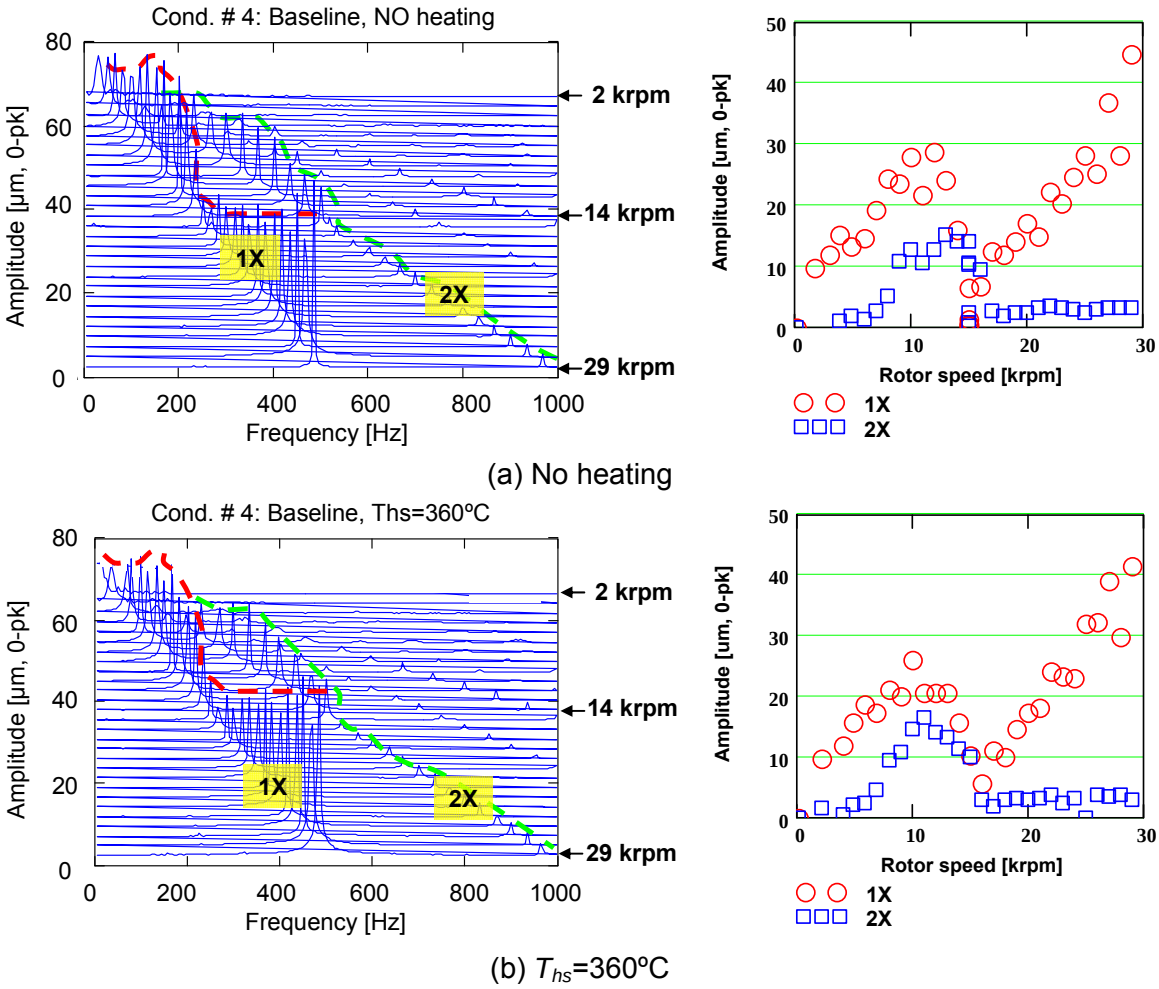

Fig. 8 Test condition 4: Waterfalls and amplitude of synchronous (1X) and 2X rotor motions. Uncompensated amplitudes of motion. Rotor drive end, horizontal plane (DH). Tests w/o heating and with heating at T_{hs}=360ºC

Figure 9 shows the synchronous (1X) rotor orbits at rotor speeds equal to 5, 10, 15, 20 krpm for test condition 4 (no axial cooling streams). Recall that the orbit represents the path of the shaft centerline relative to a pair of orthogonally mounted displacement sensors [20]. In the figure, the blank/dot sequence on each orbit represents a keyphasor mark which shows the location of the shaft centerline at the instant when the reflective mark (once-per-revolution mark) passes the keyphasor probe (tachometer). The keyphasor mark in an orbit curve aids to determine the instantaneous direction of rotor motion (CCW direction in Fig. 9) and to estimate the

absolute phase; and with multiple orbit plots, the mode shape of the rotor [21]. Note that the orbits w/o heating and with heater at T_{hs}=360ºC are almost identical at similar shaft speeds. The ellipticity of the orbital motion shows the anisotropic character of the foil bearing stiffnesses. The 1X orbits are nearly circular at rotor speed above 20 krpm. Note the keyphasor marks imply out of phase motions between the drive end and free end of the rotor over the entire speed range.

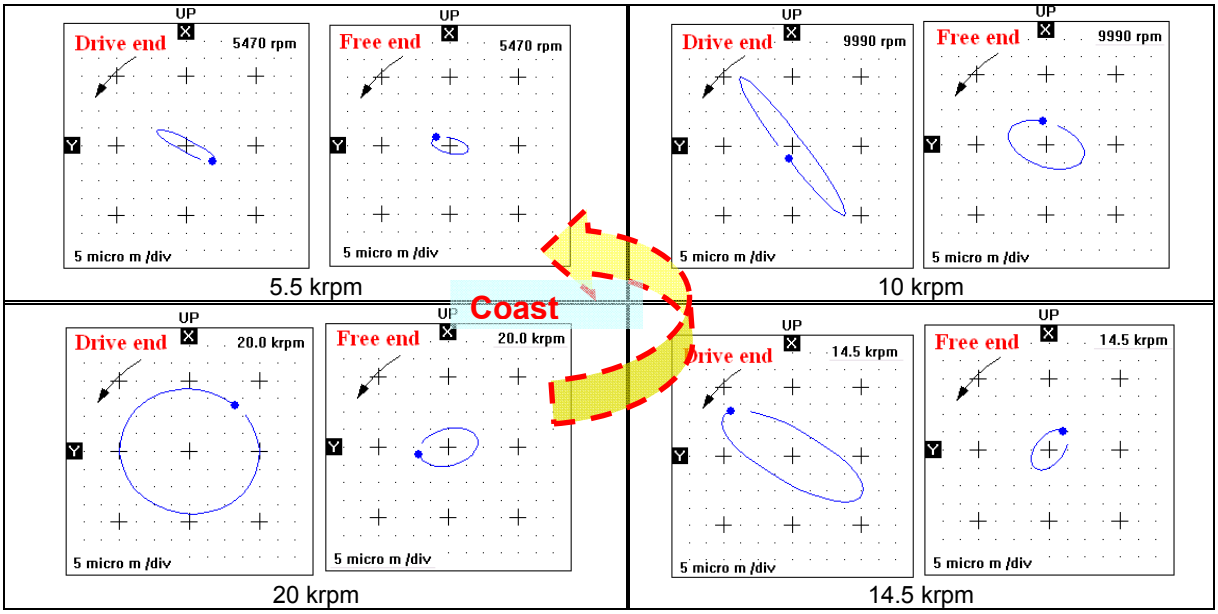

(a) No heating

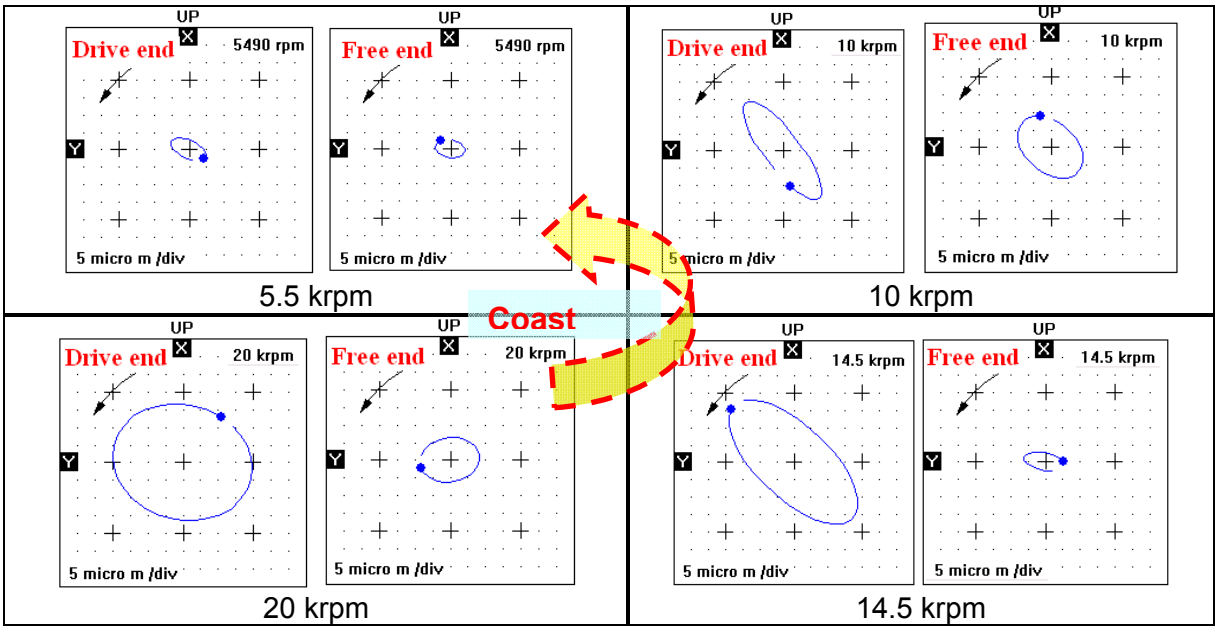

(b) T_{hs}=360ºC

Fig. 9 Test condition 4: Synchronous speed rotor orbits. (a) no heating (heater off), and (b) heater at T_{hs}=360ºC. Slow roll compensated at 2 krpm.

While coasting down from a top speed of 30 krpm to rest, Fig. 10 depicts the recorded coastdown rotor speed versus time at increasing heater temperatures for test condition 4. The time for the rotor to coast down is over 50 seconds which denotes very low air drag operation (nearly friction free). The results reveal an exponential decay of rotor speed with time for speeds from 30 krpm to ~11 krpm. Then, the rotor rapidly decelerates to rest, thereby evidencing rubbing (dry friction effects) in the rotor-bearing operation. The calculated (correlation coefficient) R^2 of both exponential and linear decays in the figure renders a goodness of correlation of 99%. Exponential decay in a speed coastdown curve is typical of a rotating system with viscous drag, and hence demonstrates no contact between the rotor and the bearing surfaces. For speeds below ~11 krpm, the rotor speed decays nearly linearly, typical of mixed drag conditions, i.e., viscous and with dry-friction. The overall coast down time reduces noticeably as the rotor becomes hot. For example, the overall coast down time for T_{hs}=360ºC is ~10 second shorter than that for the *no heating* (heater off) tests (16% decrease in overall coastdown time). As the rotor temperature increase, the rotor touchdown speed (transition from viscous drag to dry friction) also decreases.

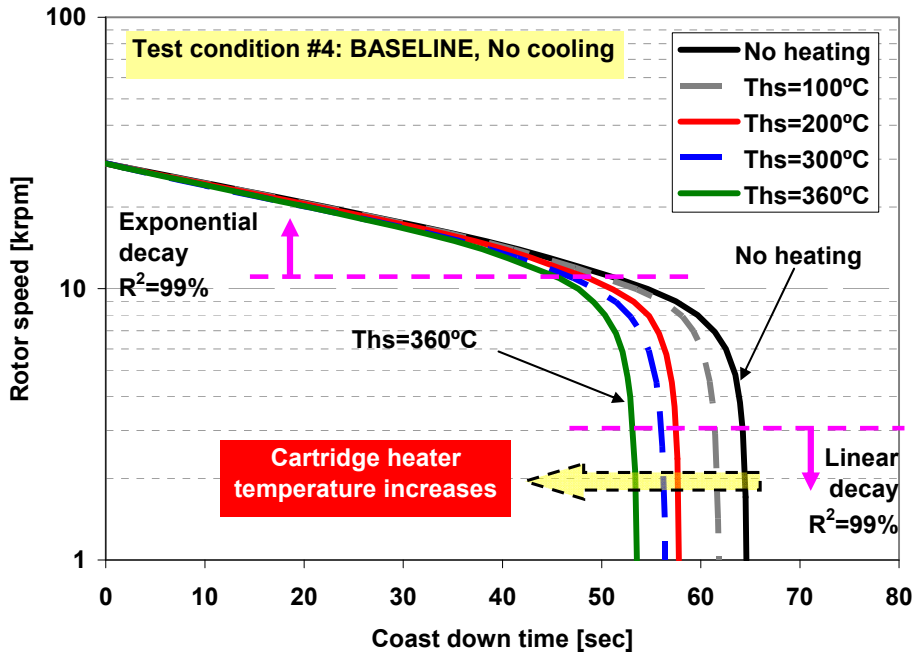

Fig. 10 Test condition 4. Effect of shaft temperature on time extent for speed coastdown: Tests with increasing heater temperatures. Baseline imbalance.

Effect of rotor speed on rotor and GFB temperatures: Test conditions 7 and 8 (operation at ambient temperature)

Test condition #		Rotor speed condition	Imbalance conditions	Axial cooling flow conditions	Heater set temperature conditions	Test hours	Rig enclosure
Cond. 7	Temperature measurement for **increasing rotor speed**	Fixed rotor speed of 10, 20, 29.3 krpm	Baseline	No cooling	No heating	1 h	Open
Cond. 8				100L/min			

In test conditions 7 and 8 (with electrical heater off), the bearing and rotor temperatures are recorded while the rotor operates at a constant speed (10, 20 and 30 krpm). The tests correspond to conditions without and with forced axial cooling flow (50 L/min per bearing). The ambient temperature is $T_a \sim 21$ºC.

In the tests, after 20 minute intervals, the rotor speed is set at 10 krpm, then at 20 krpm, and finally at 29.3 krpm. The temperatures shown below represent thermal steady state conditions. The total experiment lasts 60 minutes (1 hour). Figure 11 shows the temperature raise of the free end (FE) and drive end (DE) rotor surfaces (T_{11} and T_{12}) and the FE and DE bearing cartridges (T_1 and T_6) versus test elapsed time. See Fig. 3 for designation of thermocouples. The recorded bearing cartridge and rotor surface temperatures steadily increase with operating time. For operation without or with 50 L/min axial cooling, the temperatures of the FE and DE bearing cartridges (T_1 and T_6) are almost identical. Note that the free end rotor surface (T_{11}) shows the largest temperature raise as operation time and rotor speed increase.

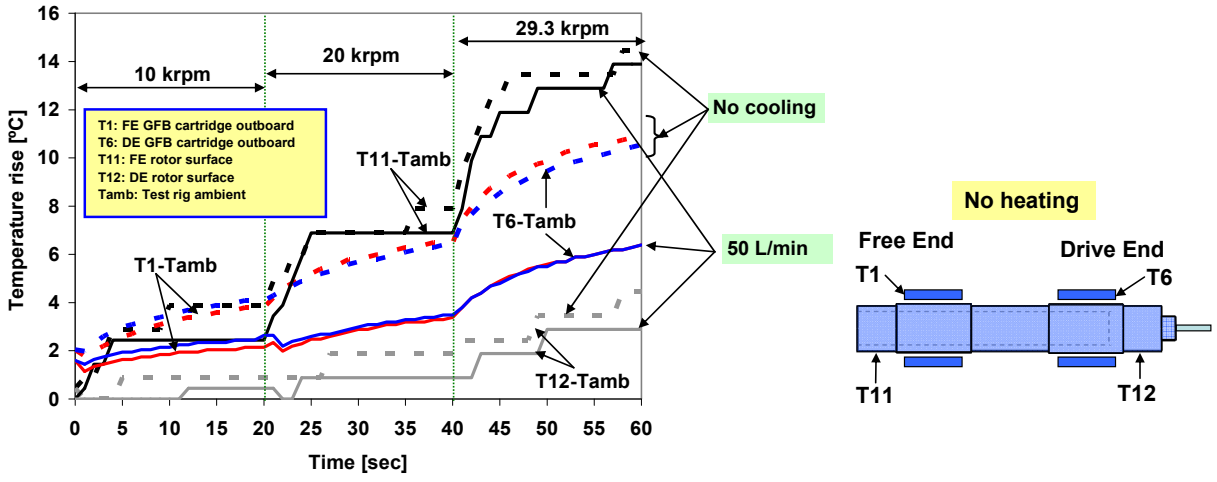

Fig. 11 Test conditions 7 and 8: Temperature raises in FE and DE FB cartridges, T_1-T_{amb} and T_6-T_{amb}, and FE and DE shaft surface, T_{11}-T_{amb} and T_{12}-T_{amb}, versus rotor speed. Operation at ambient condition, T_{amb} =21ºC. Without and with 50 L/min cooling stream into each bearing.

Figure 12 shows the temperature raise on the FE and DE GFB cartridges, (T_1-T_{amb}) and (T_6-T_{amb}), versus rotor speed. See Fig. 3 for the locations of the thermocouples. The bearing cartridge and rotor surface temperatures increase as the rotor speed increases. The forced axial cooling flow produces an effective decrease in bearing temperatures. At 29.3 krpm, the bearing cartridge temperature with 50 LPM cooling reduces the overall temperature as much as 5ºC (a drop of 44% in temperature raise when compared to the no cooling condition). Note, however, the insignificant effect of cooling flow on the rotor surface temperature, irrespective of shaft speed (only ~1ºC decrease). The paramount effect of the cooling flow stream in the bearings is distinct at the highest rotor speed, ~30 krpm. More discussion of the effect of forced axial cooling follows later.

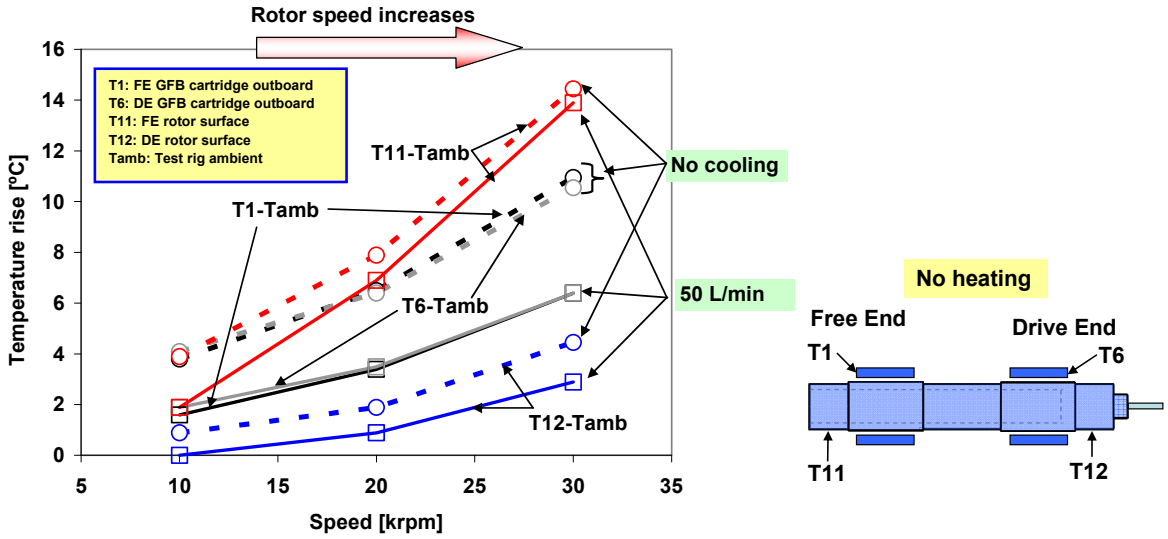

Fig. 12 Test conditions 7 and 8. Effect of rotor speed on bearing temperature raise: Temperature raise in FE and DE FB cartridges, T_1-T_{amb} and T_6-T_{amb}, and FE and DE shaft surface, T_{11}-T_{amb} and T_{12}-T_{amb}, versus rotor speed. Operation at ambient condition, T_{amb}=21ºC. With 50 L/min and without cooling stream to each bearing.

Effect of shaft temperature and strength of cooling flow on rotor and GFB temperatures: Test conditions 9-12

Test condition #		Rotor speed condition	Imbalance conditions	Axial cooling flow conditions	Heater set temperature conditions	Test hours	Rig enclosure
Cond. 9	Temperature measurement for **increasing heater temperature**	Fixed rotor speed 29.3 krpm	Baseline	No cooling	No heating, 100, 200, 300, 360ºC	1 h	Open
Cond. 10				100L/min			
Cond. 11		Fixed rotor speed 29.3 krpm		200L/min	No heating, 100, 200 ºC		
Cond. 12				300L/min	No heating, 100, 165ºC		

For test condition 9 (without forced cooling), Fig. 13 shows the temperatures raise of the cartridge heater ($T_h - T_{amb}$), the free end (FE) and drive end (DE) rotor surfaces, ($T_{11} - T_{amb}$ and $T_{12} - T_{amb}$), and the FE and DE bearing cartridges, ($T_1 - T_{amb}$ & $T_6 - T_{amb}$), versus elapsed test time. After a 20 minute interval, in similar fashion as in test conditions 7 and 8, the cartridge heater temperature (T_{hs}) is set at 100 ºC, 200 ºC, 300 ºC and 360ºC[9]. The rotor speed is 29.3 krpm.

Recall that the heater cartridge does not heat evenly the hollow rotor. There is an axial thermal gradient from the rotor free end towards its drive end. The measurements show that the rotor, although much cooler than the heater, has a temperature path which parallels that of the heater. The temperatures on the bearing cartridges, on the other hand, increase steadily with time.

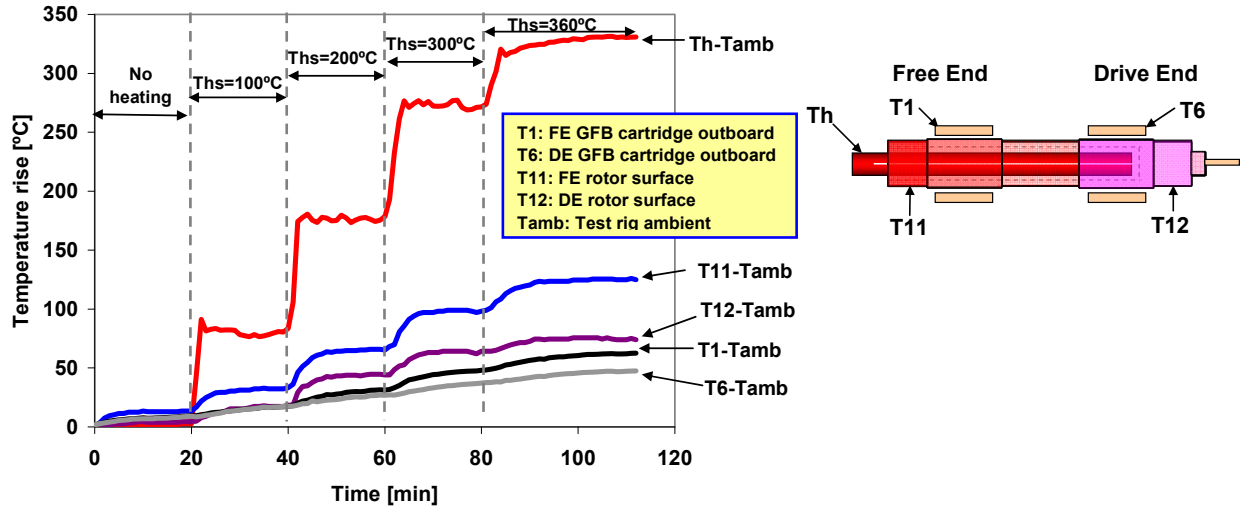

Fig. 13 Test condition 9: Recorded temperature raises of cartridge heater (T_h - T_{amb}), rotor free end (FE): (T_{11} - T_{amb}) and drive end (DE): (T_{12} - T_{amb}), and FE and DE bearing cartridges (T_1 - T_{amb} & T_6 - T_{amb}). Heater set temperature (T_{hs}) at 100 ºC, 200 ºC, 300 ºC, and 360ºC. Rotor speed = 29.3 krpm. No cooling flow into bearings. Baseline condition.

[9] Maximum operating temperature of the cartridge heater (rated at 400W with 120VAC) is 360ºC while the rotor operates at a speed of 30 krpm and without cooling flow into the test bearings.

For test conditions 9 through 12, i.e. with increasing strength of the cooling gas stream (0 – 150 L/min per bearing), Fig. 14 depicts the measured heater temperature (T_h) and the temperature raise on the FE and DE GFB cartridges, (T_1-T_{amb}) and (T_6-T_{amb}), versus elapsed test time. Note that the maximum operating temperature of the cartridge heater surface reduces from 360ºC (without cooling and with 50 L/min per bearing) to 190ºC and 165ºC for 100 L/min and 150 L/min cooling flows, respectively. Since the heater electrical power is limited, the reduction in its surface temperature is due to the cooling flow with increasing strength quickly advecting heat from the whole test rig. The measurements show that without a forced cooling flow the temperature raise in the bearing cartridges is highest. The effectiveness of the cooling method is clearly demonstrated for flows above 100 L/min. Note that at highest heater temperature, the effect of cooling flow is most distinctive.

At T_{hs}=360ºC, the recorded maximum cooling capability of the forced axial flow on the FE bearing cartridge temperature is 0.44ºC/LPM (22ºC decrease due to 50 L/min at 30 krpm). Note that, for operation at ambient or a lower heater temperature condition, the cooling flow stream demonstrates very limited effectiveness, for example, 0.05 ºC/LPM (5 ºC decrease due to 100 L/min at 30 krpm) and 0.09 ºC/LPM (9 ºC decrease due to 100 L/min at 30 krpm) for no heating and T_{hs}=100ºC, respectively.

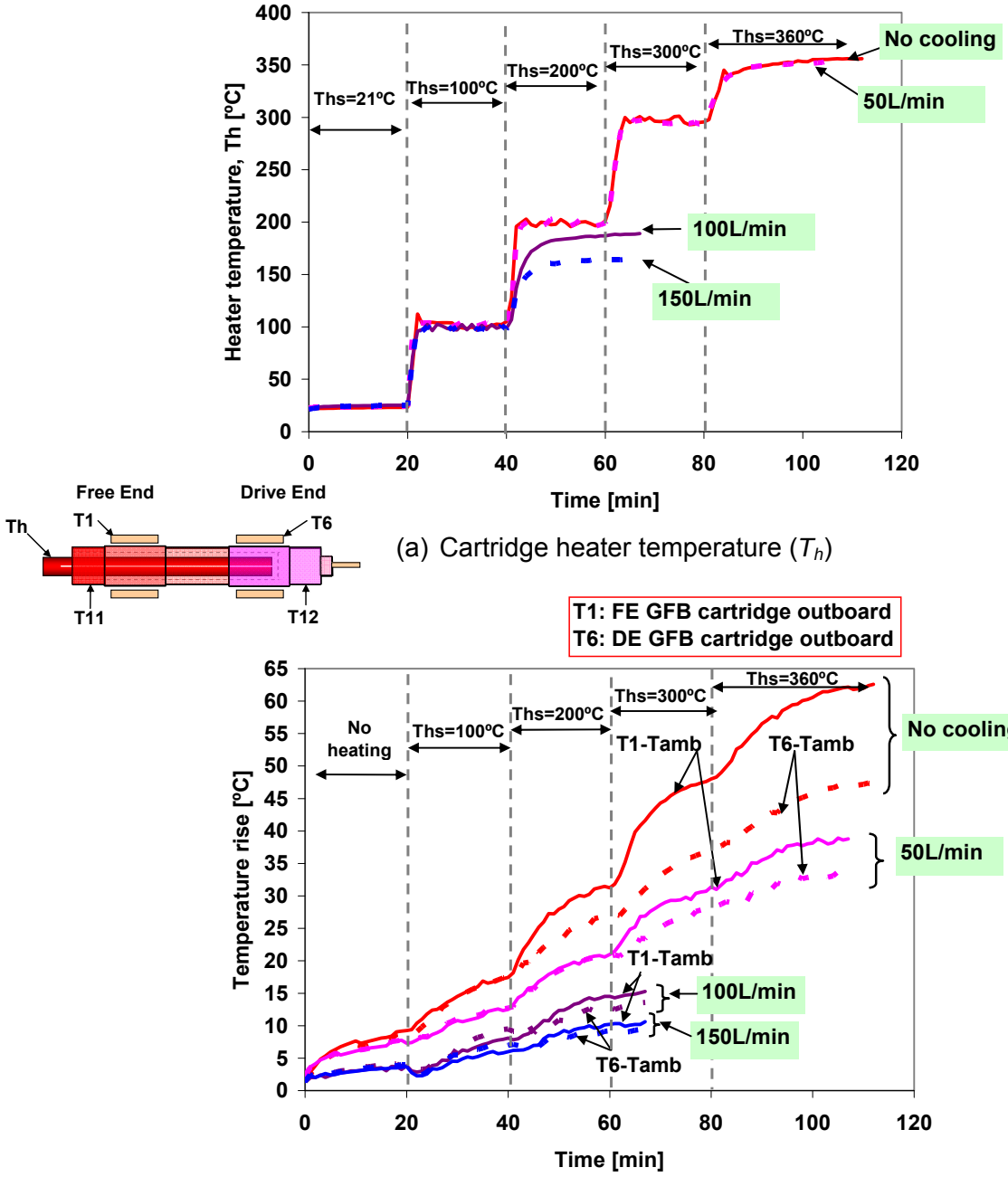

Fig. 14 Test conditions 9-12: (a) Cartridge heater temperature (T_h) and (b) temperature raises in FE and DE FB cartridges, (T_1-T_{amb}) and (T_6-T_{amb}), versus elapsed time for increasing strengths of cooling stream (max. 300L/min). Heater set temperature (T_{hs}) at 100 ºC, 200 ºC, 300 ºC and 360ºC. Rotor speed of 29.3 krpm.

For two set heater temperatures, 100 ºC and 200 ºC, Fig. 15 depicts the temperature raise on the FE and DE GFB cartridges, (T_1-T_{amb}) and (T_6-T_{amb}), quickly decreasing with the strength of the cooling flow rate. The measurements show that the lowest flow rate (50 LPM) produces the

largest thermal gradient, i.e. the largest difference in bearing operating temperatures. The largest cooling stream (150 LPM) hardly changes the bearing temperatures when compared to the results produced by a weaker one, i.e. 100 LPM. It is presumed that flow rates >100 LPM are already turbulent in character.

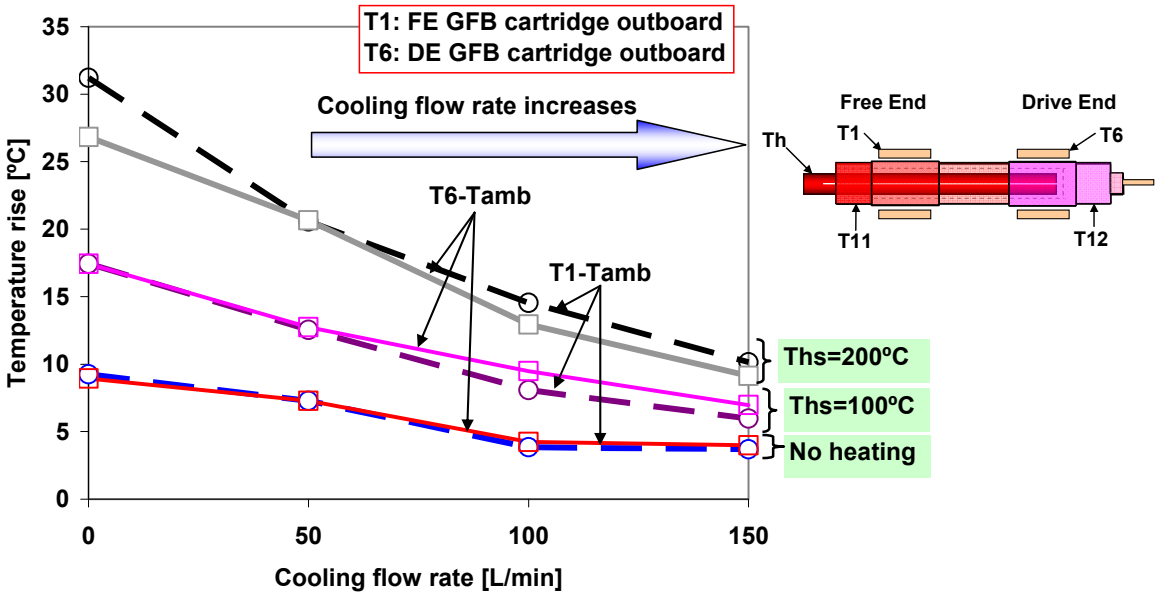

Fig. 15 Test conditions 9-12. Effect of cooling flow on bearing temperatures: Temperature raise in FE and DE FB cartridges, (T_1-T_{amb}) and (T_6-T_{amb}), versus strength of cooling flow stream. Operation at ambient condition and with cartridge heater set temperature (T_{hs}) at 100, 200ºC. Rotor speed of 29.3 krpm.

Figure 16 depicts the recorded rotor speed coastdown versus time without and with 50 LPM/bearing axial cooling (corresponding to test conditions 7 through 10). For operation at ambient temperature (no heating), no major differences in the coastdown speed curves are noticeable when supplying the forced cooling flow. On the other hand, at T_{hs}=360ºC, the overall coastdown time reduces by 20% (13 second) with a cooling flow of 50 LPM. At the highest rotor temperature, the forced cooling flow remarkably delays the touchdown speed and increases the overall coastdown time.

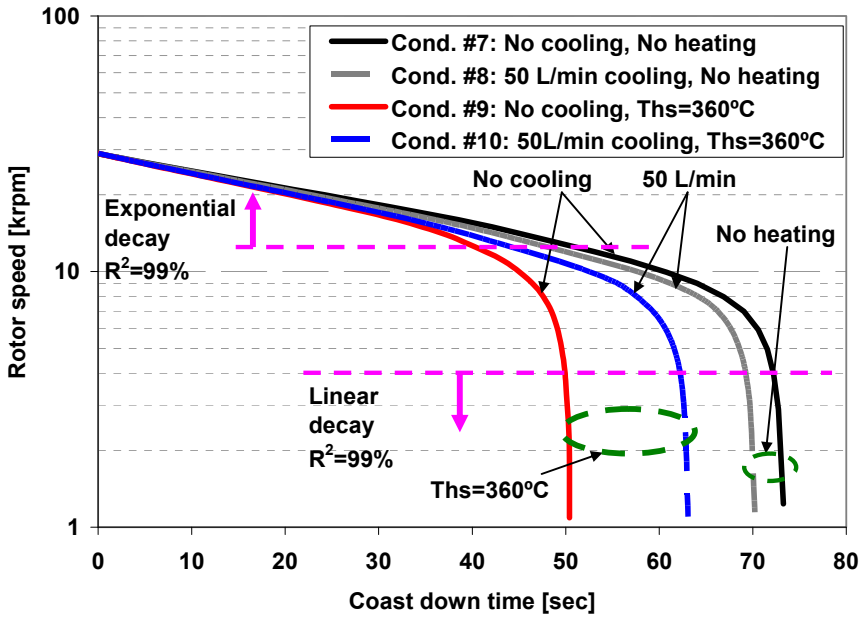

Fig. 16 Test condition 7-10. Effect of cooling flow on time extent for rotor speed coastdown response: Recorded rotor coast down speed versus time with increasing strength of cooling flow and heater temperature. Baseline imbalance.

Post-test condition of test rotor and GFBs

Figure 17 shows (negative) photographs of the test bearings and rotor before and after the tests listed in Table 3 (overall 50 hours of operation). Since the test bearings do not have any protective coatings on their top foil surfaces, wear on the top foil is a critical concern. The majority of the *polished* (wear) marks on the top foil are at its axial edges.

The rotor, originally coated with a 3 micrometer thin dense Chrome layer, shows wear marks at the locations in contact with the bearings, in particular the bearings' outboard edges.

The color of the rotor surface changes along its axes due to the considerable axial temperature gradient, see **Appendix F**. A higher temperature on the free end rotor OD renders a much darker color on its surface than at the drive end rotor OD.

Transient rubs and contact during start up and shutdown cycles, and predominant rotor conical motions, lead to the large areas of wear on the outboard rotor/bearing edges.

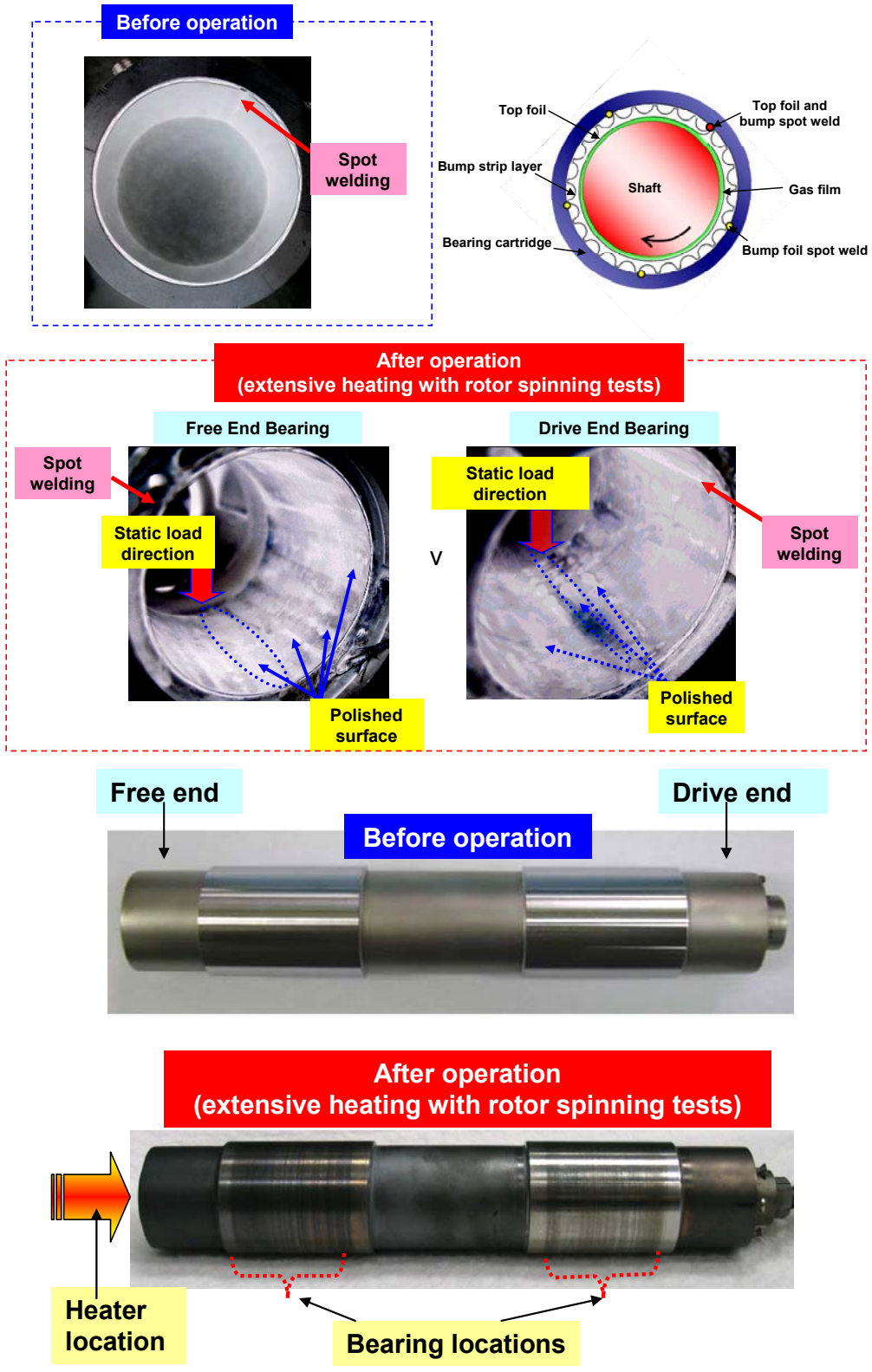

Fig. 17 Surface condition of test GFBs (negative photographs) and rotor after high temperature rotordynamic tests. Overall time of operation=50 hours.

CONCLUSIONS

Demonstrated gas foil bearing (GFB) operation at high temperature is fundamental to enable implementation of these bearings into gas turbine applications. Presently, experiments on a hollow test rotor (1.1 kg, 38.1 mm OD, and 25.4 mm ID) supported on two GFBs, 2nd generation, are performed to evaluate the rotordynamic performance of the hot rotor-GFB system while operating at increasing shaft temperatures. An inexpensive electric cartridge, fitting loosely inside the hollow rotor, heats unevenly the rotor.

A series of rotor speed coast downs from 30 krpm demonstrate the rotor response linearity with added imbalance masses. In the current measurements, there are no noticeable differences in rotor response for operation at ambient temperature and at the hottest shaft temperature. While coasting down from 30 krpm to ~11 krpm, the rotor speed decays exponentially, as is typical in systems with viscous drag. As the rotor and bearing temperatures increase, the air becomes more viscous and the bearing clearances decrease; hence the coastdown time somewhat decreases.

The temperatures on the bearing cartridges raise as the rotor temperature increases and also as the operating speed increases. At the hottest test condition, a forced cooling flow stream (at ~23ºC) significantly reduces the bearing temperatures. On the other hand, for operation at ambient or moderately low shaft temperature conditions, a cooling stream is of limited effectiveness. Thermal management with axial cooling streams is beneficial at high temperatures and with large flow rates ensuring turbulent flow conditions.

In gas turbines, an effective thermal management strategy must be ascertained to keep temperatures low, not affecting significantly the material properties of the components, and avoiding excessive thermal gradients, radial and axial. Cold gas bled-off from the compressor is readily available to cool the support bearings and hot rotor. Note that too large cooling rates will reduce engine power output and efficiency, however[10]. Determination of the minimum cooling flow rate for adequate thermal management is an important issue of scrutiny.

The current measurements demonstrate the stability and dynamic forced performance of the rotor-GFB system operating with a hot rotor. The acquired test results will serve to benchmark computational predictive tools near completion [14].

[10] Note that the temperature of air at a compressor discharge is relatively high, ~ 150ºC for the low-pressure stage and 343ºC for the high-pressure stage [4].

PROPOSED WORK IN NEXT QUARTER

Presently, after completion of the extensive tests detailed above, a 210 V circuit source (rather than 120 V) will power the cartridge heater to convert more electrical power into heat, and hence increase (significantly) the rotor and bearing temperatures. Rotor outer surface temperatures as high as 400ºC are expected.

In 2008, two 2nd generation FBs coated with a patented solid lubricant (Korolon800®, max. 400ºC) were acquired from Mohawk Innovative Technology, Inc. (MiTi®). In addition, one uncoated hollow rotor was manufactured for planned rotordynamic performance tests with the MiTi® GFBs. Therefore, the MiTi® FBs will replace the Foster-Miller FBs. In addition, high temperature fiberoptic displacement sensors[11] (max. 482ºC) will replace the eddy current displacement sensors to enable accurate measurements at high shaft temperatures.

Note that the MiTi® FBs have an outer diameter (44.64 mm) that is smaller than the inner diameter of the bearing holes in the rig housing. Each Miti® GFB fits into an outer shall for insertion into the (original) rig housing, see Fig 18. Each FB outer shell is fitted with four thermocouples on its outer surface.

The rod connecting the drive motor to the test rotor will be shortened to raise the elastic mode critical speed of the rotor-bearing system, thus ensuring safe operation at motor speeds as high as 50 krpm. The experimental results will further aid to anchor the developed predictive tools.

[11] Presently, calibrations of the fiberoptic sensors to a new test rotor are completed.

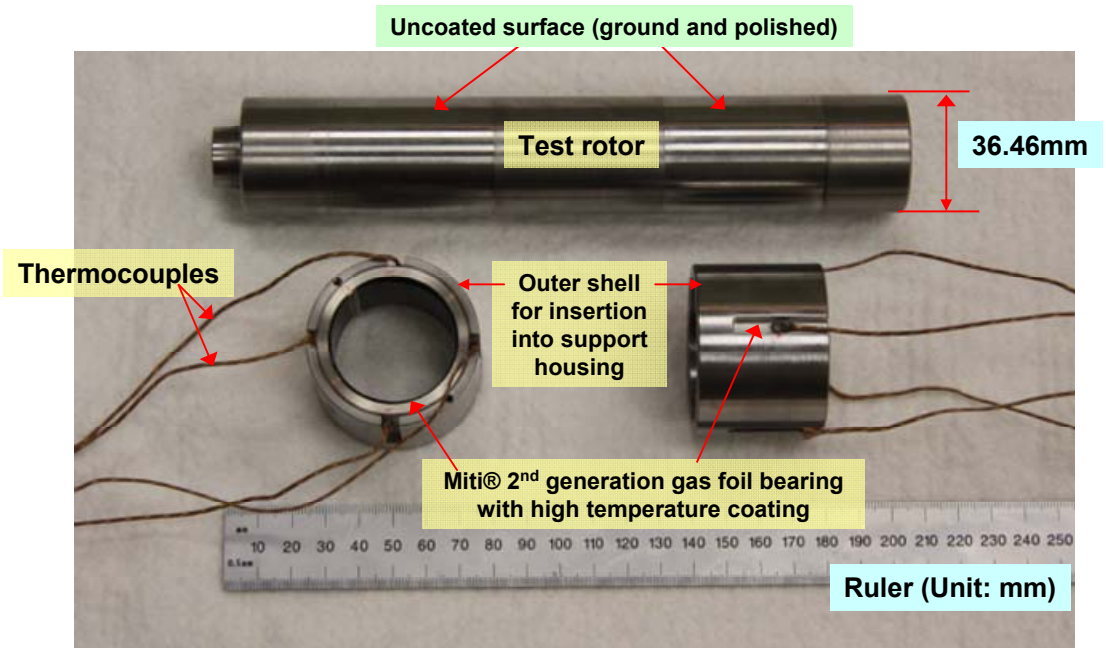

Fig. 18 (new) Test rotor and Miti® GFBs. GFBs in outer shell for installation in test rig housing.

KIST (Korea Institute of Science and Technology) donated one high-speed (high temperature solid lubricant coated, max. 400ºC) Inconel rotor and two pairs of GFB cartridges with 20 bump strips (five different bump heights × four per each height). See **Appendix M** for details. A series of static load-deflection tests and shaker load tests are being conducted on the KIST foil bearings to determine their structural characteristics. After evaluating the bearing force coefficients, rotordynamic tests will follow.

NOMENCLATURE

D_I	Bearing cartridge inner diameter [m]
D_O	Bearing cartridge outer diameter [m]
D_T	Top foil inner diameter [m]
h_B	Bump height [m]
L	Bearing axial length [m]
M_{DE} and M_{FE}	Fractions of the test rotor weight acting on each bearing [g]
m_i	Calibrated imbalance mass [g]
l_B	Bump length [m]
N_B	Number of Bumps [-]
r	Radial location of imbalance mass [m]
r_B	Bump arc radius [m]
s_0	Bump pitch [degree]
t_B	Bump foil thickness [m]
t_{BC}	Bearing cartridge wall thickness [m]
t_T	Top foil thickness [m]
T_6~T_9	Drive end GFB cartridge outboard temperature [ºC]
T_{10}	Drive end bearing support housing surface temperature [ºC]
T_{11}	Free end rotor surface temperature [ºC]
T_{12}	Drive end rotor surface temperature [ºC]
T_{13}	Connecting rod temperature [ºC]
T_{14}	Drive motor inboard temperature [ºC]
T_{15}	Drive motor outboard temperature [ºC]
T_{16}	Drive motor support housing temperature [ºC]
T_{amb}	Test rig ambient temperature [ºC]
T_h	Cartridge heater temperature [ºC]
T_{hs}	Cartridge heater set temperature [ºC]
u	Mass imbalance displacement [m]
α	Bump arc angle [degree]

REFERENCES

[1] DellaCorte, C., and Valco, M., 2003, "Oil-Free Turbomachinery Technology for Regional Jet, Rotorcraft and Supersonic Business Jet Propulsion Engines," AIAA Paper No. ASABE–2003–1182.

[2] Agrawal, G. L., 1997, "Foil Air/Gas Bearing Technology: An Overview," ASME Paper No. 97-GT-347.

[3] O'Connor, Leo, 1993, "Fluid-film foil bearings control engine heat," Mech. Eng, **115**, pp. 72-75.

[4] Radil, K., DellaCorte, C., Zeszotek, M., 2007, "Thermal Management Techniques for Oil-Free Turbomachinery Systems," STLE Tribol. Trans., **50**. pp. 319-327.

[5] Dykas, B. D., 2006, "Factors Influencing the Performance of Foil Gas Thrust Bearings for Oil-Free Turbomachinery Applications," Ph.D. Diss., Case Western Reserve University, Cleveland, OH.

[6] Bauman, S., 2005, "An Oil-Free Thrust Foil Bearing Facility Design Calibration, and Operation," NASA/TM-2005-213568.

[7] Heshmat, H., Hryniewicz, P., Walton, J. F., Willis, J. P., Jahanmir, S., DellaCorte, C., 2005, "Low-Friction Wear-Resistant Coatings for High-Temperature Foil Bearings," Tribol. Int., **38**, pp. 1059-1075.

[8] Rubio, D., and L., San Andrés, 2006, "Bump-Type Foil Bearing Structural Stiffness: Experiments and Predictions", ASME J. Eng. Gas Turbines Power, **128**, pp. 653-660.

[9] Rubio, D., and San Andrés, L., 2007, "Structural Stiffness, Dry Friction Coefficient, and Equivalent Viscous Damping in a Bump-Type Foil Gas Bearing," ASME J. Eng. Gas Turbines Power, **129**, pp. 494-502.

[10] San Andrés, L., Rubio, D., and Kim, T.H, 2007, "Rotordynamic Performance of a Rotor Supported on Bump Type Foil Gas Bearings: Experiments and Predictions," ASME J. Eng. Gas Turbines Power, **29**(3), pp. 850-857

[11] Breedlove, A., 2007, "Experimental Identification of Structural Force Coefficients in a Bump-Type Foil Bearing," Texas A&M University, M.S. Thesis, College Station, TX.

[12] Kim, T. H., 2007, "Analysis of Side End Pressurized Bump Type Gas Foil Bearings: A Model Anchored to Test Data," Texas A&M University, Ph. D. Diss., College Station, TX.

[13] Kim, T. H., and San Andrés, L., 2008, "Rotordynamic Measurements on a High Temperature Rotor Supported on Gas Foil Bearings," Technical Report No. TRC-B&C-3-08, Texas A&M Univ. College Station, TX.

[14] San Andrés, L., and Kim, T. H., 2008, "Thermohydrodynamic Analysis of Bump Type Gas Foil Bearings: Model and Predictions," Technical Report No. TRC-B&C-2-08, Texas A&M Univ. College Station, TX.

[15] San Andrés, L., Kim, T. H., 2009, "Thermohydrodynamic Model Predictions and Performance Measurements of Bump-type Foil Bearing for Oil-Free Turboshaft Engines in Rotorcraft Propulsion Systems," American Helicopter Society 65th Annual Forum, Grapevine, Texas, May 27- 29, 2009.

[16] San Andrés, L., and Kim, T. H., 2009, Thermohydrodynamic Analysis of Bump Type Gas Foil Bearings: A Model Anchored to Test Data," ASME Paper No. GT2009-59919 (accepted for publication at ASME J. Eng. Gas Turbines Power).

[17] San Andrés, L., and Kim, T. H., 2009, "Forced Nonlinear Response of Gas Foil Bearing Supported Rotors," Tribol. Int., **41**, pp. 704-715.

[18] http://www.matweb.com. Accessed May 14, 2009.

[19] Maalouf, M. G., 2007, "Slow Speed Vibration Signal Analysis: If You Can't Do It Slow, You Can't Do It Fast," ASME Paper No. GT2007-28252.

[20] Bently, D.E., 2002, *Fundamentals of Rotating Machinery Diagnostics*, Bently Pressurized Bearing Company, Minden, NV.

[21] Bachschmid, N., Pennacchi, P., and Vania, A., 2004, "Diagnostic Significance of Orbit Shape Analysis and its Application to Improve Machine Fault Detection," J. Braz. Soc. Mech. Sci. Eng. **26**, pp. 200–208.

SECTION 2.

MODEL OF GFBS WITH HOT ROTOR AND PREDICTIONS COMPARED TO TEMPERATURE AND ROTORDYNAMIC MEASUREMENTS

Edited by Luis San Andrés, original by Dr. Tae Ho Kim

The widespread usage of foil bearings in micro gas turbines relies on efficient and accurate physics based computational models with predictions anchored to reliable test data. Presently, a model for the thermal energy transport in a hot rotor–GFB test system and with cooling flow paths [1,2] predicts the bearings' temperature and pressure fields, the bearing static load performance parameters and dynamic force coefficients. A finite element (FE) model of the test rotor-GFBs using linearized bearing force coefficients predicts the system critical speeds, damping ratios and rotor synchronous responses. All model predictions are obtained for the foil bearings with nominal dimensions given in Table 1 and compared to measured temperature and rotor responses obtained in the TAMU rotor-foil bearing test rig, detailed in Section 1. Note that details in the foil bearings, including materials and geometry, are released. The bearing manufacturer, Foster-Miller, places no restrictions on the release of its foil bearing products.

COMPUTATIONAL MODEL OF GFB WITH HOT ROTOR

Prior research progress quarterly reports [1,2] describe the predictive model of GFBs with an inner cooling stream flowing through a hollow shaft and an outer cooling stream flowing through the thin film region and underneath top foil, as shown in Fig. 1. The model regards the inner and outer cooling gas streams as sinks of thermal energy. In addition, the cooling mass flow rates are large enough to keep their temperature uniform at (T_{C_i} , T_{C_o}) while advecting (removing) heat from the shaft and top foil back surface at temperatures (T_{S_i} , T_{F_o}). Figure 2 from Ref. [1] depicts the various heat flow paths in a foil bearing along with the nomenclature for the various temperatures in the components. The lumped parameter thermal model uses equivalent heat transfer coefficients representing multilayer heat conduction/convection for radial heat flow paths, as given in Fig. 2, from the film towards the bearing outer surface and/or the outer cooling stream, and/or from the film into an inner cooling stream. In operation, predicted shaft and bearing thermal expansion and centrifugal growth due to rotor spinning determine the actual operating bearing clearance. In the model, a thermal mixing parameter (λ) models the exchange

of flow and energy at the gap between the trailing edge and leading edge of the top foil. Ref. [1] details the inlet mixing mass flow conservation and energy balance equations. See **Appendices A-C**, reproduced from prior quarterly reports [1-3], for details of the GFB thermal model development and predictions compared to published test data.

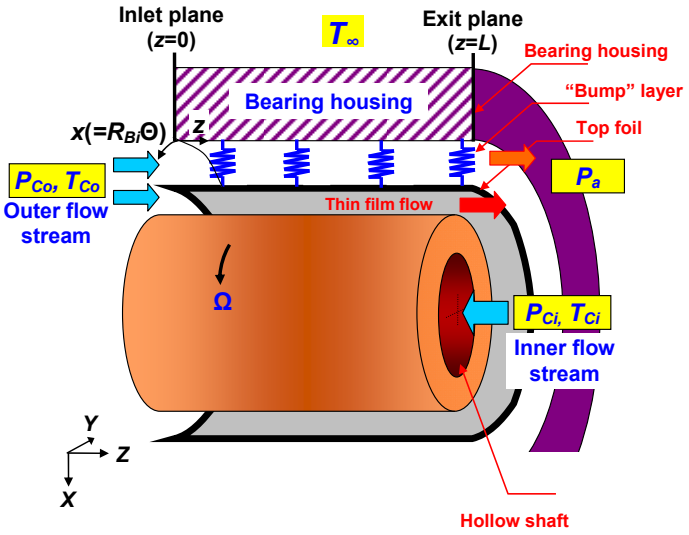

Fig. 1 Schematic side view of foil bearing with inner cooling stream (T_{Ci}, P_{Ci}) flowing through hollow shaft and outer cooling stream (T_{Co}, P_{Co}) flowing through thin film region and underneath top foil. Outer cooling flow exits to ambient pressure (P_a). Reproduced from Ref. [1]

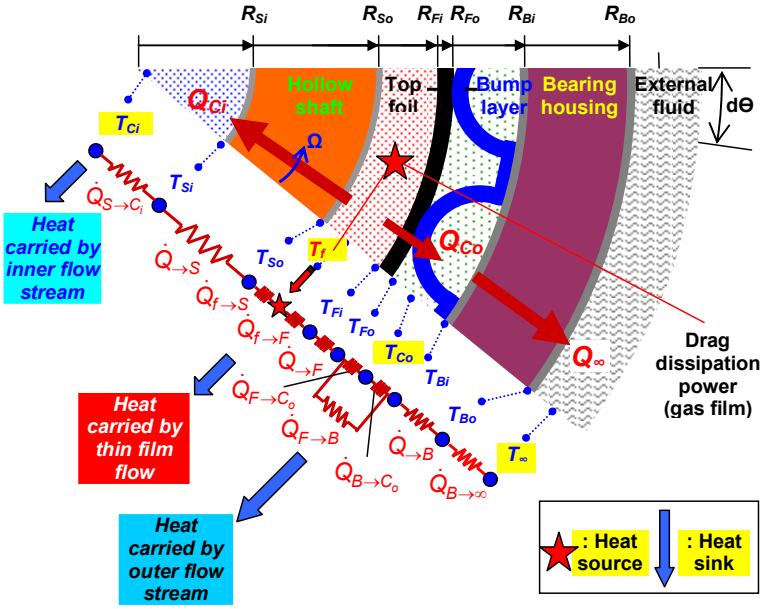

Fig. 2 Nomenclature for temperatures in foil bearing with cooling gas streams and schematic representation of heat flows. Reproduced from Ref. [1]

TEMPERATURE PREDICTIONS COMPARED TO TEST DATA

This section compares the measured temperature rises in the TAMU rotor-foil bearing test rig to predictions from the THD GFB computational model. The model accounts for the net thermal expansion of the shaft and bearing cartridge (S_T=S_{TS} - S_{TB}) and the shaft centrifugal growth (S_C) that reduce the FB nominal radial clearance (c) [1]. Presently, thermal expansion of the whole test rig casing or housing is not considered. In the THD model, an empirically based thermal mixing coefficient λ=0.65 represents best the gas flow and thermal energy balance at the conjunction of the top foil leading and trailing edges [1].

Operation without heating (room temperature)

Figure 3 shows the measured temperature rise (T_{DE}-T_{amb}) at the outboard of the drive end FB cartridge versus rotor speed for operation without a cooling stream and with a cooling stream ~ 50 L/min, half of the total supply cooling stream ~ 100 L/min (test conditions 1 and 2). Ambient temperature is ~ 21 °C and the cartridge heater is switched off. A fraction of the rotor weight ~ 6.5 N acts on the drive end bearing. The figure contains a graph showing the foil bearing and noting the orientation of the top foil spot-weld with respect to the vertical (gravity) plane. The data shown represents the (arithmetic mean) from the four temperature measurements around the bearing circumference; maximum and minimum values are also depicted. The FB cartridge temperature increases as the rotor speed increases, and decreases with the forced cooling stream ~ 50 L/min. Presently, predicted GFB cartridge (or housing) inner surface temperatures[1] are compared to the recorded temperatures. In general, predictions agree well with the test data. Discrepancies at low rotor speeds (0 – 15 krpm) are due to differences between the FB cartridges temperatures and ambient air temperature recorded before rotor spinning.

Figure 4 illustrates the predicted radial temperature profile in the foil bearing and rotor system without a cooling stream and with a cooling stream ~ 50 L/min. Rotor operation is at 30 krpm. Both peak film and axially averaged (mean) temperatures are presented in the figure. A cooling stream ~ 50 L/min not only decreases the gas film temperature (T_f), but also cools the shaft (T_{Si}, T_{So}) and the bearing cartridge (T_{Bi}, T_{Bo}).

[1] Axially averaged (mean) temperatures at the inner surface of the bearing cartridge.

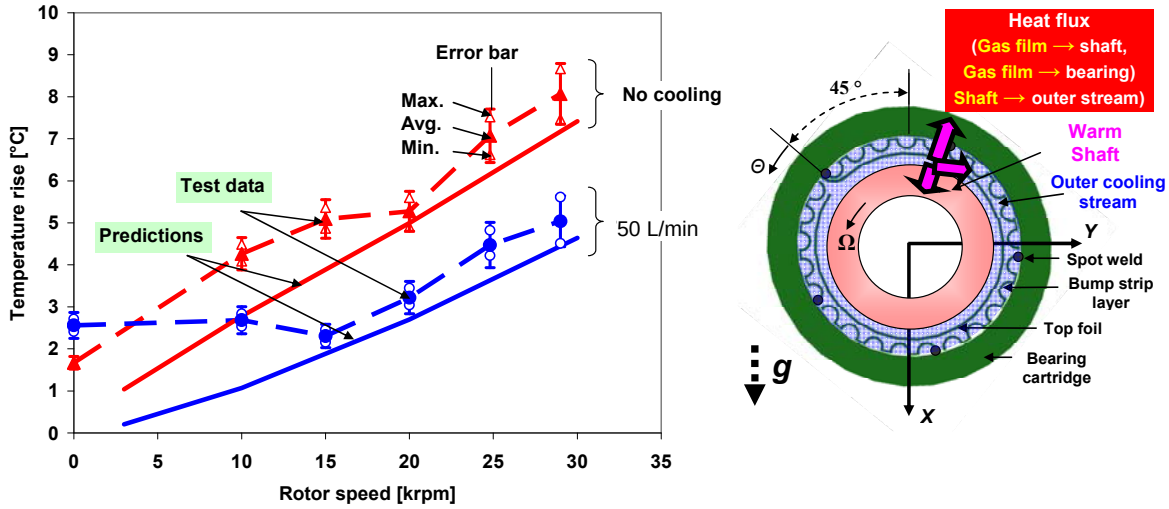

Fig. 3 Measured temperatures rise (T_{DE}-T_a) at the outboard of drive end FB cartridge versus rotor speed. Operation without cooling stream and with a cooling stream ~ 50 L/min. Ambient room air temperature T_a ~21 °C with cartridge heater switched off. Static load ~ 6.5 N. Predictions at FB cartridge inner surface. Cooling stream temperature T_{Co}~21 °C. Thermal mixing coefficient λ=0.65

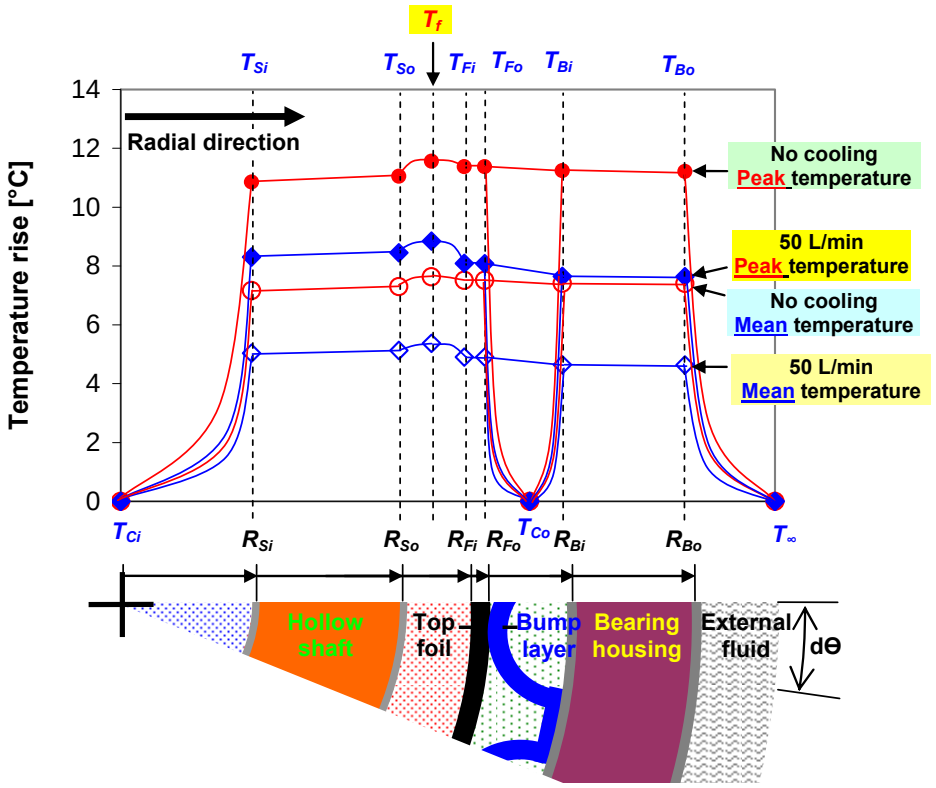

Fig. 4 Predicted radial temperature (rise) profile in foil bearing and rotor. Peak and axially averaged (mean) temperatures. Operation without cooling flow and with a cooling stream ~ 50 L/min. Ambient room air and cooling stream temperatures T_a~T_{Co}~21 °C. Thermal mixing coefficient λ=0.65. Static load ~ 6.5 N, rotor speed=30 krpm.

At a rotor speed of 30 krpm and without a forced cooling stream, Fig. 5 depicts the predicted dimensionless film pressure and temperature rise fields. Recall that the test GFBs are 2nd generation with five welded bump strips every 72 deg around the circumferential direction. The weld locations have a larger stiffness than at the bumps; hence the pressure field shows (slight) kinks at the strip welds' locations. Along the circumferential coordinate, 45 °< Θ < 200 °, the film temperature increases as the gas flows from the top foil leading edge (Θ = 45 °) and removes the shear induced mechanical energy. However, for Θ > 200 ° the temperature drops due to the reduction in hydrodynamic pressure and the gas expansion that cools the gas film.

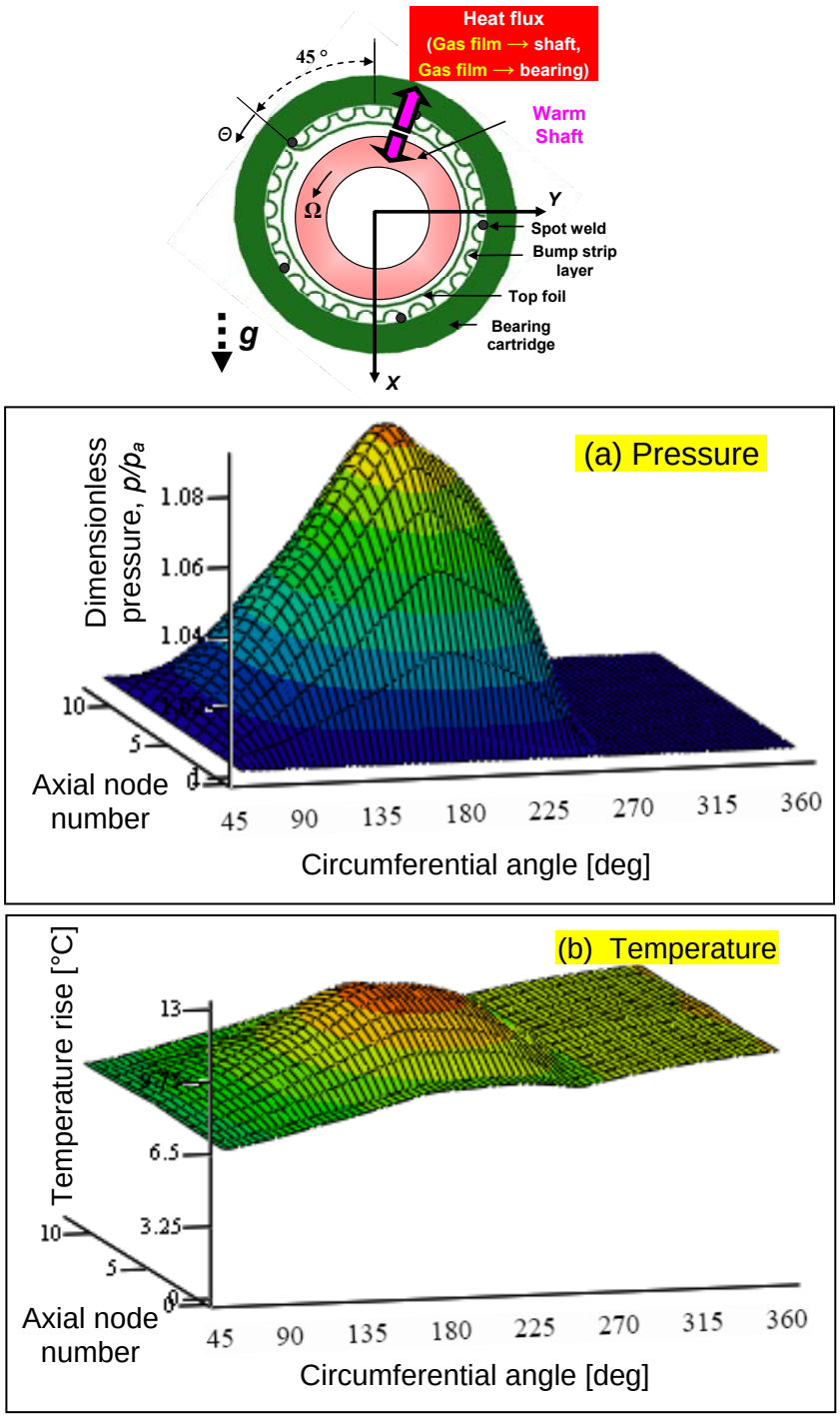

Fig. 5 Predicted thin film (a) pressure and (b) temperature fields in drive end GFB operating at 30 krpm. No forced cooling stream. Ambient temperature T_a~21 °C. Thermal maxing coefficient λ=0.65. Static load ~ 6.5 N. Journal eccentricity= 7 μm and attitude angle= 59 deg. Minimum film thickness= 27 μm

Operation with heated rotor

The electric heater cartridge (max. 360 °C) heats (unevenly) the hollow rotor. Figure 6 shows the measured FBs' temperature rise versus shaft temperature rise for operation at 30 krpm. No cooling flow is provided (test condition 9). See Fig. 1 in section 1 for details on the test rig configuration. The FB temperatures are recorded at the cartridges outboard location, *T*6 and *T*1 for the drive end and free end bearings, respectively, see also Fig. 3 in section 1. As the shaft temperature increases, the bearing cartridge temperature increases linearly. There is excellent agreement between predictions and test data for the drive end FB. However, for the free end FB the predictions are ~25% higher than the test data. The large difference is attributed to the (known) large temperature gradient along the heater axial length. That is, the measured shaft temperature at the rotor ends is not equal to the shaft temperatures (directly underneath) the bearing locations.

Figure 7 depicts the predicted film pressure and temperature rise fields for the drive end FB operating at 30 krpm and at a shaft temperature at 100 °C (= ambient 21°C + temperature rise 79°C, as seen in Fig. 6), The pressure profile becomes slightly sharper (at the strip weld locations) when compared to that derived for operation without shaft heating. As expected, the temperature field evolves steadily in the circumferential direction and is nearly uniform in the axial direction since it is influenced strongly by the specified (hot) shaft temperature. Note that the film temperature is lowest at the free end of the top foil (45 deg) where there is thermal energy mixing with cold fresh air drawn by natural suction. The predicted journal eccentricity is 4.5 μm and attitude angle is 67 deg, and the minimum film thickness is 28 μm. When comparing static performance parameters with respect to those for operation without shaft heating (see Fig. 5), the journal eccentricity decreases and the journal attitude angle increases, and the minimum film thickness increases.

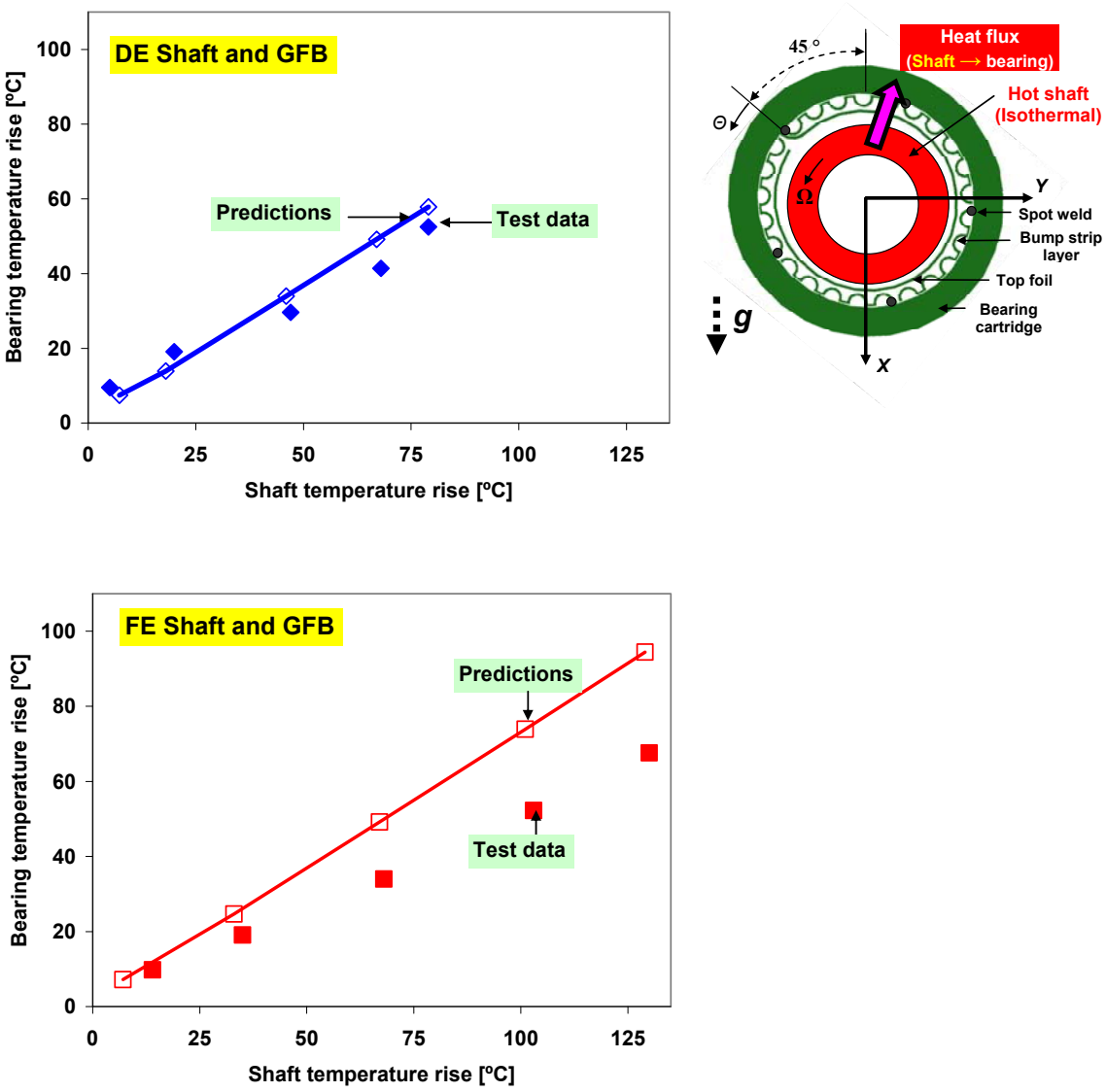

Fig. 6 Measured and predicted temperature rise at (a) drive end FB and (b) free end FB cartridges versus shaft temperature rise. Measurements at FBs outboard location *#T6* and *#T1* for drive end and free end FBs, respectively. Predictions at FB cartridge inner surface. Static load ~ 6.5 N and rotor speed= 30 krpm. No forced cooling flow. Ambient temperature T_{Co}~21 °C. Thermal mixing coefficient λ=0.65

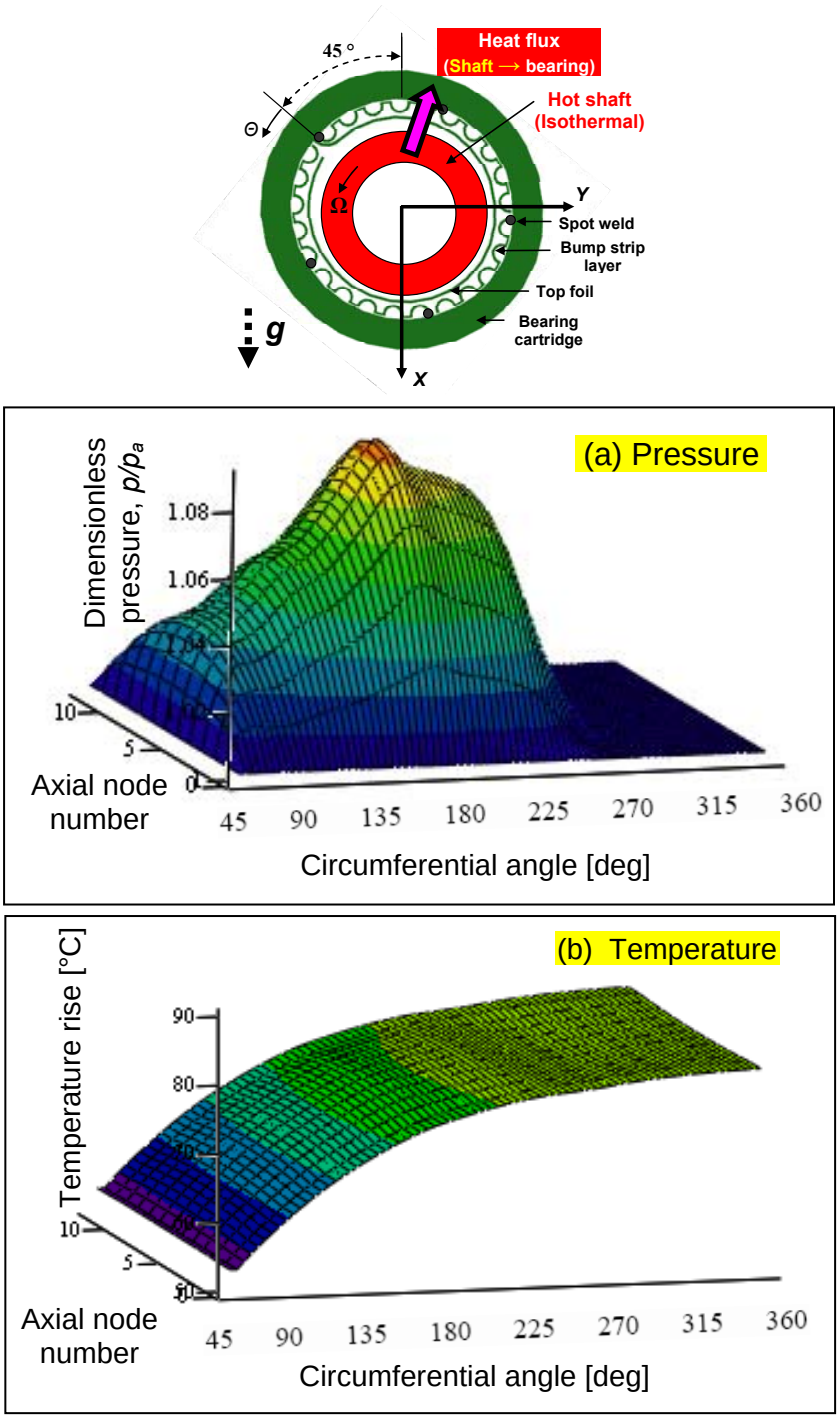

Fig. 7 Predicted thin film (a) pressure and (b) temperature fields in drive end GFB operating at 30 krpm. No forced cooling stream. Constant shaft temperature of 100°C. Thermal mixing coefficient λ=0.65. Static load ~ 6.5 N. Journal eccentricity: 4.5 μm. Journal attitude angle: 67 deg. Minimum film thickness: 28 μm

Figure 8 displays the measured temperature rise at the drive end GFB cartridge versus shaft temperature rise for increasing cooling flow rates to 150 L/min, half of the largest total supply cooling stream ~ 300 L/min (test conditions 1-2 and 9-12). The data was collected at the cartridge outboard location #*T*6. The predictions depict the temperature rise of the inner surface of the FB cartridge. As the cooling flow rate increases the FB cartridge temperature decreases significantly, in particular for the highest flow rates, > 100 L/min. In general, predictions agree well with test data.

Figure 9 shows the predicted radial temperature (rise) in the foil bearing and rotor system for increasing cooling stream flow rates to 150 L/min. Rotor operation is at 30 krpm. The axially averaged (mean) temperatures are presented in the figure. In the model, the shaft is uniformly hot (T_{Si}=T_{So}). The cooling stream flows within the gap between the rotating shaft and the bearing cartridge. This stream removes heat from the gas film as well as the top foil back surface. Note the large temperature difference between the hot shaft and the GFB inner surface for the strongest cooling stream (150 L/min).

For a rotor speed of 30 krpm, with shaft temperature at 64 °C (= heater rise of 32 °C + ambient at 32 °C, as in Fig. 9) and a cooling flow of 150 L/min, Fig. 10 shows the predicted film pressure and temperature rise fields. The pressure differential (p-p_{sub}), which directly affects the top foil deflection and film thickness, is obtained by subtracting the cooling stream pressure between the top foil and the bearing cartridge from the film pressure [1]. Note that a pressure differential along the bearing axial length forces the cooling stream underneath the top foil. The gas film temperature field is nearly uniform in the axial direction since it is influenced strongly by the constant shaft temperature and the cooling stream constant temperature.

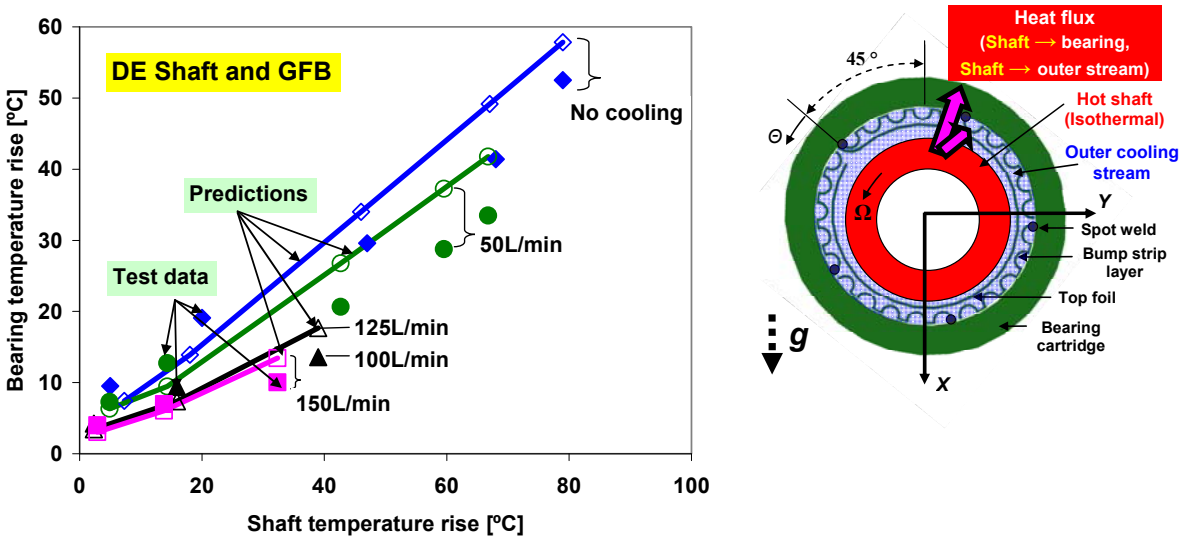

Fig. 8 Measured temperature rise at drive end FB cartridge versus shaft temperature rise for increasing cooling flow rates to 150L/min and T_{Co}~21 °C. Measurements at cartridge outboard location #*T6*. Predictions at GFB cartridge inner surface. Static load ~ 6.5 N, 30 krpm. Thermal mixing coefficient λ=0.65

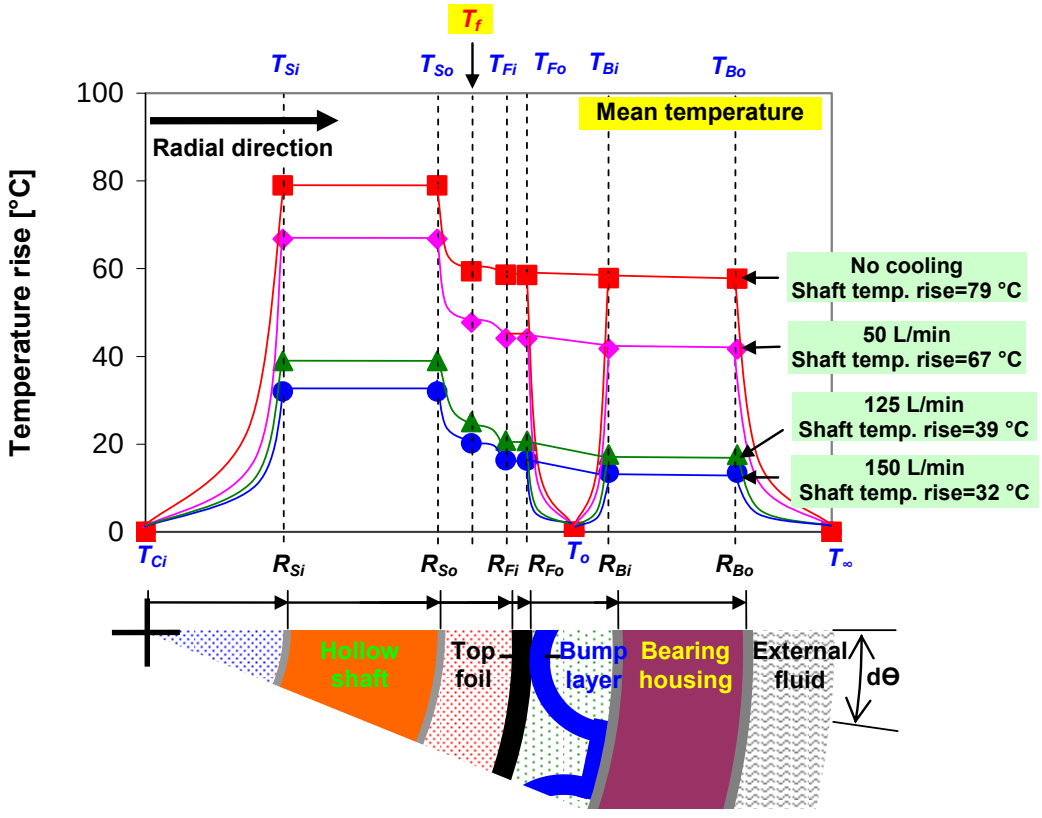

Fig. 9 Predicted radial temperature (rise) profile in foil bearing and rotor. Axially averaged (mean) temperatures. Operation with increasing cooling flow rates to 150 L/min and T_{Co}~21 °C. Thermal mixing coefficient λ=0.65. Static load ~ 6.5 N, rotor speed=30 krpm.

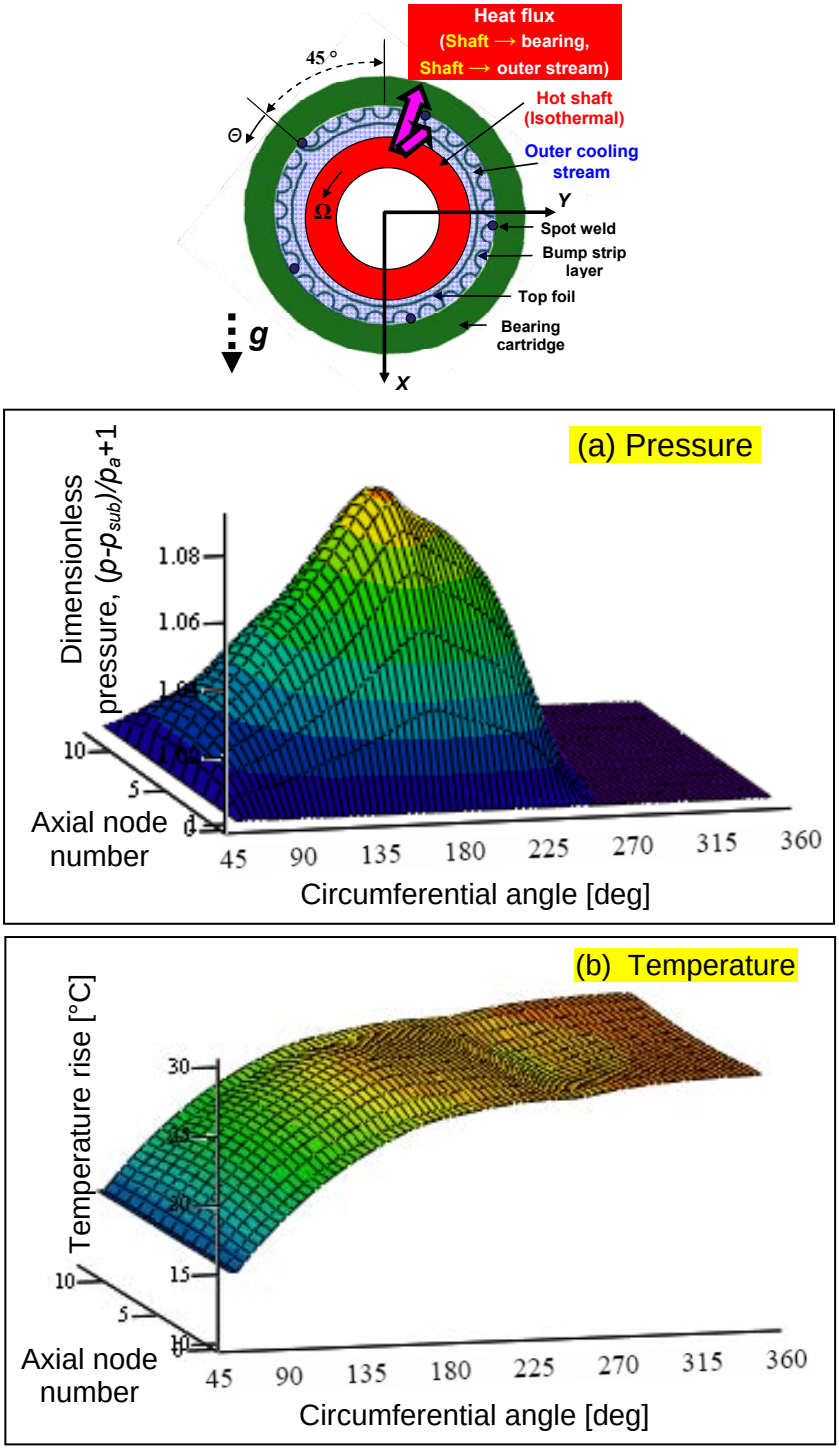

Fig. 10 Predicted thin film (a) pressure and (b) temperature fields in drive end GFB operating at 30 krpm. Cooling stream flow rate of 150 L/min and T_{Co}~21 °C. Shaft temperature of 64 °C. Thermal maxing coefficient λ=0.65. Static load ~ 6.5 N. Journal eccentricity= 5.5 μm and attitude angle= 62 deg. Minimum film thickness= 27 μm

GFB STATIC LOAD PARAMETERS, DYNAMIC FORCE COEFFICIENTS, AND ROTOR SYNCHRONOUS RESPONSE (PREDICTIONS AND MEASUREMENTS)

For the drive end GFB, which supports a static load of 6.5 N, and for operation at rotor speed of 30 krpm, Fig. 11 shows the predicted radial peak and mean (circumferential average) temperature profiles in the rotor-GFB system. The predictions show operation at ambient temperature (no heating) and with cartridge heater set temperatures (T_{hs}) at 200 °C and 360 °C. The inset table on the right of the figure lists the measured shaft temperature corresponding to the respective cartridge heat temperature. The predictions and measurements are for a condition without a forced outer cooling flow. That is, the heat flow path outwards to ambient includes conduction into the bearing cartridge and natural convection at the bearing OD. The mean temperatures are lower than the peak temperatures due to the thermal mixing with a fresh (cold) supply air flow at the leading edge of the top foil. As the heater temperature increases, the GFB temperatures increase accordingly.

Figures 12 through 14 present the predicted static load performance parameters for the drive end GFB versus rotor speed and for operating conditions identical to those in Fig. 12. As the rotor speed increases, the journal attitude angle, minimum film thickness, drag torque, peak film temperature rise, and shaft centrifugal growth increase. The journal eccentricity decreases with rotor speed. As the heater temperature increases, the journal attitude angle, drag torque, peak film temperature, and shaft thermal growth increase. The journal eccentricity decreases with shaft temperature. The heater temperature increases the minimum film thickness due to the increase in gas viscosity at low rotor speeds. However, at high rotor speeds, the minimum film thickness decreases since the bearing operating clearance reduces. Note that the decrease in the bearing operating clearance reduces the bearing load capacity and increases the likelihood of thermal seizure and bearing failure.

Figure 15 displays predicted GFB synchronous speed stiffness coefficients, (a) direct and (b) cross-coupled, versus rotor speed for increasing heater temperatures. An increase in the heater temperature increases significantly the direct stiffness coefficients (K_{XX}, K_{YY}), while the difference in the cross-coupled stiffness coefficients (K_{XY}-K_{YX}) increases slightly at low rotor speeds and decreases at high rotor speeds. In Fig. 16, the predicted direct damping coefficients (C_{XX}, C_{YY}) increase significantly with increasing heater temperature, in particular at low rotor speeds. The cross-coupled damping coefficients (C_{XY}, C_{YX}) change little at rotor speeds above 30

krpm. **Appendix J** provides the predicted stiffness and damping coefficients for the free end GFB.

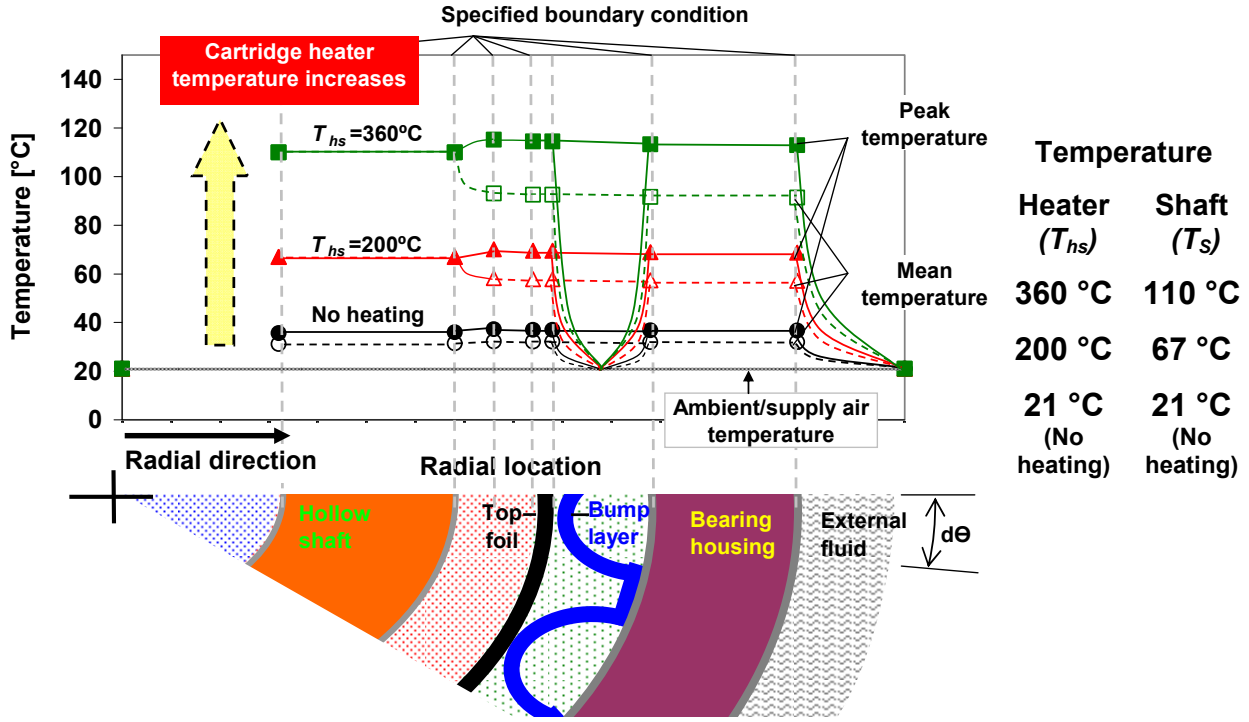

Fig. 11 Predicted radial temperature profile in drive end foil bearing and shaft for operation at ambient condition (no heating) and with cartridge heater set temperature (T_{hs}) at 200 °C and 360 °C. Static load 6.5 N. Rotor speed=30 krpm. No forced cooling flow.

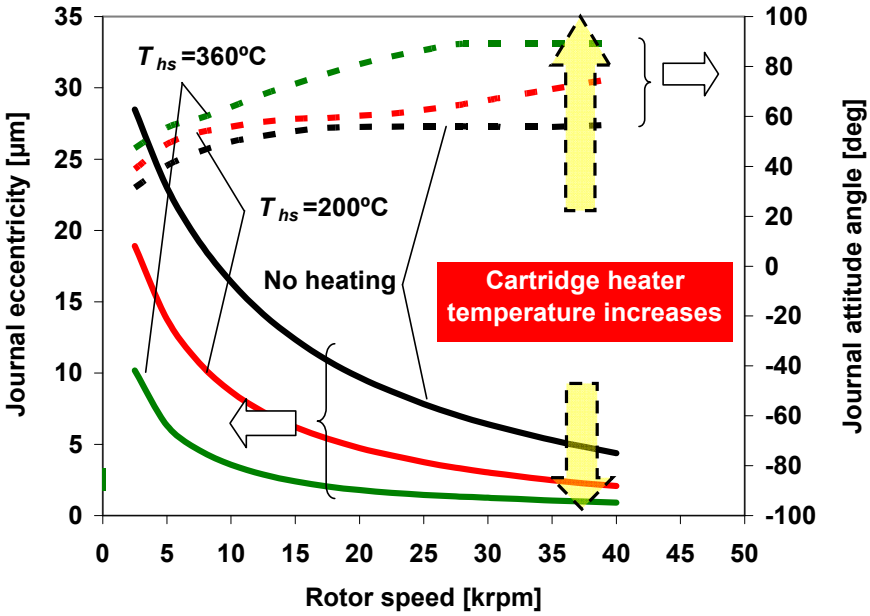

Fig. 12 Journal eccentricity and attitude angle for drive end GFB versus rotor speed for operation at ambient condition (no heating) and with cartridge heater set temperature (T_{hs}) at 200 °C and 360 °C. Static load 6.5 N. No forced cooling flow.

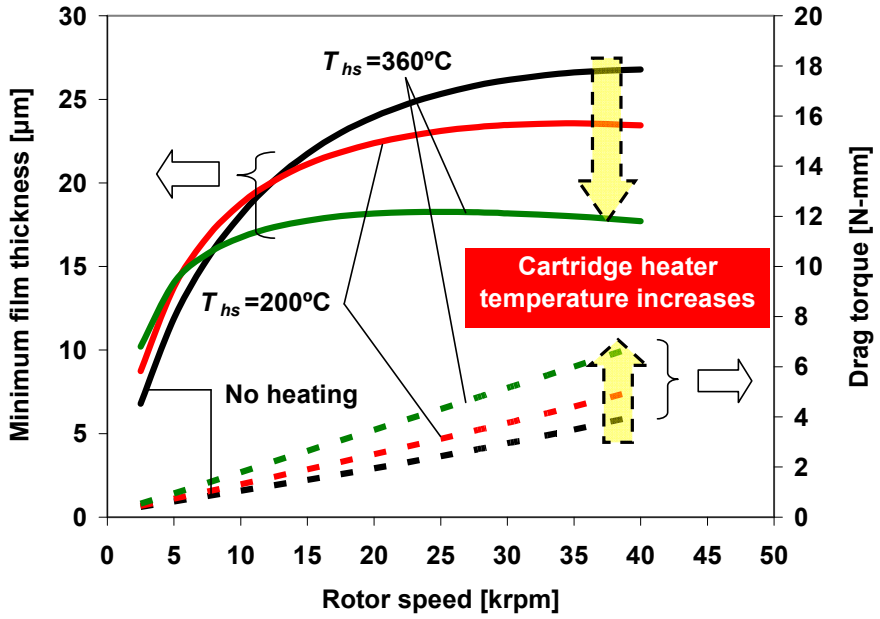

Fig. 13 Minimum film thickness and drag torque for drive end GFB versus rotor speed for operation at ambient condition (no heating) and with cartridge heater set temperature (T_{hs}) at 200 °C and 360 °C. Static load 6.5 N. No forced cooling flow.

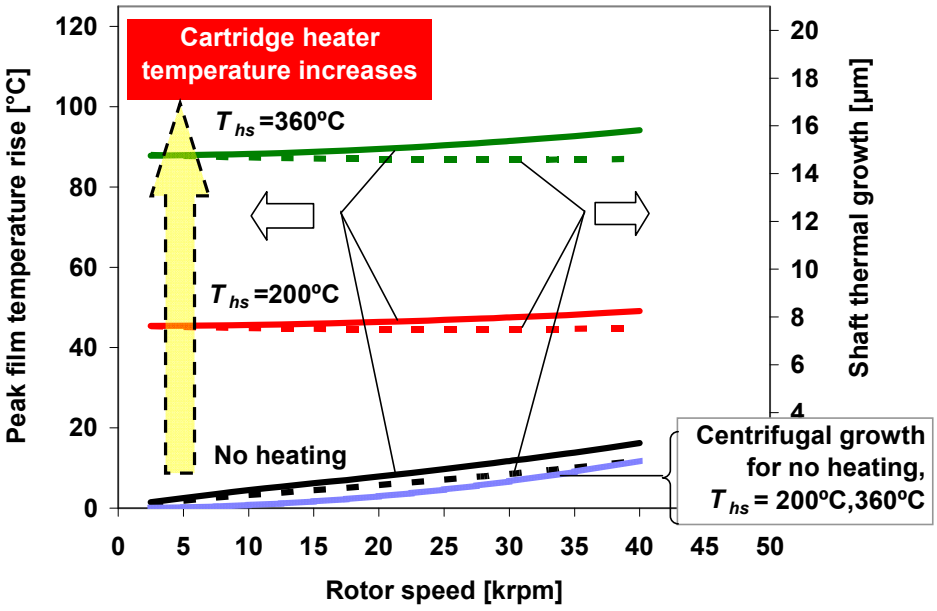

Fig. 14 Peak film temperature rise and shaft thermal growth for drive end GFB versus rotor speed for operation at ambient condition (no heating) and with cartridge heater set temperature (T_{hs}) at 200 °C and 360 °C. Shaft centrifugal growth denoted. Static load 6.5 N. No forced cooling flow.

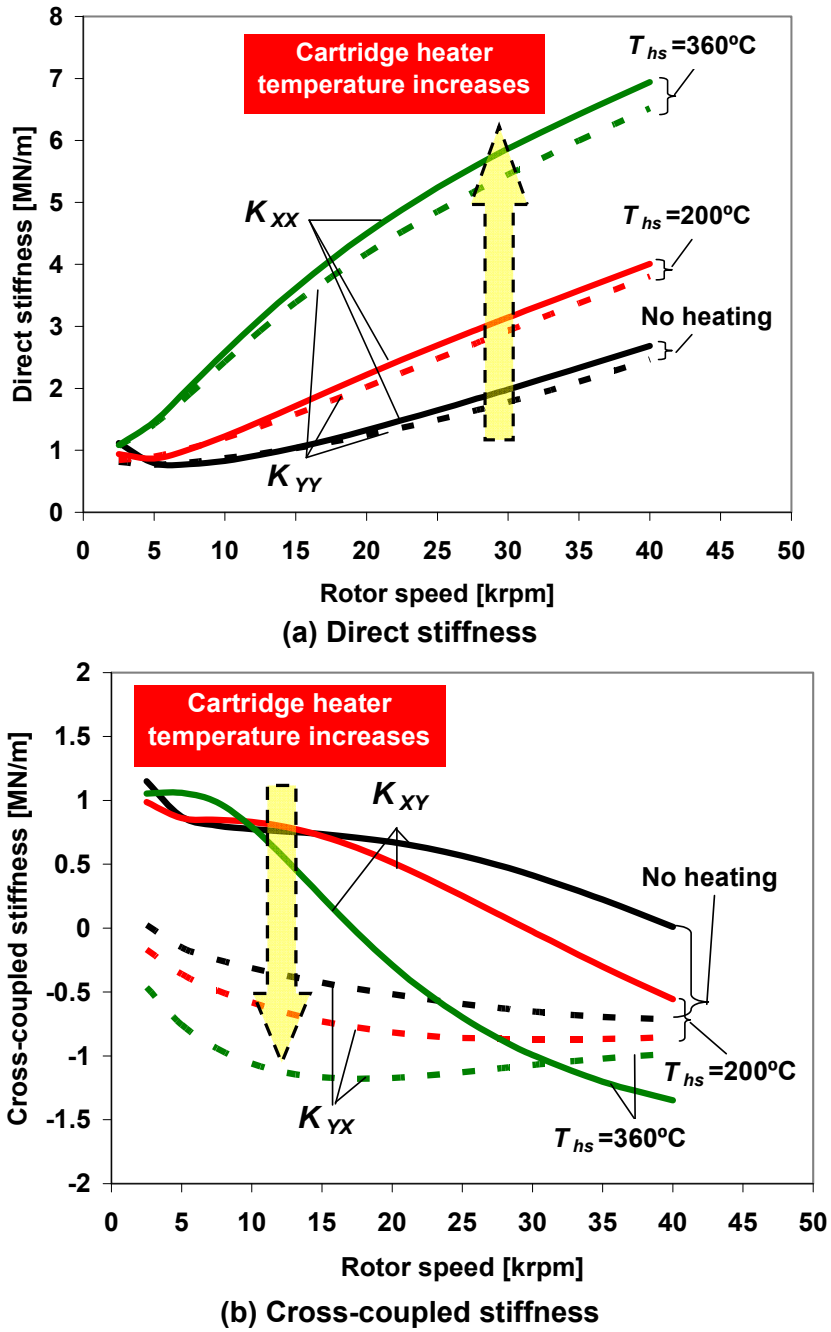

Fig. 15 (a) Direct stiffness and (b) cross-coupled stiffness for drive end GFB versus rotor speed for operation at ambient condition (no heating) and with cartridge heater set temperature (T_{hs}) at 200 °C and 360 °C. Static load 6.5 N. No forced cooling flow.

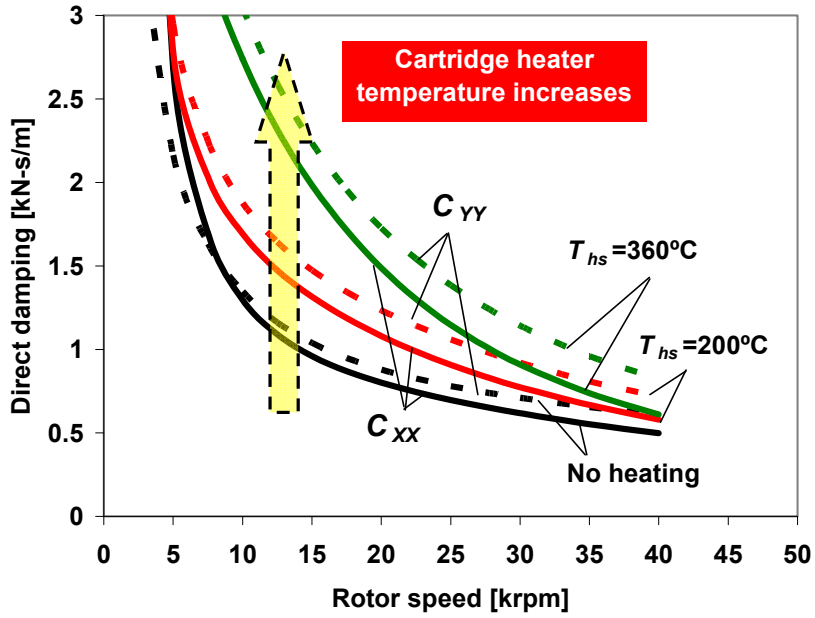

(a) Direct damping

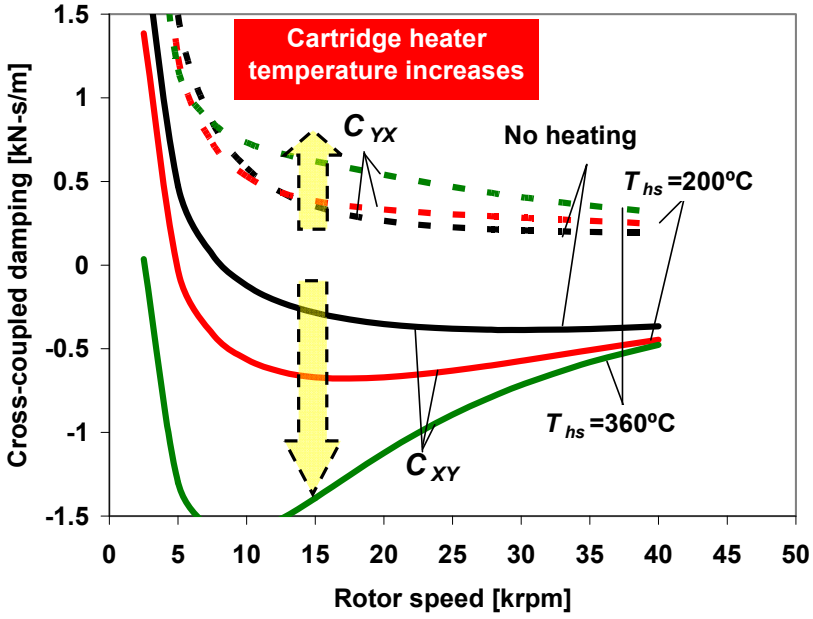

(b) Cross-coupled damping

Fig. 16 (a) Direct damping and (b) cross-coupled damping for drive end GFB versus rotor speed for operation at ambient condition (no heating) and with cartridge heater set temperature (T_{hs}) at 200 °C and 360 °C. Static load 6.5 N. No forced cooling flow.

A finite element rotordynamics model integrates the linearized GFB force coefficients to predict the synchronous responses of the test rotor and for operation with increasing heater temperatures. Figure 17 shows the finite element structural model of the test rotor. The model accounts for the temperature induced changes in material properties (rotor and connecting rod). The hot rotor-GFB test rig uses a stiffer flexible coupling than that used in the original test rig, see Ref. [4]. The old and current couplings have experimentally estimated lateral stiffness coefficients of 1 N/mm and 4 N/mm, respectively. The original connecting rod [4] is also replaced with a slightly longer one of the same material, i.e., old and new connecting rods have lengths of 46 mm and 51 mm, respectively. The modifications aid to isolate the rotor - GFB system from the drive motor system.

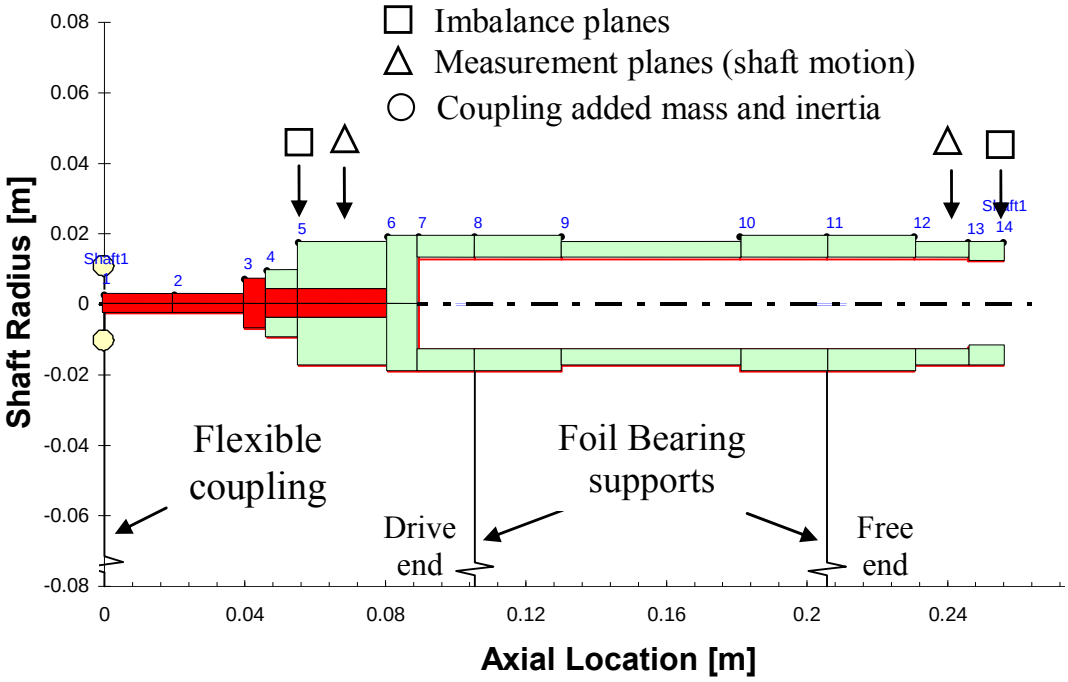

Fig. 17 Finite element model of test rotor supported on two radial GFBs (with connecting shaft and flexible coupling).

An eigenvalue analysis predicts the damped natural frequencies and damping ratios of the rotor-GFBs system over a speed range. The analysis implements the predicted (synchronous speed) stiffness and damping coefficients, see Figs. 15 and 16 and **Appendix J**. Figure 18 shows the damped natural frequency map with predicted forward mode critical speeds at 3.4 krpm and

12.5 krpm, associated to conical and cylindrical modes, respectively. The rotor bending mode at a speed of 28.2 krpm evidences the ringing of the connecting rode and coupling, i.e. a *dog tail wagging* mode*)*. Figure 19 shows the predicted damping ratios decreasing rapidly as rotor speed increases. A positive damping ratio indicates a stable system. The predicted damping ratio of ~ 0.8 at the critical speed of 12.5 krpm damps well the cylindrical mode rotor motions, while the low damping ratio < 0.2 above 10 krpm implies significant rotor conical mode motions excited by an out-of-phase imbalance distribution, as discussed earlier. Table 1 provides a summary of the predicted critical speeds and damping ratios for increasing shaft temperatures.

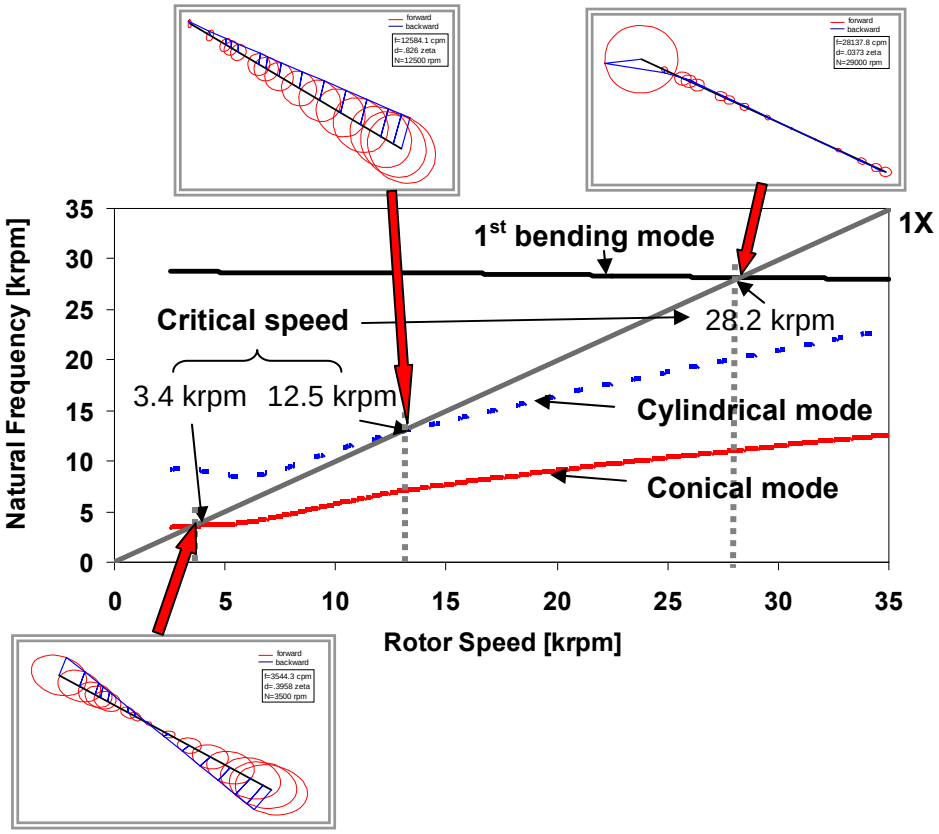

Fig. 18 Predicted damped natural frequencies for rotor – GFB system (forward modes). Operation at ambient condition (no heating). Mode shapes denoted.

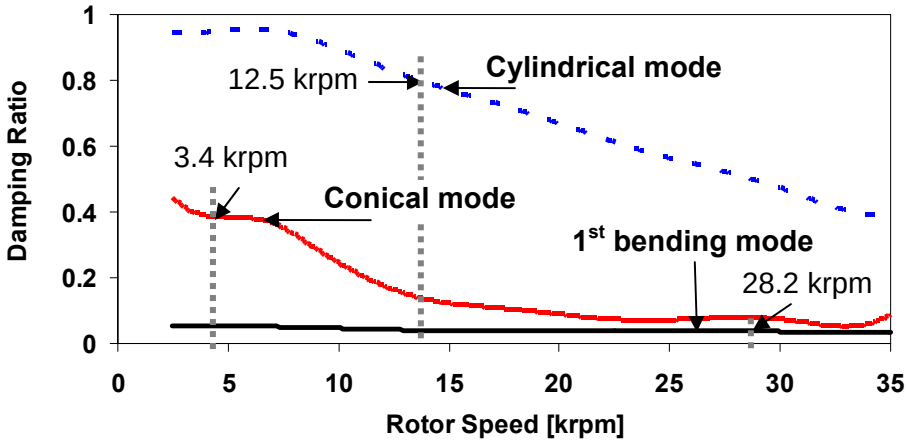

Fig. 19 Predicted damping ratios (ξ) for rotor – GFB system. Operation at ambient condition (no heating).

Table 1. Predicted critical speeds and damping ratios of rotor-GFB system for increasing shaft temperatures

Temperature			Predicted natural mode					
Heater (T_{hs})	Shaft (T_S)		Cylindrical		Conical		Flexural	
	Drive end	Free end	Critical speed	Damping ratio	Critical speed	Damping ratio	Critical speed	Damping ratio
360 °C	110 °C	150 °C	**12.5 krpm**	0.70	**22.0 krpm**	0.15	**31.5 krpm**	0.07
200 °C	67 °C	88 °C	**6.5 krpm**	0.90	**14.0 krpm**	0.84	**31.0 krpm**	0.04
21 °C (No heating)	21 °C (No heating)	21 °C (No heating)	**3.4 krpm**	0.43	**12.7 krpm**	0.82	**28.2 krpm**	0.04

Figure 20 presents the predicted and measured rotor amplitudes of rotor synchronous response for operation at ambient condition (no heating) and with the cartridge heater set temperature (T_{hs}) at 200 °C and 360 °C. No forced cooling flow is supplied during the baseline rotor speed coastdown tests shown earlier in Fig. 4 (Section 1). In the predictions (remnant) imbalance masses (m_e) = 600 mg are added into the rotor end planes, at a radius of 15.11 mm, and with angles (θ_e) = 0° and 250° at the drive and free ends.

As the heater temperature increases, the rotor amplitude decreases for rotor speeds < 15 krpm while the critical speed of the rotor-GFB system increases from 14 krpm to 17 krpm. Note that the rotor bending critical speed is above 28 krpm. In general, the model predictions agree reasonably well with the measurements. The agreement is best at rotor speeds well below the bending critical speed (~ 30 krpm), thus validating the computational model of the hot rotor – GFB system.

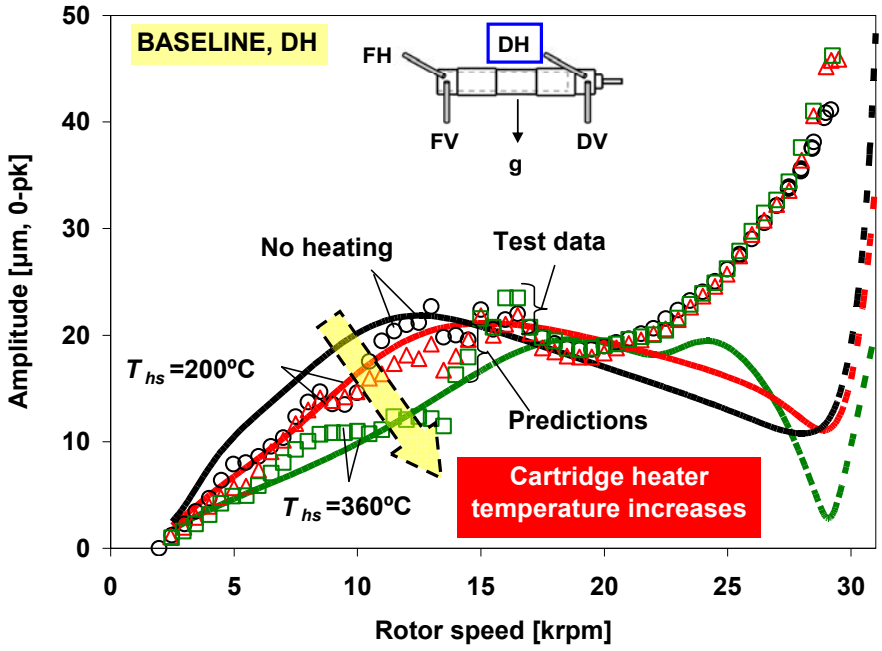

Fig. 20 Predicted and measured rotor amplitude of synchronous response for the drive end GFB versus rotor speed. Operation at ambient condition (no heating) and with cartridge heater set temperature (T_{hs}) at 200 °C and 360 °C. Static load 6.5 N. No forced cooling flow. Assumed imbalance mass (m_e) = 600 mg at a radius of 15.11 mm and both rotor drive and free ends. Assumed imbalance angle (θ_e) = 0° and 250° for the rotor drive and free ends, respectively.

CLOSURE

THD GFB model predictions reproduce with accuracy measured foil bearing temperatures in a hot shaft rotordynamic test rig. Section 1 reports the measurements. Operating conditions include increasing rotor speeds to 30 krpm, shaft OD hot temperature to 125 °C above ambient, and with increasing strength of cooling flow rates to 150 L/min into each test GFB.

Presently, predictions of GFB static load performance parameters and dynamic force coefficients versus rotor speed are provided for operation at ambient condition (no heating) and with cartridge heater set temperatures (T_{hs}) at 200 °C and 360 °C. As the shaft temperature increases, the test foil bearing temperature increases accordingly. As the heater temperature increases, the journal attitude angle, drag torque, peak film temperature, and shaft thermal growth increase, but the journal eccentricity decreases. The net-shaft thermal growth is most significant at the highest heater temperature and decreases the minimum film thickness at high rotor speeds, due to the reduction in the bearing operating clearance Note that the decrease in the bearing operating clearance reduces the bearing load capacity and increases the likelihood of thermal seizure and bearing failure. As the shaft temperature increases, the predicted direct stiffness (K_{XX}, K_{YY}) and damping (C_{XX}, C_{YY}) coefficients increase, while the difference in the cross-coupled stiffness coefficients (K_{XY} - K_{YX}) decreases at high rotor speeds. Note that the increase in (C_{XX}, C_{YY}) and the decrease in (K_{XY} - K_{YX}) are beneficial from the view point of rotordynamic stability.

A finite element (FE) model of the hot rotor supported on GFBs is developed in XLTRC^2 ©. An eigenvalue analysis predicts the system critical speeds and damping ratios for increasing shaft temperatures. In general, the predicted rotor synchronous responses based on predicted linearized bearing coefficients show good agreement with test measurements during the rotor speed coastdown test. The rotor amplitude peak decreases and the system rigid-mode critical speed increases as the shaft temperature increases. The predicted rotor bending critical speed is above 28 krpm in reasonable agreement with the measurements.

The computational physics model predictions reproduce with accuracy the measurements of bearing temperatures and rotordynamic response. The test data serves to benchmark the computational program developed, a major objective of the funded research program.

NOMENCLATURE

c	Nominal (cold) GFB radial clearance [m]
$C_{\alpha\beta}$	Bearing damping coefficients; $_{\alpha\beta=X,Y}$ [N·s/m]
$K_{\alpha\beta}$	Bearing stiffness coefficients; $_{\alpha\beta=X,Y}$ [N·s/m]
L	Bearing axial width [m]
p	Gas pressure [Pa]
R	Radius [m], D=2 R
S_C	Shaft (journal) centrifugal growth [m]
S_T	Shaft (journal) thermal expansion
T	Temperature [K]
X,Y	Inertial Cartesian coordinate system [m]
$x=R\Theta,z$	Coordinate system on plane of bearing [m]
λ	Thermal inlet mixing ratio [-]
Θ	Circumferential coordinate [rad]
Ω	Rotor angular speed [rad/s]

Subscripts

amb	Ambient
B,F,S,hs	Bearing, Foil, Shaft(Journal), Cartridge heater
C	Cooling gas flow
D,F,V,H	Drive end, Free end, Vertical, Horizontal
f	Thin gas film
i, o	Inner and outer
∞	Ambient fluid medium (stagnant)

REFERENCES

[1] San Andrés, L., and Kim, T. H., 2007, "A Thermohydrodynamic Model for Prediction of Gas Foil Bearing Performance," 1st Quarter Research Progress Report submitted to NASA SSRW2-1.3 Oil Free Engine technology Program, November.

[2] San Andrés, L., and Kim, T. H., 2008, "A Thermohydrodynamic Model for Prediction of Gas Foil Bearing Performance," 2nd Quarter Research Progress Report submitted to NASA SSRW2-1.3 Oil Free Engine technology Program, February.

[3] San Andrés, L., and Kim, T. H., Ryu, K., 2008, "A Thermohydrodynamic Model for Prediction of Gas Foil Bearing Performance," 4th Quarter Research Progress Report to NASA SSRW2-1.3 Oil Free Engine technology Program, August.

[4] San Andrés, L., and Kim, T. H., Ryu, K., 2008, "A Thermohydrodynamic Model for Prediction of Gas Foil Bearing Performance," 3rd Quarter Research Progress Report to NASA SSRW2-1.3 Oil Free Engine technology Program, May.

[5] San Andrés, L., and Kim, T. H., Ryu, K., 2009, "A Thermohydrodynamic Model for Prediction of Gas Foil Bearing Performance," 6th Quarter Research Progress Report to NASA SSRW2-1.3 Oil Free Engine Technology Program, February.

SECTION 3
MEASUREMENT OF MITI® FBS STRUCTURAL STIFFNESS

By RA: Keun Ryu, Edited by P.I Luis San Andrés

Regardless of the operating conditions, namely shaft speed, applied load and surrounding temperature, the FB underspring[1] structure dominates the static and dynamic force performance of GFBs [1,2]. A series of static load deflection tests are conducted with the Korolon™ coated MiTi foil bearings to determine their structural stiffness. Three shafts of differing diameters are employed to give bearing configurations of increasing clearances.

Table 1 lists the measured or estimated dimensions of both test bearings and the shafts for bearing-shaft configurations labeled as 1 through 3. A bearing consists of an arcuate top foil, a bump foil strip and a cartridge shell [3][2]. Fig. 1 taken from Ref.[4] depicts the bearing components. The bearing vendor only provided dimensions of the bearing shell outer diameter (1.760 in [44.704 mm]) and axial length (1.1 in [27.94 mm]). Korolon™ 800 coating, maximum operating temperature of 800°F (426°C), is applied on the top foil surface. The underspring system has three bump strip layers extending along the axial length. The bump strip layers, each with 24 bumps, lay around the bearing shell inner circumference. The ends of the top foil and underspring layers are spot welded to the bearing shell. The other ends are free. Reference [5] details the tribological characteristics of Korolon™ coating. Note that the bearing vendor recommends a journal bore diameter of 1.4375 inch (36.513 mm). The bearing axial length (25.4 mm) is smaller than the bearing shell length (27.94 mm).

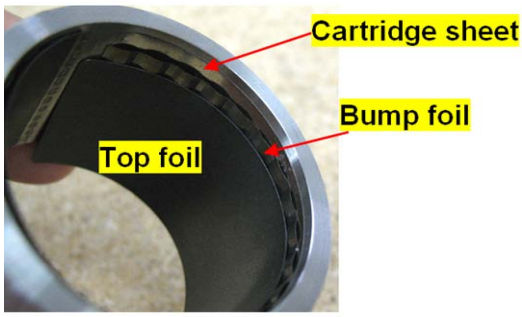

Fig. 1 Top foil, bump foil strip and cartridge sheet in MiTi foil bearing. Taken from [4]

[1] The underspring structure consists of the preformed top foil and the bump strip layers held inside the bearing cartridge

[2] The manufacturer placed a thin metal sheet (0.051 mm) underneath the bump strip layers and in contact with the bearing shell ID. The metal sheet serves to adjust the bearing foil stack-up height, i.e., to achieve the desired final nominal bearing clearance [3]. Both ends of the metal sheet are spot welded to the ID of the bearing shell.

Shaft 1 (*S*1) denotes the hollow rotor which will be used in the upcoming rotordynamic test. The rotor outer diameter is 36.453 mm at the location of the drive end (DE) bearing and 36.461 mm at the free end (FE), respectively. Configuration 1 includes foil bearing 1 (serial# 90203C001-1) installed on the rotor drive end side. Configuration 2 takes foil bearing 2 (serial# 90203C001-2) installed on the rotor free end side.

Configuration 3 implements another hollow shaft (*S2)* with an outer diameter of 36.555mm, i.e., ~100 μm larger OD than the rotor used in configurations 1 and 2. Both hollow shafts, *S*1and *S*2, are made of AISI 4140 steel and machined to give a polished surface with average roughness R_{RMS} at 10 μ-in [6].

Bearing *B*2 (serial#: 90203C001-2) and shaft *S*2 were used in the dynamic load tests detailed in the 5th quarter research progress report [7]. The bearing shell ID of *B*2 is 60 μm smaller than the ID of *B*1[3]. Each test bearing fits into an outer shell[4] with thickness of 3.08mm. The thick outer shell contains holes for connections to a load cell and accelerometer and axial slots for installation of thermocouples.

[3] The original bearing cartridge ID of bearing *B*2 is 37.984 mm, as reported in [4]. Presently, the cartridge ID reduced permanently to 37.921 mm, a decrease by ~63 μm [8], after being press-fitted into the thick bearing shell [7].

[4] The bearings are sliding-fitted into the outer shell without any perceptible play, i.e., close sliding fit (*RC*1 class according to standard clearance fit from ANSI Standard B4.1 [8]). Note that the bearing shell ID does not decrease after a sliding fit (*RC*1 = zero clearance fit).

Table 1. Dimensions for shafts and MiTi foil bearings. Unit: mm

System designation	**System configuration 1**	**System configuration 2**	**System configuration 3**
Shaft#	Shaft 1 (*S*1)	Shaft 1 (*S*1)	Shaft 2 (*S*2)
Shaft outer diameter	36.453 ± 0.0025 mm	36.461 ± 0.0025 mm	36.555 ± 0.0025
Shaft inner diameter	17.89 ± 0.005 mm	18.01 ± 0.005 mm	25.50 ± 0.005
Bearing# Test setup in Fig. 2	Bearing 1 (*B*1): serial# 90203C001-1	Bearing 2 (*B*2): serial# 90203C001-2	Bearing 2 (*B*2): serial# 90203C001-2
Bearing sleeve outer diameter, D_O	44.635	44.575	44.575
Bearing sleeve wall thickness, t_B	3.327	3.327	3.327
Bearing sleeve inner diameter, $D_I = D_O - 2\ t_B$	37.981	37.921	37.921
Bearing (Top foil) axial length, L	25.4	idem	idem
Bearing sleeve axial length, L_O	27.94		
Top foil thickness, t_T	0.127		
Cartridge sheet thickness, t_{CS}	0.051		
Bump foil thickness, t_B	0.102		
Number of Bumps, N_B	24 × 3 axial		
Bump pitch, s_0 (deg)	4.64		
Bump length, l_B	3.950		
Bump height, h_B	0.510		
Bump arc radius, r_B	4.079		
Bump arc angle, α (deg)	58		
Top foil inner diameter, D	36.605	36.545	36.562
Radial clearance	**0.076**	**0.042**	**-0.005**
System designation	**System configuration 1**	**System configuration 2**	**System configuration 3**

Material Elastic Modulus=214 [GPa], Poisson Ratio=0.3

Figure 2 depicts photographs of the test setups to apply static, push and pull, loads into each FB resting on its shaft. Figure 3 shows in a schematic view the procedure to apply loads on a bearing. Quarter 4 research progress report details the test setup and experimental procedure [9]. To minimize the shaft elastic deflection under static loads, both ends of the shaft are secured to the lathe. A lathe tool holder displaces manually to deliver a static load on the bearing. A strain gauge load cell (uncertainty 0.45 N) is affixed to the lathe tool holder and connected to the test bearing outer shell through a flexible string and two hollow tubes. Moving the lathe tool holder forward and backward provides compression and tension forces onto the test bearing,

respectively. An eddy current displacement sensor (uncertainty: 0.104 V/mm) facing the bearing OD measures the displacements of the test bearing. Note that the experiments are performed at room temperature. For every test, the orientation of the bearing top foil spot weld is 90º away from the direction of the static load.

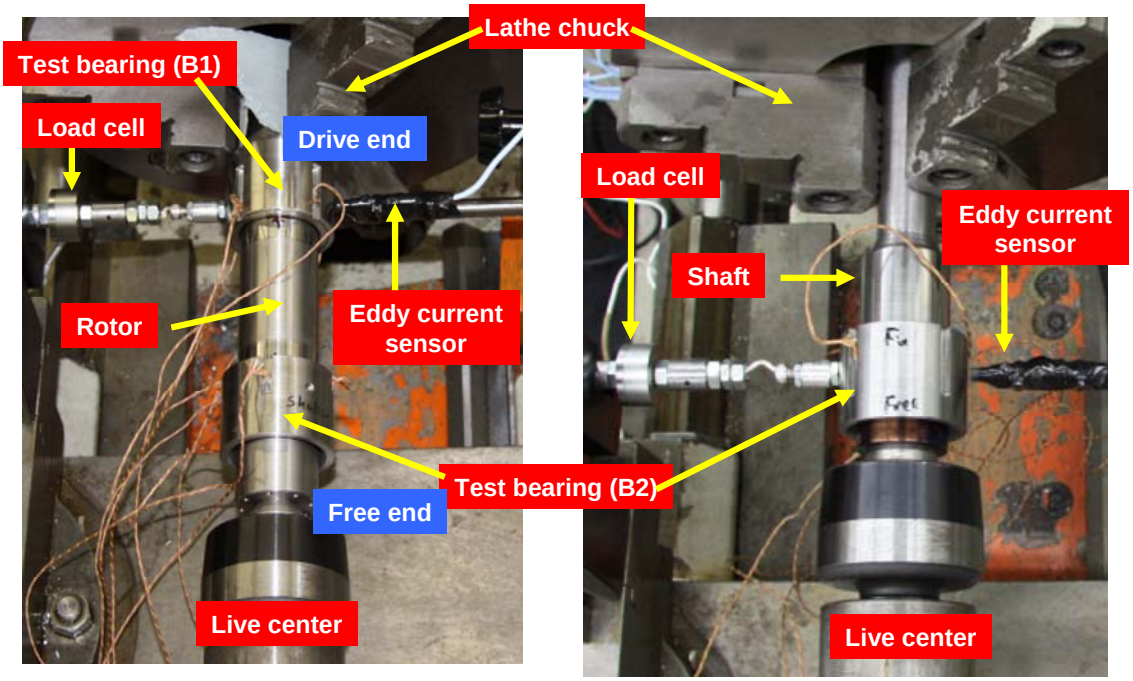

Test setup 1 Test setup 2

Fig 2. Test setups for FB static pull-push load tests. 1: Bearings *B*1 and *B*2 and shaft *S*1. 2: Bearing *B*2 and shaft *S*2

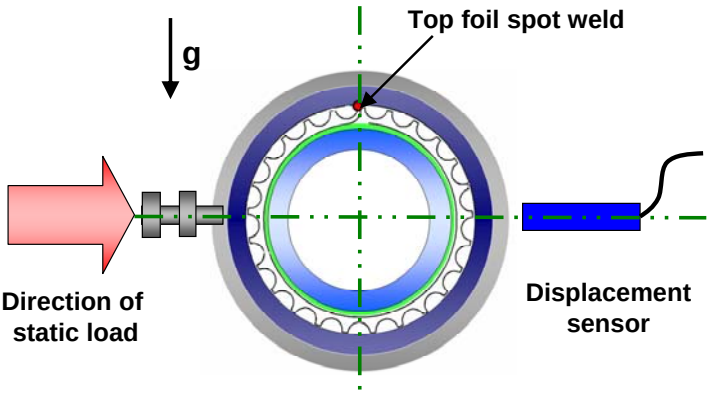

Fig. 3 Schematic view of setup for static load and FB structural deflection test. Load 90º away from spot weld

TEST RESULTS

The measurements are conducted at room temperature. Figure 4 depicts the measured FB deflection versus applied load for configurations 1 through 3 during three consecutive loading-unloading cycles. Note that measured shaft displacements, detailed in **Appendix L,** are subtracted from the corresponding FB displacements to obtain the actual FB deflection. In the results, the deflection varies nonlinearly with load and the area under a hysteresis loop represents lost mechanical energy. Dry-friction from sliding contacts between the bumps and top foil and the bumps and cartridge sheet provides the characteristic energy dissipation.

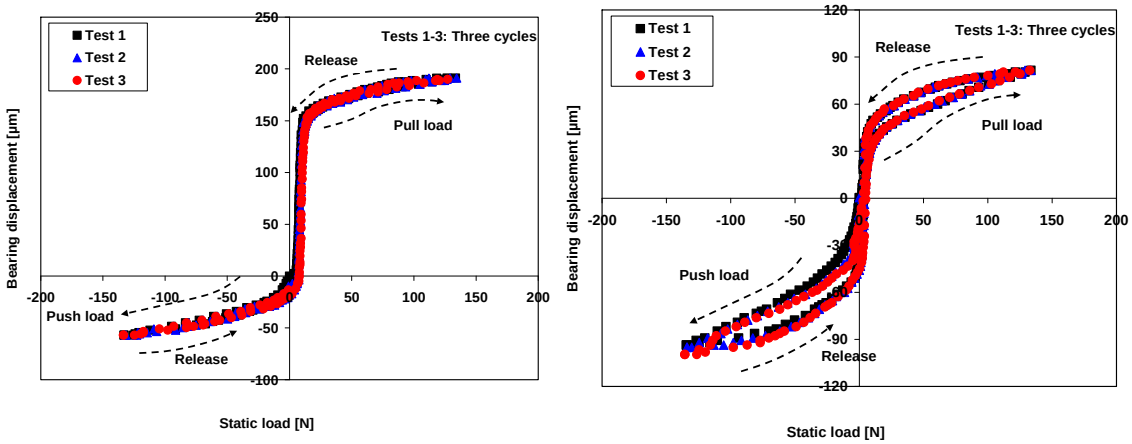

(a) System configuration 1
Radial clearance ~ 0.076 mm

(b) System configuration 2
Radial clearance ~ 0.042 mm

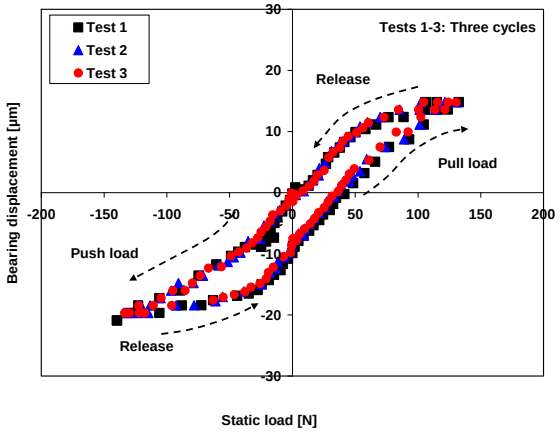

(c) System configuration 3
Radial clearance ~ -0.005 mm

Fig. 4 Recorded FB deflection versus static load for configurations 1 through 3. Data for three cycles of loading-unloading shown. Note different vertical (deflection) scales.
Radial clearance (mm) C1: 0.076 C2: 0.042 C3: -0.005

Figure 5 places together the deflection versus static load measurements for the three test configurations to evidence the differences in clearance, mainly. Configurations 1 and 3 show the largest and smallest radial play or sway space, respectively, as expected. Recall from Table 1 that the bearing clearances derived from geometrical dimensions are 0.076 mm, 0.042 mm and -0.005 mm for configurations 1, 2 and 3, respectively. Note that configuration 2 shows the largest area within its hysteresis loop; hence it has the largest energy dissipation characteristics. In configuration 3, the test FB is highly preloaded (assembly interference), with the shaft OD being larger than the top foil ID[5].

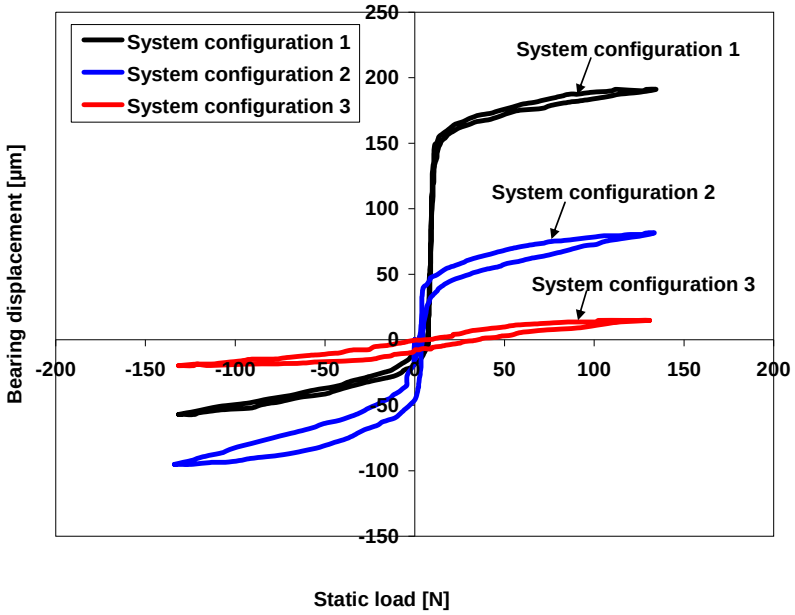

Fig. 5 Superposition of FB deflection vs. load for three test configurations

ESTIMATION OF FB STRUCTURAL STIFFNESS

A cubic polynomial curve fit over the span of applied loads establishes an analytical relation between the static load and the FB deflection; i.e., $F=F_0+K_1 x+K_2 x^2+K_3 x^3$. The FB structural stiffness is $K=\partial F/\partial x= K_1+2K_2 x+3K_3 x^2$. For configuration 1, however, the load-FB deflection curve cannot be estimated by a polynomial curve fit due to the large clearance, i.e. the very soft elastic foundation region, ~ 140 µm. Hence, dividing small changes in static load by the

[5] In general, the preload ensures even contact at the static condition with uniform pressures pushing on the elastic structure.

corresponding changes in bearing displacements determines the static structural stiffness coefficient of the FB.

Figure 6 shows the estimated bearing stiffness K versus deflection (x) for configuration 1. The symbols denote finite differences in applied load divided by the ensuing difference in bearing deflection, $\Delta F/\Delta x$. The test results show a typical hardening nonlinearity in FB structure during the loading and unloading processes.

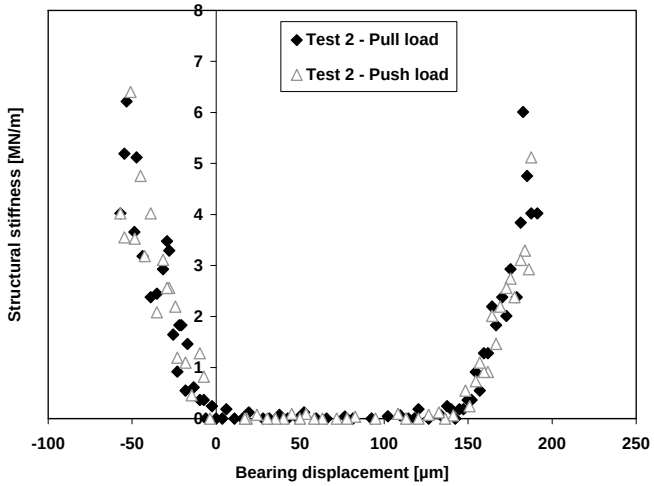

Fig. 6 Estimated FB structural stiffness *K* versus deflection for configuration 1. Stiffness determined from finite differences in applied load. (Baring clearance: 0.076 mm)

For configurations 2 and 3, Figure 7 depicts the test FB deflection versus load in the left graphs, and the bearing stiffness K derived from the curve fits in the right graphs. The correlation coefficient, R^2, indicates the goodness of the polynomial curve fit to the test data. The FB stiffness shows a distinctive hardening effect as the bearing deflection increases. Note that in configuration 3, the FB has 3~4 MN/m of structural stiffness even at null bearing deflection (and null static load, as shown in later).

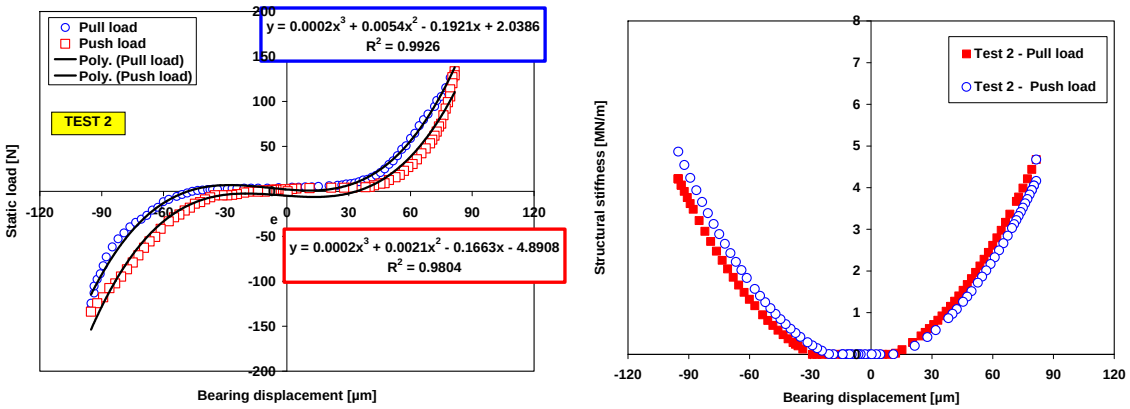

(a) Configuration 2: clearance ~ 0.042 mm

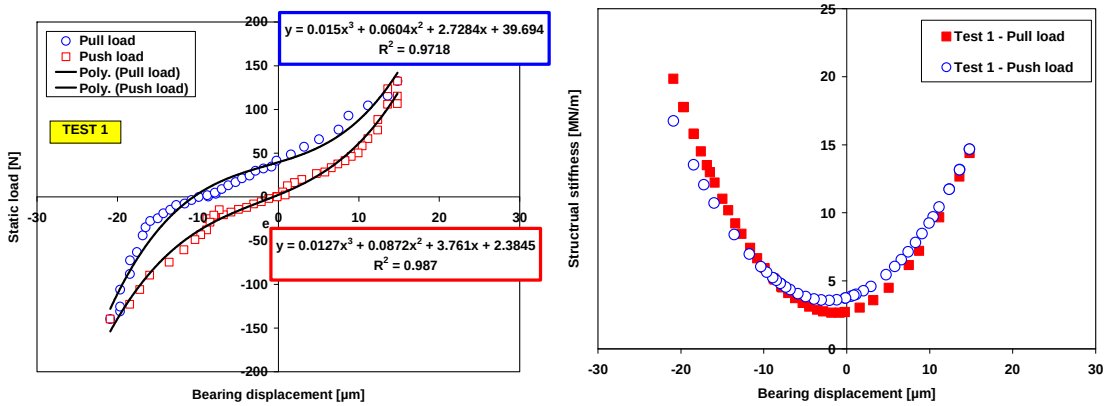

(b) Configuration 3: clearance ~ -0.005 mm

Fig. 7 Static load versus bearing deflection (test and polynomial curve fit) and estimated structural stiffness for configurations 2 and 3. Stiffness coefficients determined form spatial derivative of load versus deflection curve fit. Note different vertical and horizontal scales.

Quarter 5 research progress report [7] presents the dynamic force coefficients of MiTi bearing *B2* (serial# 90203C001-2, see Table 1) for increasing bearing deflections, excitation frequency, and shaft temperature. In Ref. [7] the test FB-shaft system represents current configuration 3, i.e., one with large assembly preload. Figure 8, taken from Ref. [7], depicts the identified FB dynamic stiffness for increasing FB motion amplitudes versus frequency and at ambient temperature. The FB stiffness is frequency dependent and decreases with excitation frequency and magnitude of FB displacement.

Figure 9 compares the identified FB static stiffness, shown in Fig. 7, with the dynamic stiffness obtained at 50 Hz frequency, see Fig. 8. At 7.4 µm FB deflection, the static and dynamic stiffnesses match closely. However, at larger FB deflections, the static stiffness is

higher than the dynamic stiffness. In general, the FB static stiffness is higher than the dynamic stiffness since the static dry friction coefficient is higher than the kinetic dry friction coefficient [10,11].

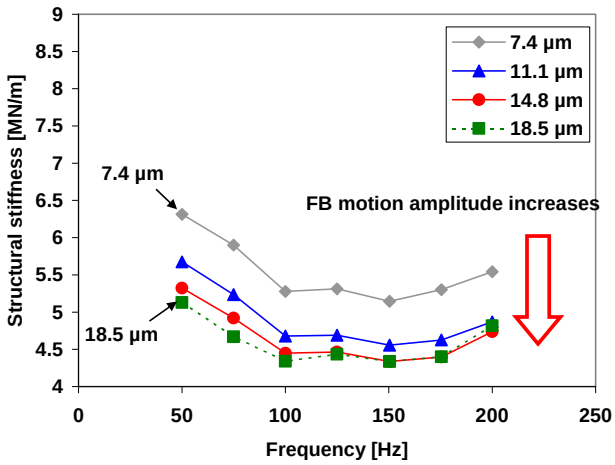

Fig. 8 Taken from Ref. [7]: FB dynamic structural stiffness versus excitation frequency for FB motion amplitudes of 7.4, 11.1, 14.8, and 18.5 µm. Tests at room temperature. Configuration 3

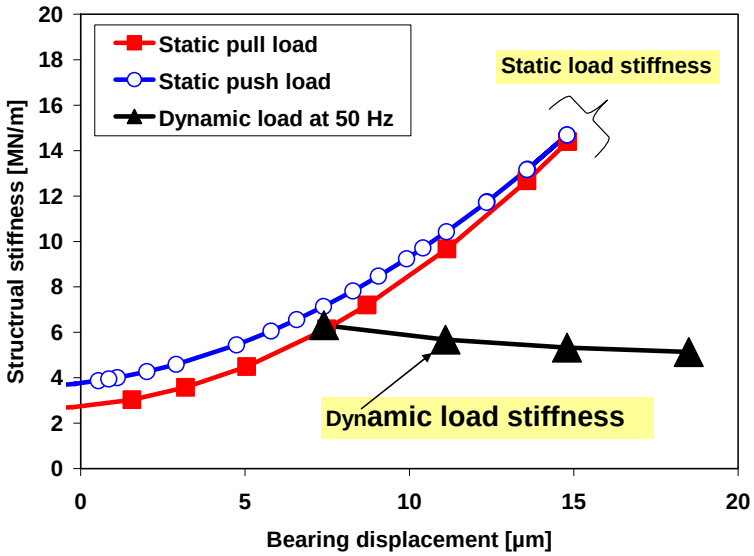

Fig. 9 Comparison of static and dynamic FB stiffness versus FB deflection. Configuration 3 (with large preload).

Figure 10 depicts the identified FB structural stiffnesses versus applied loads. The FB structural stiffness is strongly load-dependant since the bumps gradually activates as the static

load increases, i.e., piece-wise linear hardening effect. Asymmetry of the identified coefficients with respect to above or below the null load condition is distinctive in system configuration 3. For system configurations 1 and 2, the FB structural stiffness versus static load shows almost similar curve. The maximum FB structural stiffness at the largest applied load (~140 N) for system configurations 1 and 2 are ~ 5MN/m. On the other hand, the identified coefficients in system configuration 3 range up to ~20 MN/m. For system configuration 3, an initial assembly preload, which is interference between the shaft and top foil, increases the FB static stiffness. The structural stiffness is piecewise linear depending on the contact area for a given load and assembly preload [12].

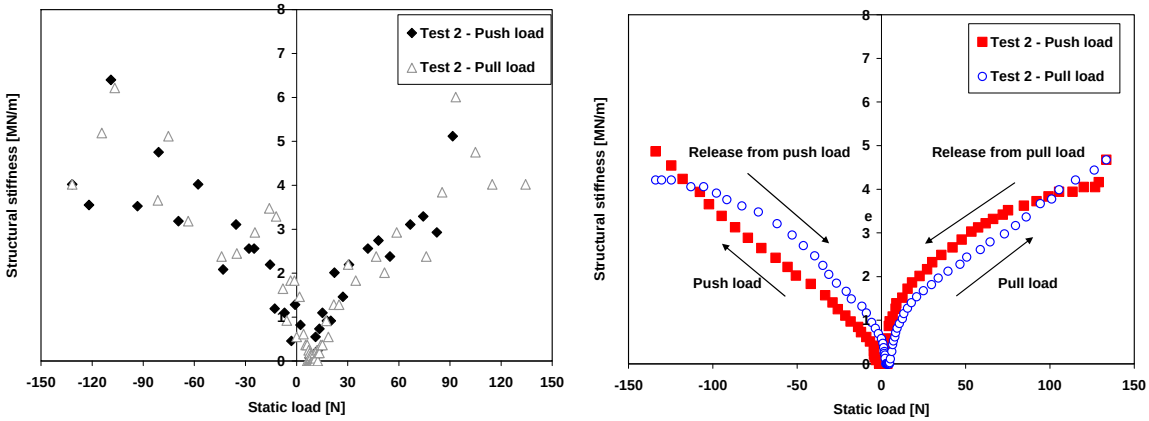

(a) Configuration 1
Clearance ~ 0.076 mm

(b) Configuration 2
Clearance ~ 0.042 mm

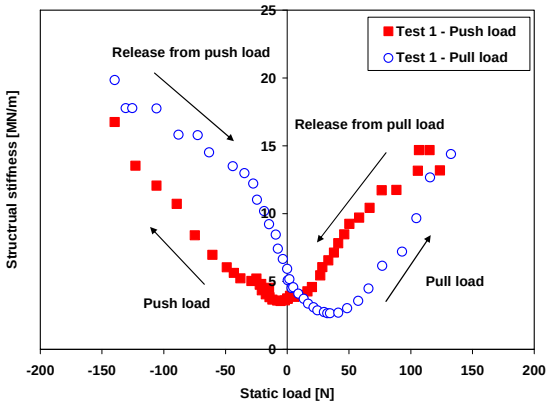

(c) **Configuration 3 (with large assembly preload)**
Radial clearance ~ -0.005 mm

Fig. 10 Foil bearing structural stiffness versus static load for three shaft-bearing configurations. Tests at room temperature.

Test configurations 1 and 2 refer the rotor-FB system which will be operated in high temperature rotordynamic test rig. Hence, the "ad-hoc" nominal FB radial clearance, taken from the report by Ruscitto et al [13][6], can be estimated from Fig. 4. The nominal radial clearances are determined as ~75μm and ~35μm for configurations 1 and 2, respectively. The clearances derived from geometry are 76 μm and 42 μm, see Table 1. The agreement is remarkable. The FB in configuration 3 has an assembly interference, i.e., no initial clearance. The assembly interference, particularly highly preloaded condition, significantly increases the estimated static stiffness over the applied load range. Note that in practice most FBs will have assembly interference between the components.

References [10,12] detail a FB structural model and the identification procedure for estimation of FB static stiffness coefficients. Iordanoff's single bump stiffness model[7] [14] assembles individual bump stiffness as the FB becomes loaded. The bump pitch, length, arch radius and arch angle are estimated from the zoomed photographs shown in Ref. [4]. The inner diameter (D) and "geometrical" radial clearance (C) of the bearing are calculated from the parameters in Table 1. For the current test FBs, an assumed dry friction coefficients μ_f=0.2 delivers the best agreement with the measurement results.

For configurations 1 and 2, Figs. 11 and 12 show the predicted FB structure stiffness coefficient versus static load and compares the test data to the model predictions. The predictions show a remarkable agreement with the test data.

[6] For determination of the GFB clearance by a load deflection test, Ruscitto et al [13] apply the static load which corresponds to the load on the bearing due to the weight of the bearing housing and load support mechanism. Note that the clearance is controlled by inserting an adjustment shim between the bump foil strip and the bearing cartridge.
[7] Iordanoff's model ignores the interaction between adjacent bumps and assumes a constant bump pitch.

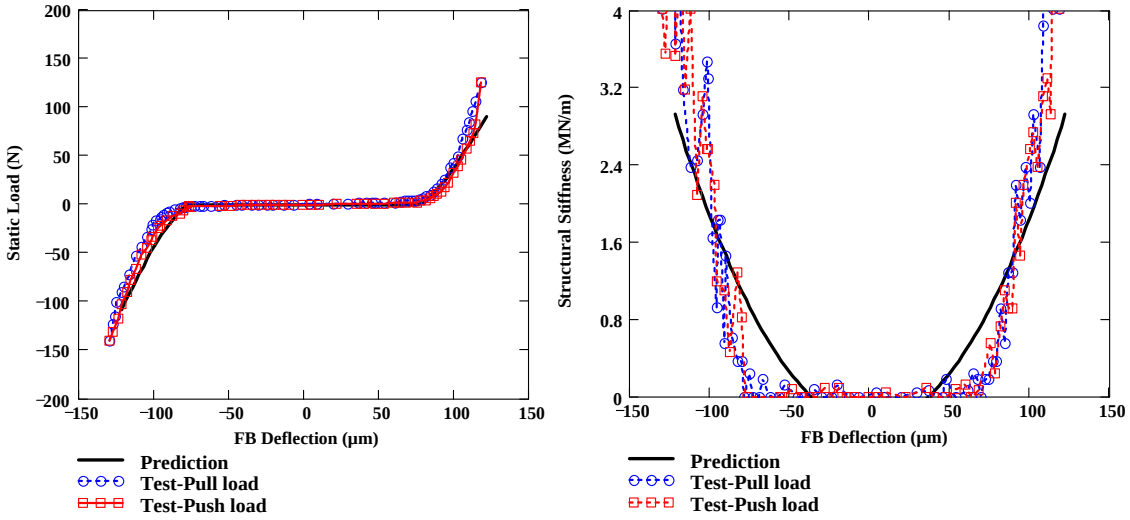

Fig. 11 Configuration 1: Predicted and experimentally derived static load and FB structural stiffness versus deflection. (μ_f=0.2)

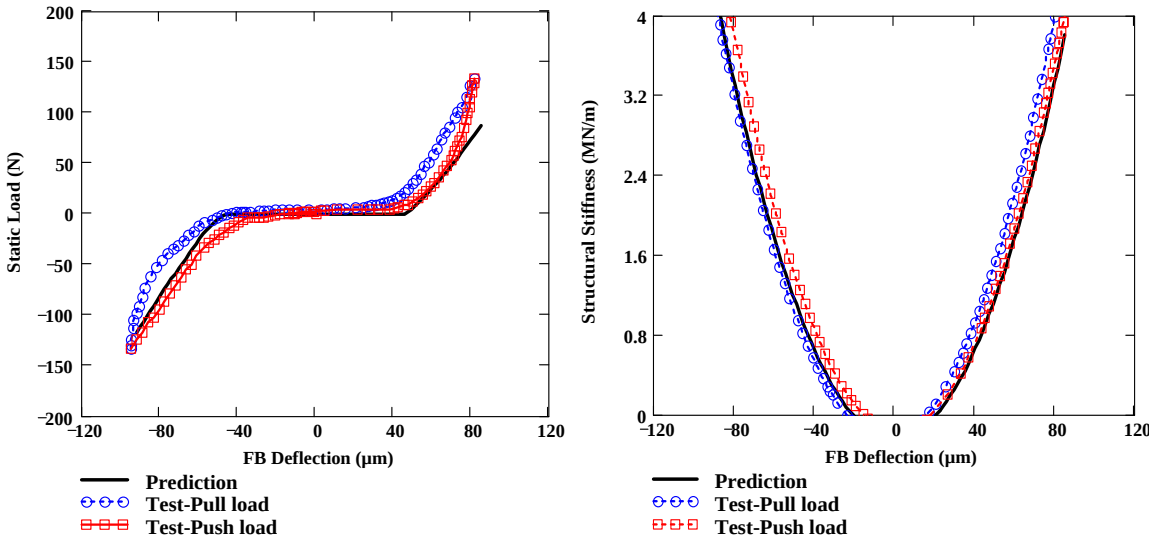

Fig. 12 Configuration 2: Predicted and experimentally derived static load and FB structural stiffness versus deflection (μ_f=0.2)[8].

CLOSURE

Section 3 presents static load versus bearing deflection tests to estimate the structural stiffness of two MiTi FBs. The tests were performed at room temperature; hence the effect of the high temperature top foil coating (Korolon®) is of no consequence in the experiments. Two

[8] The recorded FB displacement in Fig. 12 is shifted by 73 μm so that the center of the hysteresis loop coincides with the origin of the FB displacement coordinate. Note that the FB geometric center relative to the stationary shaft is unknown, thus the push load starts from an arbitrary offset displacement.

configurations pairing the test rotor with a respective foil bearing, at the drive end or free end sides, show an actual clearance, i.e. the rotor OD is smaller than the FB top foil ID. A third configuration pairs a FB with a larger OD shaft resulting in assembly interference. The static load measurements show different FB deflection versus load characteristics depending on whether the system has an actual clearance of a preload. The FB structural stiffness increases nonlinearly as the bearing deflection increases. Predictions of FB stiffness based on Iordanoff's single bump stiffness formulas, agree very well with the measurements.

Presently, further rotordynamic performance and bearing/rotor temperature measurements in the hollow test rotor supported on the MiTi FBs are being performed. The measurement results will reveal experimental rotordynamic force coefficients for the test foil bearings. An upcoming technical report will present further comparisons of measurements to predictions in order to further benchmark the computational GFB predictive model.

REFERENCES

[1] Kim, T. H., San Andres, L, 2006, "Limits for High-Speed Operation of Gas Foil Bearings," ASME J. Tribol., **128**, pp. 670-673.,

[2] Kim, T. H., San Andres, L, 2007, "Analysis of advanced gas foil bearings with piecewise linear elastic supports," Tribol. Int., **40**(8), pp. 1239-1245.

[3] Heshmat, H., 1999, "High Load Capacity Compliant Foil Hydrodynamic Journal Bearing," US Patent 5,988,885.

[4] San Andrés, L., and Kim, T. H., 2008, "A Thermohydrodynamic Model for Prediction of Gas Foil Bearing Performance," 3rd Quarter Research Progress Report submitted to NASA SSRW2-1.3 Oil Free Engine Technology Program, June.

[5] Heshmat, H., Hryniewicz, P., Walton, J. F., Willis, J. P., Jahanmir, S., DellaCorte, C., 2005, "Low-Friction Wear-Resistant Coatings for High-Temperature Foil Bearings," Tribol. Int., **38**, pp. 1059-1075.

[6] Oberg, Erik, Jones, Franklin D., Horton, Holbrook L., Ryffel, Henry H., 2008, *Machinery's Handbook (28th Edition) & Guide to Machinery's Handbook*, Industrial Press Inc, NY., pp. 713.

[7] San Andrés, L., Kim, T. H., and Ryu, K., 2008, "A Thermohydrodynamic Model for Prediction of Gas Foil Bearing Performance," 5th Quarter Research Progress Report submitted to NASA SSRW2-1.3 Oil Free Engine Technology Program, November.

[8] Mott, R. L., 1999, *Machine Elements in Mechanical Design, Third Edition*, Prentice-Hall, Inc., Upper Saddle River, NJ., pp. 529-532.

[9] San Andrés, L., Kim, T. H., and Ryu, K., 2008, "A Thermohydrodynamic Model for Prediction of Gas Foil Bearing Performance," 4th Quarter Research Progress Report submitted to NASA SSRW2-1.3 Oil Free Engine Technology Program, August.

[10] Breedlove, A., 2007, "Experimental Identification of Structural Force Coefficients in a Bump-Type Foil Bearing," Texas A&M University, M.S. Thesis, College Station, TX.

[11] Ku, C., and Heshmat, H., 1994, "Effects of Frequency on Structural Stiffness and Damping in a Self-Acting Compliant Foil Journal Bearing," ASME Paper No. 97-GT-100.

[12] Rubio, D., and San Andrés, L., 2006, "Bump-Type Foil Bearing Structural Stiffness: Experiments and Predictions," ASME J. Eng. Gas Turbine Power, **128**, pp. 653-660.

[13] Ruscitto, D., Mc Cormick, J., and Gray, S., 1978, "Hydrodynamic Air Lubricated Compliant Surface Bearing for an Automotive Gas Turbine Engine I-Journal Bearing Performance," NASA, Report No. CR-135368.

[14] Iordanoff, I., 1999, "Analysis of an Aerodynamic Compliant Foil Thrust Bearing: Method for a Rapid Design," ASME J. Tribol., **121**, pp. 816-822.

APPENDIX A . THERMAL ENERGY TRANSPORT MODEL IN GAS FOIL BEARINGS

Figure A.1 shows the schematic view of a bump-type foil bearing supporting a rotating hollow shaft. The graph depicts the coordinate systems and major components of the GFB. For generality, two cooling gas flow streams are supplied as noted. Figure A.2 illustrates a cross-sectional view of the GFB with the cooling streams, inner and outer. For purposes of the discussion below, consider – as in a gas turbine – the shaft is at a high temperature T_S due to a heat conducted from a hot section. The two cooling streams are:

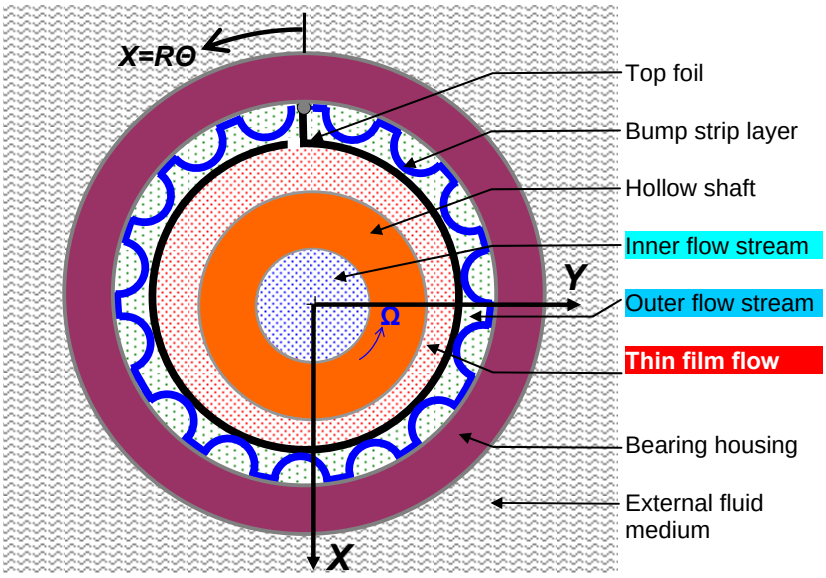

Fig. A.1. Schematic view of bump type gas foil bearing and shaft. Coordinate systems, major components and cooling flow streams

(a) **Inner flow stream,** at supply temperature and pressure $\left(T_{C_i}, P_{C_i}\right)$ flowing through the hollow shaft to cool directly the shaft inner surface at temperature T_{S_i} ; and/or

(b) **Outer flow stream,** at supply temperature and pressure $\left(T_{C_o}, P_{C_o}\right)$ flowing axially through one end of the FB structure to cool directly the back face of the top foil at temperature T_{Fo}. Along the bearing axial coordinate $\left(0 \le z \le L\right)$, the outer stream temperature (T_O) increases as it removes heat, while its pressure (P_O) decreases to ambient condition (P_a).

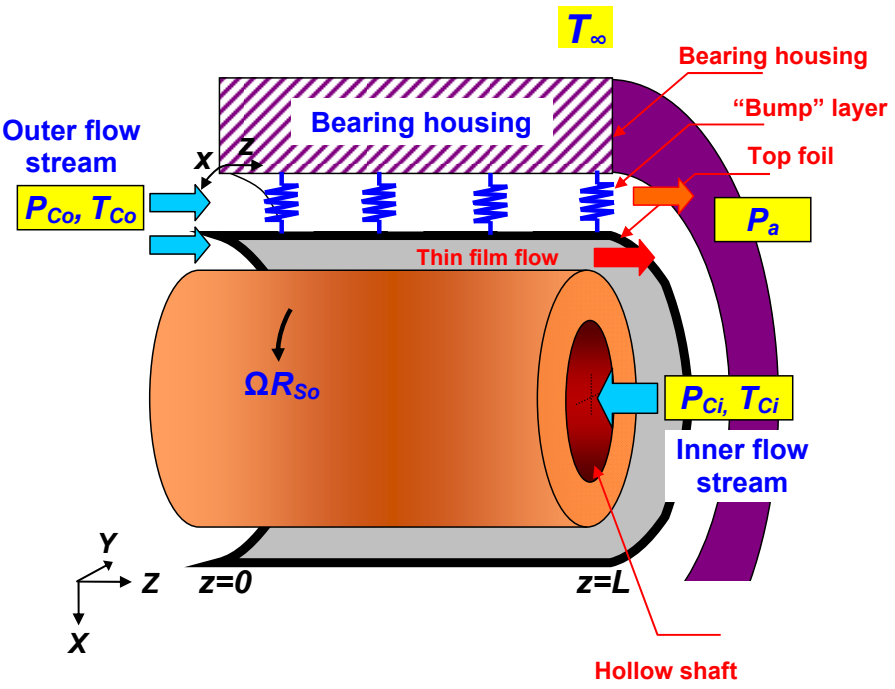

Fig. A.2. Schematic view of cooling flows in gas foil bearing: inner cooling stream (T_{Ci}, P_{Ci}) flows through hollow shaft; and outer cooling stream (T_{Co}, P_{Co}) flows through thin film region and underneath top foil. Outer cooling flow exits to ambient pressure (P_a)

Importantly enough, there is also pressurized gas flowing axially through the **thin film region** separating the rotating shaft from the topfoil front face. In this region, the gas hydrodynamic film pressure (P_f) is generated while its temperature (T_f) varies. The outer stream $\left(T_{C_o}, P_{C_o}\right)$ also sets the inlet or entrance conditions into the thin gas film. Note that the inner gas film is characterized by a minute film thickness (h_f), while the outer flow underneath the top foil has a larger gap with characteristic length equal to a bump foil height (Δ_B).

Within the thin gas film, mechanical power generated by fluid drag and heat convected from the *hot* shaft is removed[1] by the inner film gas flow and also conducted through the top foil at temperature T_F. The outer cooling stream, at temperature T_O increasing axially, advects part of

[1] This assertion implies the gas film is at a lower temperature than the shaft outer surface. The opposite case, i.e. where thermal energy flows from the film into the shaft, requires the shaft to be at a lower temperature and an inner cooling stream. Note that a solid shaft (journal) becomes a source or sink of thermal energy for the cases described above, respectively.

the conducted heat; while the remnant heat flows through conduction into the bearing housing at temperature $T_{B,}$ and disposed into an external fluid medium at temperature T_{∞}.

In practice, however, one or the other cooling methods are implemented. It would not be efficient to implement both methods at once.

THERMOHYDRODYNAMIC MODEL FOR PREDICTION OF GFB PERFORMANCE

Refer to Figures A.1 and A.2 for a geometrical depiction of the foil bearing, coordinate systems, and nomenclature for the cooling streams, inner and outer. Figure A.3 shows the nomenclature for the temperatures in the gas foil bearing and shaft system. Consider:

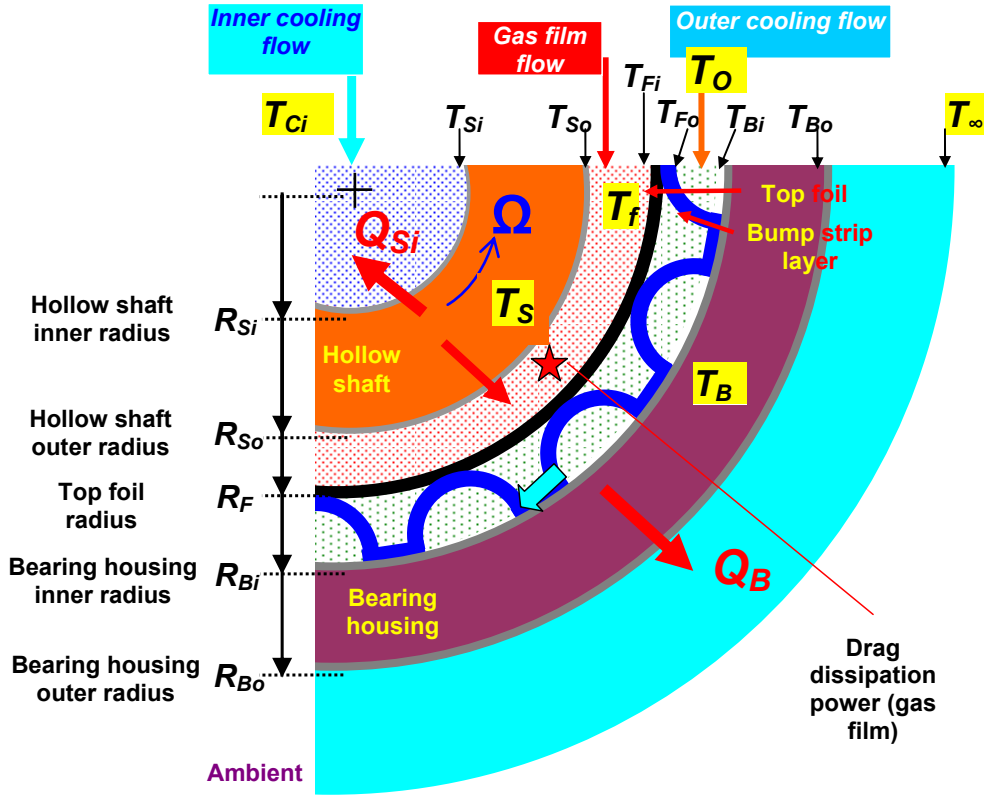

Fig. A.3. Nomenclature for temperatures in gas foil bearing, hollow shaft, bearing shell, and cooling flow streams

a) Ideal gas with density $\rho = P/\Re_g T$, where P and T denote absolute pressure and temperature, and $\Re_g$ is the gas constant.

b) Gas viscosity (μ) is a function of absolute temperature only, i.e. $\mu = \alpha_v T$.
c) Gas Specific heat (c_p) and thermal conductivity (κ_g) determined at an effective temperature and regarded as invariant in the thermal process.

A bulk-flow model describes best the transport of thermal energy. Hence, the noted pressures and temperatures below represent meaningful averages across the film thickness. This assumption is less restrictive for the pressure than for the temperature. The gas flow paths modeled include:

(a) **Thin film gas region**, between rotor surface and top foil, generating the hydrodynamic pressure field $\left(P_{f_{(\Theta,z)}}\right)$ able to support static and dynamic loads. In this region, the gas film temperature $\left(T_{f_{(\Theta,z)}}\right)$ increases due to the dissipation of mechanical energy from viscous drag, and importantly enough, due to convection of heat from the *hot* shaft and carried away by the gas film flow. In addition, some heat also flows into the top foil, part of it advected by the outer flow stream and with the rest conducted into the bearing shell.

(b) **Outer cooling flow stream region** supplied axially at one bearing end with feed conditions $\left(T_{C_o}, P_{C_o}\right)$. This cooling stream increases in temperature $\left(T_{O(\Theta,z)}\right)$, as it removes heat from the back surface of the top foil; while its pressure $\left(P_{O(\Theta,z)}\right)$ decreases toward ambient pressure P_a, as it exits the other end of the bearing ($z=L$).

(c) **Inner cooling flow stream region** at uniform *cold* temperature $\left(T_{C_i}\right)$ In this region, typically of a large diameter, enough gas flow is supplied so that its temperature does not vary along the axial direction.

Hydrodynamic pressure and temperature transport within thin film gas flow region

The gas film thickness $\left(h_{f_{(\Theta,z)}}\right)$ separating the rotor from the topfoil is very small compared to the shaft outer radius $\left(R_{S_o}\right)$ and bearing axial length (L). Furthermore, the gas kinematic viscosity ($\upsilon=\mu/\rho$) is relatively large, and hence the flow regime within the gas film region is

typically laminar and not influenced by fluid inertia. That is, the characteristic Reynolds number based on shaft angular speed (Ω) is relatively small, i.e. $\mathrm{Re}_h^* = \dfrac{\Omega\, h_f^2}{\nu} < 1$.

Under these considerations, the gas film mass flow rates $\left(\dot{m}_{x,z}\right)$ along the circumferential $\left(x = R_{S_o}\Theta\right)$ and axial *(z)* directions are:[2]

$$\dot{m}_{x_f} = \left(\rho\, h\, U\right)_f = \rho_f\, h_f \left(U_m - \frac{h_f^2}{12\,\mu_f}\frac{\partial P_f}{\partial x} \right); \quad \dot{m}_{z_f} = \left(\rho\, h\, W\right)_f = \rho_f\, h_f \left(-\frac{h_f^2}{12\,\mu_f}\frac{\partial P_f}{\partial z} \right) \quad (1)$$

where $U_m(z) = \dfrac{\Omega\, R_{S_o}}{2}\left(1 - e^{-\delta z}\right) + \alpha_\Omega\, \Omega\, R_{S_o}\, e^{-\delta z}$ with $\delta = \dfrac{12\,\mu_f}{(\dot{m}_z h^2)_f}$ is the mean circumferential flow velocity [1,2], proportional to shaft surface speed and evolving in the axial direction due to the imposed pressure gradient from the outer cooling flow. Above, α_Ω is an empirical inlet flow pre-swirl factor.

The gas film thickness (h_f) for an aligned journal (shaft) is

$$h_f = c_{(z)} + e_X \cos\left(\Theta\right) + e_Y \sin\left(\Theta\right) + w_d \quad (2)$$

where c is the bearing operating clearance[3], (e_X, e_Y) are journal center displacements, and w_d is the deflection field of the bearing underlying elastic support structure. w_d is proportional to the pressure differential $\left(P_f - P_O\right)$ and a function of the material, thickness and geometry of the top foil -modeled with shell FEs- and coupled to the stiffness of the bump-strip layers. See Refs. [3,4] for details on the analysis.

The mass continuity equation for the thin film bulk-flow establishes

$$\frac{\partial}{\partial x}\left(\dot{m}_{x_f}\right) + \frac{\partial}{\partial z}\left(\dot{m}_{z_f}\right) + \frac{\partial}{\partial t}\left(\rho_f\, h_f\right) = 0 \quad (3)$$

Substitution of Eqs.(1) into Eq. (3) renders the **Reynolds equation** for generation of hydrodynamic pressure (P_f),

---

[2] Equations (1) follow from the momentum transport equations for fluid motion along the circumferential and axial directions and neglecting fluid inertia terms, as is customary in Classical Lubrication. Furthermore, the fluid non-slip condition is assumed to apply at the *walls* of the flow region. Above, *(U, W)* are bulk-flow velocities in the circumferential and axial directions, i.e. representative averages across the gas film thickness.

[3] The bearing nominal diametrical clearance equals the difference in bearing topfoil inner diameter and shaft (journal) outer diameter. However, this clearance is also a function of the acting pressure and temperature fields. Note that shaft (rotor) thermal growth and centrifugal growth due to spinning need be accounted for.

$$\frac{\partial}{\partial x}\left(\frac{h_f^3}{12\alpha_v}\frac{P_f}{T_f^2}\frac{\partial P_f}{\partial x}\right)+\frac{\partial}{\partial z}\left(\frac{h_f^3}{12\alpha_v}\frac{P_f}{T_f^2}\frac{\partial P_f}{\partial z}\right)=U_{m(z)}\frac{\partial}{\partial x}\left(\frac{P_f h_f}{T_f}\right)+\frac{\partial}{\partial t}\left(\frac{P_f h_f}{T_f}\right) \qquad (4)$$

in the flow region $\{0\le z\le L,\ \Theta_l\le\Theta\le\Theta_t\}$. Reynolds equation (4) is nonlinear and coupled to the temperature field T_f. Boundary conditions for the pressure field follow later.

The bulk-flow temperature transport equation is derived from integration across the film thickness of the 3D thermal energy transport equation as given in Ref. [5]. Refs. [6,7] detail the integration procedure rendering the following transport equation

$$c_{p_f}\left(\frac{\partial\left(\rho_f T_f\right)}{\partial t}+\frac{\partial\left(\dot{m}_{x_f} T_f\right)}{\partial x}+\frac{\partial\left(\dot{m}_{z_f} T_f\right)}{\partial z}\right)+\dot{q}_{f\to F}-\dot{q}_{S\to f}=\left(U\,h\frac{\partial P}{\partial x}+W\,h\frac{\partial P}{\partial z}\right)_f+\Phi_f \qquad (5)$$

Convection of heat by fluid flow + diffusion to bounding surfaces = compression work + dissipated energy

where
$$\Phi_f=\frac{12\mu_f}{h_f}\left\{W^2+\frac{1}{3}U_m+\left(U-U_m\right)^2\right\}_f \qquad (6)$$

is the mechanical power dissipated within the gas film; and

$$\dot{q}_{S\to f}=\bar{h}_{Sf}\left(T_{S_o}-T_f\right)\ ,\ \text{and}\ \ \dot{q}_{f\to F}=\bar{h}_{fF}\left(T_f-T_{F_i}\right) \qquad (7)$$

are the heat fluxes per unit area from shaft into the inner film and from inner film into the topfoil front surface, respectively. Above, T_{S_o} and T_{F_i} are the shaft (journal) outer surface temperature and the top foil temperature facing the gas film. Typically, a heat convection coefficient $\bar{h}$ is a function of the flow conditions (laminar or turbulent), gas thermal conductivity, and a characteristic diffusivity length, i.e. film thickness. Details on the evaluation of the heat convection coefficients appear later.

The **boundary conditions** for the inner film gas pressure and temperature fields $\{P_f, T_f\}$ are[4]:

(a) at the inlet plane $z=0$, $\{\Theta_l\le\Theta\le\Theta_t\}$

$$P_f\left(\Theta,0,t\right)=P_{C_o};\ T_f\left(\Theta,0,t\right)=T_{C_o} \qquad (8)$$

[4] Reynolds equation for the pressure field is of elliptic type, thus requiring of boundary conditions on the entire closure of the flow domain. On the other hand, the temperature transport equation is of parabolic type with specified boundary conditions at the inlet plane(s) where gas flow is supplied.
In addition note that due to the asymmetry in temperature conditions, an assumed pressure field symmetric about the bearing midplane, i.e. $P_f(z+\frac{1}{2}L)=P_f(z)$ when $0<z<\frac{1}{2}L$, is physically impossible. Prior analyses, see Ref. [1] for example, use this incorrect assumption.

where $\left(P_{C_o}, T_{C_o}\right)$ are the pressure and temperature of the *outer* cooling stream supplied at one end of the GFB.

(c) at the leading edge angle (Θ_l) of top foil, for $\{0 \le z \le L\}$,

$$P_f\left(\Theta_l, z, t\right) = P_O(\Theta_l,\ z);\quad T_f\left(\Theta_l, z, t\right) = T_{f_l}(\Theta_l) \tag{9}$$

with $T_{f_l} = f\left(T_O\left(\Theta_l\right), T_f\left(\Theta_t, z, t\right)\right)$, and $\{P_O, T_O\}$ as the gas pressure and temperature underneath the top foil (outer flow cooling stream).

(d) at the trailing edge angle (Θ_t) of top foil, for $\{0 \le z \le L\}$,

$$P_f\left(\Theta_t, z, t\right) = P_O(\Theta_t, z) \tag{10}$$

with the *exit* temperature leaving the topfoil, $T_{f_e} = T_f\left(\Theta_t, z, t\right)$, determined by solving Eq. (5).

Note that the inlet temperature T_{f_I} at the top foil leading edge (Θ_l) results from mixing of a fraction of the *hot* film stream leaving the top foil with temperature T_{f_E} with the externally supplied cold outer stream flow at temperature $T_{O(z)}$. A detailed formulation for the mixing condition will be given later.

(e) at the exit plane, $z=L$, $\{\Theta_l \le \Theta \le \Theta_t\}$

$$P_f\left(\Theta, L, t\right) = P_a \tag{11}$$

where P_a denotes ambient temperature. The exit film temperature $T_f\left(\Theta, L, t\right)$ is determined from solution of the thermal energy transport Eq. (5).

Pressure drop and thermal energy transport in outer gas flow region

The outer cooling gas stream with pressure and temperature $\left\{P_{C_o}, T_{C_o}\right\}$ at the inlet plane *z=0,* flows axially through the inner gas film and also through the region underneath the top foil and the inner diameter of the bearing housing. In this outer flow region, the gas pressure P_O drops from P_{C_o} towards the ambient condition P_a, while the gas temperature T_O increases as it removes heat from the topfoil surface at T_{F_o}.

The externally imposed gas flow is eminently axial, i.e. not disturbed by the closeness to the rotating shaft, which may induce fluid pre-rotation, or severely restricted by the underspring

bump layers. Under steady-state and fully-developed flow conditions, the axial outer mass flow rate $\left(\dot{m}_{z_O}\right)$ is constant, i.e.

$$\frac{d}{dz}\left(\dot{m}_{z_O}\right)=0 \leftarrow \dot{m}_{z_O}=\left(\rho\, h_B\, W\right)_O=-\frac{\Delta_B^3\,\rho_O}{\kappa_{z_O}\,\mu_O}\frac{dP_O^{\,2}}{dz} \tag{12}$$

where the thickness of the flow region equals the bump height Δ_B, and κ_{z_O} is a shear factor equal to 12 for laminar flow. For turbulent flow conditions, this factor depends on the axial flow Reynolds number and the bounding surfaces condition, see Ref. [7]. For laminar flow, Eq. (12) reduces to

$$\frac{d}{dz}\left(\frac{1}{T_O^2}\frac{dP_O^{\,2}}{dz}\right)=0 \tag{13}$$

The transport equation for the temperature of the outer cooling stream is [8]

$$c_{p_O}\frac{d\left(\dot{m}_{z_O}T_O\right)}{dz}+\dot{q}_{O\to B_i}-\dot{q}_{F\to O}=\left(W_O\,h_B\frac{dP_O}{dz}\right)+\Phi_O \tag{14}$$

Heat convected by gas flow + diffusion to/from bounding surfaces = compression work + dissipated energy

where

$$\Phi_O=\frac{\kappa_{z_O}\,\mu_O}{h_B}W_O^2 \tag{15}$$

is the mechanical power in the outer gas region; and

$$\dot{q}_{F\to O}=\bar{h}_{FO}\left(T_{F_o}-T_O\right),\ \text{and}\ \dot{q}_{O\to B_i}=\bar{h}_{OB}\left(T_O-T_{B_i}\right) \tag{16}$$

are the heat flow rates (per unit area) from topfoil back surface[5] into the outer gas stream, and from gas stream into the bearing surface, respectively. Above, T_{F_o} and T_{B_i} denote the temperature of the top foil back surface temperature and inner diameter of bearing cartridge. Above, the heat convection coefficients $\left(\bar{h}_{FO},\bar{h}_{OB}\right)$ depend on the cooling stream gas material properties and the flow conditions determining natural or forced convection processes.

Note that the viscous dissipation term Φ_O may be negligible since the bump height (Δ_B) is large, thus offering little resistance to the flow. The importance of the compression work term

[5] Note that a fraction of heat from the topfoil back surface flows *directly* by conduction through a bump foil into the bearing housing. The importance of this heat flux, relative to the heat removed by the outer cooling stream, is proportional to the conductivity of the bump material, and inversely proportional to the heat convection coefficients $\left(\bar{h}_{FO},\bar{h}_{OB}\right)$, i.e. the effectiveness of the forced heat convection process induced by the external cooling flow.

will be assessed later. However, compressibility effects need be retained since too large cooling mass flow rates may provoke choke conditions with a reduced efficiency in the heat removal capability of the external forced flow.

The **boundary conditions** for the outer cooling stream pressure and temperature fields $\{P_O, T_O\}$ are:

(a) at the inlet plane $z=0$, $$P_O(\Theta,0)=P_{C_o};\ T_O(\Theta,0)=T_{C_o} \tag{17}$$

Recall that (P_{C_o}, T_{C_o}) are the pressure and temperature of the *outer* cooling stream supplied at one end of the GFB.

(b) at the exit plane, $z=L$, $$P_O(\Theta,L)=P_a \tag{18}$$

if the gas flow is not choked. The exit outer stream temperature $T_O(\Theta,L)$ is determined from solution of the thermal transport Eq. (14).

Note that the thermal energy transport equation (14) apparently shows variation of temperature in the axial direction only. However, the foil surface temperature is a function of the circumferential coordinate (Θ). Hence, the angular coordinate is a parameter for the solution of the outer stream cooling temperature $T_O(\Theta,z)$.

Heat transport from top foil into outer cooling stream and conduction into bearing housing

The heat flow rate $\dot{q}_{f\to F}=\bar{h}_{fF}\left(T_f-T_{F_i}\right)$ convected from the thin film into the topfoil surface is further conducted through its thickness (Δ_{t_F}), and equals to

$$\dot{q}_{f\to F}=\frac{\kappa_F}{\Delta_{t_F}}\left(T_{F_i}-T_{F_o}\right)=\dot{q}_{F\to O}+\dot{q}_{F\to B_i} \tag{19}$$[6]

where $$\dot{q}_{F\to O}=\bar{h}_{FO}\left(T_{F_o}-T_O\right) \tag{20a}$$

is the heat convected into the outer cooling stream, and

$$\dot{q}_{F\to B_i}\approx\frac{\kappa_B}{h_B}\left(T_{F_o}-T_{B_i}\right) \tag{20b}$$

[6] This equation is strictly valid for $R_{B_i}\approx R_{F_i}\approx R_{F_o}$

is the heat conducted through the material of the bump layer into the bearing housing.

The total heat flux into the bearing housing adds the convection from the outer flow stream and the conduction through the bump material, i.e.

$$\dot{q}_{\to B_i} = \dot{q}_{O\to B_i} + \dot{q}_{F\to B_i} = \bar{h}_{OB}\left(T_O - T_{B_i}\right) + \frac{\kappa_B}{h_B}\left(T_{F_o} - T_{B_i}\right) \tag{21}$$

For simplicity, assume only radial heat conduction through the bearing shell with thickness $\Delta_{t_B} = \left(R_{B_o} - R_{B_i}\right)$. Hence, a simple analysis shows that the heat flow rate per unit length equals

$$\left(\dot{q}_{\to B_i}\right) R_{B_i} = \dot{Q}_{\to B} = \frac{\kappa_B}{\ln\left(R_{B_o} \big/ R_{B_i}\right)}\left(T_{B_i} - T_{B_o}\right) \tag{22a}$$

where, for a thin bearing shell,

$$\dot{Q}_{\to B} \sim \frac{\kappa_B R_B}{\Delta_{t_B}}\left(T_{B_i} - T_{B_o}\right) \tag{22b}$$

Finally, the heat flux $\dot{Q}_{\to B}$ is disposed by convection into an external fluidic media at temperature T_∞.

$$\dot{Q}_{\to B} = \bar{h}_{B\infty} R_{B_o}\left(T_{B_o} - T_\infty\right) \tag{23}$$

Above, $\bar{h}_{B\infty}$ is a heat convection coefficient, whose magnitude depends on the external fluid material properties and flow conditions determining either a natural or a forced convection process.

In spite of its apparent simplicity, the radial heat flow analysis will render foil ($\left(T_F\right)_{i,o}$ and bearing $\left(T_B\right)_{i,o}$ temperatures, as well as a cooling outer stream temperature (T_O) which vary in the circumferential and axial directions, i.e. $T_{B_i}\left(\Theta, z\right)$ for example.

Without an outer cooling flow stream, the heat transfer on the back of the topfoil is by natural convection and further conduction into the bearing through the bump strip layers. In this **simplistic** scenario, the heat flow model is much simpler and fully described by an overall or equivalent heat transfer coefficient $\bar{h}_{eq}$ that represents a multilayer conduction/convection.

Consider the heat flows through an arc of size $\Delta\Theta$, i.e. $\dot{Q} = R\,\dot{q}$. Figure A.4 depicts the various heat flow paths and a simple representation in terms of thermal resistances. The heat flow convected by the film into the top foil inner surface is conducted through the top foil and further conducted and advected into the bearing inner surface, i.e.

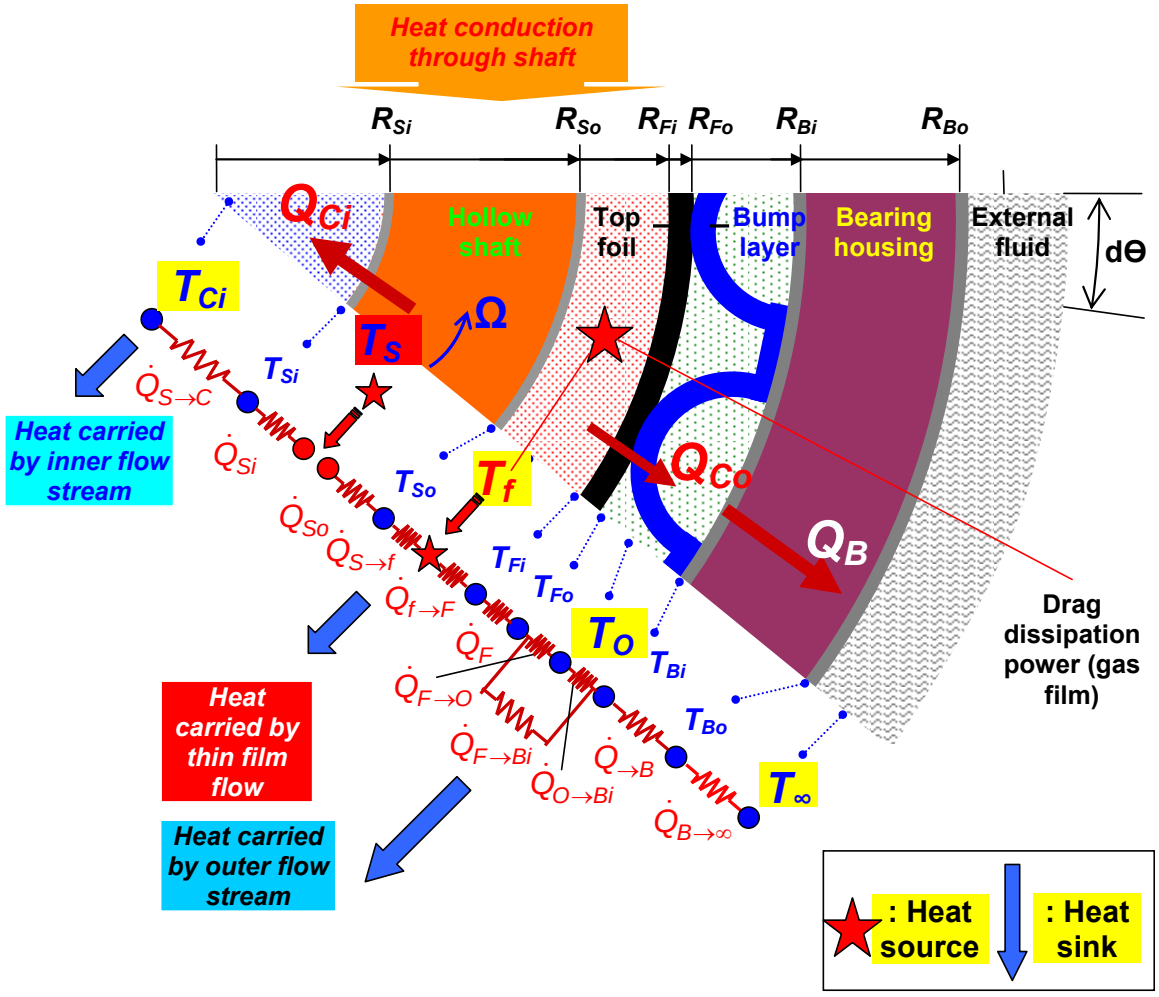

Fig. A.4. Simplified schematic diagram for heat flux paths in GFB system

$$\dot{Q}_{f\to F} = \bar{h}_{fF} R_{F_i} \left(T_f - T_{F_i}\right)$$

$$\rightarrow = \dot{Q}_{\to F} = \frac{\kappa_F\, R_F}{\Delta_{t_F}} \left(T_{F_i} - T_{F_o}\right) \tag{24a}$$

$$\rightarrow = \dot{Q}_{F\to B} = \bar{h}_{FO}\, R_{F_o} \left(T_{F_o} - T_O\right) + \frac{\kappa_F}{\Delta_B}\, R_{B_{eq}} \left(T_{F_o} - T_{B_i}\right)$$

where a bump *equivalent* radius $R_{B_{eq}} = \dfrac{\Delta_{t_B} N_B}{\pi}$ denotes the narrow contact area (/axial length) of N_B bumps with thickness Δ_{t_B} .

Since the outer stream is stagnant, then,

$$\dot{Q}_{F\to O} = \bar{h}_{FO}\, R_{F_o}\left(T_{F_o} - T_O\right) \to = \dot{Q}_{O\to B_i} = \bar{h}_{OB}\, R_{B_i}\left(T_O - T_{Bi}\right) .$$

In the absence of an outer cooling stream, the heat flow is conducted into the bearing to be finally disposed into an external fluidic medium at T_∞, i.e.

$$\dot{Q}_{F\to B} \to = \dot{Q}_{\to B} = \frac{\kappa_B}{\ln\left(R_{B_o} \big/ R_{B_i}\right)}\left(T_{B_i} - T_{B_o}\right) \tag{24b}$$

$$\to = \dot{Q}_{B\to\infty} = \bar{h}_{B\infty}\, R_{B_o}\left(T_{B_o} - T_\infty\right)$$

Eliminate the internal temperatures in the equations above by adding each heat flow divided by its respective thermal conductance (=1/resistance). This simple process leads to

$$\dot{Q}_{f\to F} = \dot{q}_{f\to F} R_{F_i} = \bar{h}_{eq_\infty}\, R_{F_i}\left(T_f - T_\infty\right) \tag{25a}$$

where the equivalent heat transfer coefficient is

$$\frac{1}{\bar{h}_{eq_\infty}} = \frac{1}{\bar{h}_{fF}} + \frac{1}{\dfrac{\kappa_F}{\Delta_{t_F}}} + \frac{R_{F_i}}{R_{B_{eq}}\dfrac{\kappa_F}{\Delta_B} + \dfrac{1}{\dfrac{1}{R_{F_o}\bar{h}_{FO}} + \dfrac{1}{R_{B_i}\bar{h}_{OB}}}} + \frac{R_{F_i}\ln\left(\dfrac{R_{Bo}}{R_{Bi}}\right)}{\kappa_B} + \frac{R_{F_i}}{h_{B\infty} R_{Bo}} \tag{25b}$$

Conversely, **an outer cooling stream with a large flow rate** takes away most of the heat from the back of the topfoil, with little conduction into the bearing. In this case, the heat flow reduces to the simple expression

$$\dot{Q}_{f\to F} = \dot{q}_{f\to F} R_{F_i} = \bar{h}_{eq_O}\, R_{F_i}\left(T_f - T_O\right) \tag{26a}$$

$$\frac{1}{\bar{h}_{eq_O}} = \frac{1}{\bar{h}_{fF}} + \frac{\Delta_{t_F}}{\kappa_F} + \frac{R_{F_i}}{R_{F_o}\bar{h}_{FO}} \tag{26b}$$

as also given by Peng and Khonsari [9].

Temperature field in rotating shaft

The inner cooling gas stream flowing through the hollow shaft is regarded as a sink of thermal energy. That is, this cooling mass flow rate is large enough to maintain a constant temperature T_{C_i} while advecting (removing) heat flow from the shaft inner surface [7] at temperature T_{S_i}. Note that the thin gas film with temperature T_f also carries away heat from the shaft outer surface at temperature T_{S_o}.

The energy transport equation for the rotating shaft in polar coordinates $(r,\Theta.z)$ is [10]

$$c_{P_S}\rho_S\,\Omega\frac{\partial T_S}{\partial\Theta}=-\left[\frac{1}{r}\frac{d}{dr}\left(r\,\dot{q}_{r_S}\right)+\frac{1}{r}\frac{d}{d\Theta}\left(\dot{q}_{\Theta_S}\right)+\frac{d}{dz}\left(\dot{q}_{z_S}\right)\right] \tag{27}$$

where the components of the heat flux vector are

$$\dot{q}_{\Theta_S}=-\kappa_S\frac{1}{r}\frac{\partial T_S}{\partial\Theta};\ \dot{q}_{r_S}=-\kappa_S\frac{\partial T_S}{\partial r};\ \dot{q}_{z_S}=-\kappa_S\frac{\partial T_S}{\partial z}; \tag{28}$$

The shaft temperature must be periodic in the circumferential direction. Hence, $T_S\left(\Theta,r,z\right)=T_S\left(\Theta+2\pi,r,z\right)$. Other **boundary conditions** include

a) Heat convection through inner and outer surfaces of hollow shaft, i.e.

$$\text{At}\quad r=R_{S_i}\qquad\left[-\dot{q}_{r_{S_i}}\,R_{S_i}\right]=\dot{Q}_{S\to C_i}=R_{S_i}\,\bar{h}_{SC_i}\left(T_{S_i}-T_{C_i}\right) \tag{29}$$

$$\text{And,}\ r=R_{S_o}\qquad\left[\dot{q}_{r_{S_o}}\,R_{S_o}\right]=\dot{Q}_{S\to f}=R_{S_o}\,\bar{h}_{Sf}\left(T_{S_o}-T_f\right); \tag{30}$$

Recall $\dot{Q}_{S\to f}=\dot{q}_{S\to f}\,R_{S_o}$. The equations above show the heat flows removed by the inner cooling stream and by the thin gas film, respectively.

b) Specification of shaft temperature at *z=0* **and** z=*L* for $\left\{0\le\Theta\le2\pi;R_{S_i}\le r\le R_{S_o}\right\}$. Accurate (a-priori) knowledge of the shaft temperature fields at the inlet and exit axial planes is quite difficult. In actuality, the model should not just consider a piece of hollow shaft of length *L* but rather a longer shaft span with physically known operating temperature conditions. Presently, assume for simplicity:

[7] Recall that for purposes of discussion, the shaft is regarded as *hot* with temperature $T_S > T_f > T_C$.

1. The inner cooling stream flow is so large that the shaft inner surface temperature T_{S_i} does not vary axially or circumferentially, i.e. it is a constant; and
2. A high speed (Ω) rotor condition tends to make more uniform the shaft temperature in the circumferential direction.

The considerations above imply that most of the heat flow within the shaft is transported radially. Hence, $\dot{q}_{\Theta_S} = \dot{q}_{z_S} = 0$; $\dot{q}_{r_S} = -\kappa_S \dfrac{d\,T_S}{d\,r}$; and the heat conduction Eq. (27) reduces to

$$\frac{1}{r}\frac{d}{d\,r}\left(r\,\dot{q}_{r_S}\right) = 0 \rightarrow \frac{1}{r}\frac{d}{d\,r}\left(r\frac{d\,T_S}{d\,r}\right) = 0 \tag{31}$$

Integration of this equation leads to a shaft temperature distribution along the radial coordinate equal to

$$T_S\left(r\right) = T_{S_i} + \left(T_{S_o} - T_{S_i}\right)\frac{\ln\left(r \big/ R_{S_i}\right)}{\ln\left(R_{S_o} \big/ R_{S_i}\right)} \tag{32}$$

And from the heat convection at the inner and outer surfaces of the hollow shaft,

$$-\dot{Q}_{S\rightarrow C_i} = -R_{S_i}\,\bar{h}_{SC_i}\left(T_{S_i} - T_{C_i}\right) = \dot{Q}_{S\rightarrow f} = R_{S_o}\,\bar{h}_{Sf}\left(T_{S_o} - T_f\right) \tag{33}$$

The equation above is incompatible with the assumption of pure radial heat flow and a *hot shaft* since it requires that if $\left(T_{S_i} - T_{C_i}\right) > 0 \rightarrow \left(T_f - T_{S_o}\right) > 0$, i.e. heat flows from the thin film into the shaft. More scrutiny of the heat conduction model is thus needed.

However, if the whole shaft is regarded at a uniform *hot* temperature, then $T_{S_i} = T_{S_o} = T_S$, and heat can flow into the thin film and/or into the cooling stream. Note that in this case, the shaft acts as a source of thermal energy with heat flowing along two opposite radial directions, i.e. through the inner and outer surfaces of the hollow shaft.

Summary of heat flow paths for GFB thermal model

Table A.1 summarizes each of the heat flows and their relevant physical description. See Figure A.4 for a definition of all temperatures, interfacial and within solids.

Table A.1 Summary of radial heat flows (convection and conduction)

Heat flow per unit axial length	Description
$\dot{Q}_{f\to F} = \dot{q}_{f\to F}\, R_{F_i} = \bar{h}_{fF}\, R_{F_i}\left(T_f - T_{F_i}\right)$	Heat convected from thin film into front (inner) surface of top foil
$\dot{Q}_{\to F} = \dfrac{\kappa_F\, R_F}{\Delta_{t_F}}\left(T_{F_i} - T_{F_o}\right)$	Heat conducted through top foil (inner to outer surfaces)
$\dot{Q}_{F\to B} = \dfrac{\kappa_F}{\Delta_B}\, R_{B_{eq}}\left(T_{F_o} - T_{B_i}\right)$	Heat conducted through bump foil – from top foil back surface into bearing inner surface
$\dot{Q}_{F\to O} = \bar{h}_{FO}\, R_{F_o}\left(T_{F_o} - T_O\right)$	Heat convected from back surface of top foil into cooling outer stream
$\dot{Q}_{O\to B_i} = \bar{h}_{OB}\, R_{B_i}\left(T_O - T_{B_i}\right)$	Heat convected from cooling outer stream into bearing inner surface
$\dot{Q}_{\to B} = \dfrac{\kappa_B}{\ln\left(R_{B_o} \big/ R_{B_i}\right)}\left(T_{B_i} - T_{B_o}\right)$	Heat conducted through bearing shell
$\dot{Q}_{B\to\infty} = \bar{h}_{B\infty}\, R_{B_o}\left(T_{B_o} - T_\infty\right)$	Heat convected from outer surface of bearing into external fluid medium
$\dot{Q}_{S\to f} = \dot{q}_{S\to f}\, R_{S_o} = \bar{h}_{Sf}\, R_{S_o}\left(T_{S_o} - T_f\right)$	Heat convected from shaft outer surface into gas film
$\dot{Q}_{\to S} = \dfrac{\kappa_S\left(T_{S_i} - T_{S_o}\right)}{\ln\left(\dfrac{R_{S_i}}{R_{S_o}}\right)}$	Heat conducted through hollow shaft
$-\dot{Q}_{S\to C_i} = \bar{h}_{SC_i}\, R_{S_i}\left(T_{S_i} - T_{C_i}\right)$	Heat from hollow shaft convected by cooling inner stream

About the heat transfer convection coefficients

The Reynolds-Colburn analogy between fluid friction and heat transfer [10] for fully-developed flow is used to determine the heat convection coefficients. The mean heat transfer over the entire laminar/turbulent boundary is:

$$S_t \wp_r^{2/3} = f/2 \tag{34}$$

where $S_t = \dfrac{\bar{h}_t}{\rho c_p V_t}$ is the *Stanton* number, and $\wp_r = \dfrac{c_p \mu}{\kappa}$ is the *Prandtl* number, and

$f = a_m \left[1 + \left(c_m \dfrac{r}{H} + \dfrac{b_m}{R_e} \right)^{e_m} \right]$ is the *Fanning* friction factor based on *Moody's equation*. Above V_t is a characteristic fluid velocity relative to the velocity of the surface of interest. From the relationships above, the heat convection coefficient is:

$$\bar{h}_t = \frac{1}{2} \frac{\rho c_p V_t f}{\wp_r^{2/3}} \tag{35}$$

and by analogy, $$\bar{h}_B = \frac{1}{2} \frac{\rho c_p V_B f_B}{\wp_r^{2/3}}; \quad \bar{h}_J = \frac{1}{2} \frac{\rho c_p V_J f_J}{\wp_r^{2/3}} \tag{36}$$

Where $V_{B,J}$ and $f_{B,J}$ are the fluid velocities and friction factors relative to the bearing and journal surfaces.

In a centered journal bearing with characteristic clearance c, the mean velocities $V_{B,J} \sim \frac{1}{2} \Omega R$. The friction factor for laminar flow is f=12/Re$_c$, where $\mathrm{Re}_c = \dfrac{\rho \Omega R c}{\mu}$ is the circumferential flow Reynolds number. Algebraic substitution of f into Eqs. (36) renders

$$\bar{h}_B = \bar{h}_J = 3 \frac{\kappa}{c} \wp_r^{1/3} \big|_{\text{laminar flow}} \text{ or } Nu = \frac{c \bar{h}}{\kappa} = 3 \wp_r^{1/3} \tag{37}$$

The archival literature presents many other formulas – empirically based - for turbulent flow heat transfer coefficients, including evolving or fully developed thermal conditions, as well as

for fixed wall temperature or constant heat flux into a wall. For example, a well known formula for turbulent flow conditions sets the Nusselt number as [10]

$$Nu = \frac{c_* \bar{h}}{\kappa} = 0.023\,\mathrm{Re}^{0.8}\,\wp_r^{1/3} \tag{38}$$

where $c_* = \Delta_B$ is a characteristic length for the outer cooling stream, and Re is an axial flow Reynolds number, a function of the axial pressure drop $\left(P_{C_i} - P_a\right)$.

NOMENCLATURE

c	Thin film radial clearance, a function of temperature [m]
c_p	Gas specific heat at constant pressure [I/kg-K]
D	2 R. Diameter [m]
e_X, e_Y	Journal eccentricity components [m], $e = \sqrt{e_X^2 + e_Y^2}$
f	Flow friction coefficient [-]
h_f	film thickness [m]
$\bar{h}$	Heat convection coefficient [W/m^2-K], $\hat{\bar{h}} = \bar{h} \Big/ \left(c \frac{\Omega}{2} \frac{P_a}{T_a} \right)$
$\bar{h}_{eq_O}$	Equivalent heat convection coefficient for outer radial heat flux [W/m^2-K]
L	Bearing axial width [m]
$\dot{m}_x, \dot{m}_z$	$\rho h\left(U, W\right)$. Mass flow rate per unit length [(kg/s)/m]
Nu	Nusselt number
P	Gas pressure [Pa]
$\dot{q}$	Heat flux per unit area [W/m^2]
$\dot{Q}$	= $\left(\dot{q}\, R\right)$ Heat flow rate per unit length [W/(m-rad)]
R	Radius [m]
$\Re_g$	Ideal gas constant [J/kg-K]
S_t	*Stanton* number
T	Bulk Temperature [K]

t	Time [s]
V_t	Characteristic fluid velocity [m/s]
U, W	Bulk-flow gas velocities in circumferential (x) and axial (z) direction
U_c	Mean circumferential flow velocity [m/s]
X, Y, Z	Inertial Cartesian coordinate system [m]
$x = R\,\Theta, z$	Coordinate system on plane of bearing [m]
α	Inlet flow pre-swirl factor
α_v	Gas viscosity parameter [N-s/m^2-K]
α_Ω	Inlet pre-swirl factor for circumferential velocity.
Δ_t	$\left(R_o - R_i\right)$, thickness [m]
Λ	$\frac{6\,\mu_a \Omega}{P_a}\left(\frac{R}{c}\right)^2$. Bearing speed number
Φ	Mechanical energy dissipation function [W/m^2]
κ	Thermal conductivity [W/m-K]
κ_z	Turbulent shear flow factor [-]
ρ	Gas density [kg/m^3]
μ	Gas viscosity [Pa-s]
$\wp_r$	*Prandtl* number
Θ	Circumferential coordinate [rad]
Ω	Rotor angular velocity [rad]

Subscripts

l,t	Leading and trailing edge of top foil
i, o	Inner and outer
O	Outer flow region
S	Shaft (journal)
B	Bearing
I, E	Inlet and Exit.
F	Foil
C	Cooling Stream
a	Ambient

REFERENCES

[1] Black, H. F., Allaire, P. E., and Barrett, L. E., 1981, "Inlet Flow Swirl in Short Turbulent Annular Seal Dynamics," *Proc. 9th Intl. Conf. in Fluid Sealing*, BHRA Fluid Engineering, Leeuwenborst, The Netherlands, pp. 141-152.

[2] Childs, D., 1993, *Turbomachinery Rotordynamics*, John Wiley & Sons, Inc., NY, Chapter 4, pp. 239-259.

[3] San Andrés, L., and Kim, T. H., 2007, "Improvements to the Analysis of Gas Foil Bearings: Integration of Top Foil 1D and 2D Structural Models," ASME Paper No. GT2007-27249.

[4] Kim, T. H., 2007, "Analysis of Side End Pressurized Bump Type Gas Foil Bearings: A Model Anchored to Test Data," Texas A&M University, Ph. D. Dissertation, College Station, TX.

[5] Bird, R. B., Stewart, W.E., Lightfoot, E.N., 1960, Transport Phenomena, John Wiley & Sons, Inc., New York, pp. 318-323.

[6] San Andrés, L., 2007, "Thermohydrodynamic Bulk-Flow Model in Thin Film Lubrication," Lecture Notes # 10 in Modern Lubrication Theory, available at http://phn.tamu.edu/me626

[7] San Andrés, L., 2007, "Derivation of Heat Flow Equations for Entire Gas Foil Bearing," Personal Research Note, November. (available upon request)

[8] Whitaker, S., 1977, *Fundamental Principles of Heat Transfer*, Pergamon Press, New York, pp. 208-219.

[9] Peng, Z-C., and Khonsari, M. M., 2006, "A Thermohydrodynamic Analysis of Foil Journal Bearings," ASME J. Tribol., **128**, pp. 534-540.

[10] Holman, J. P., 1990, *Heat Transfer*, McGraw Hill, New York, pp. 245-247.

APPENDIX B. NUMERICAL SOLUTION PROCEDURE FOR THERMOHYDRODYNAMIC ANALYSIS OF GFBS

The steady state, laminar flow Reynolds equation for an ideal gas of density $\rho_f = P_f \big/ \Re_g T_f$ flowing within a thin film thickness h_f is [1]

$$\frac{\partial}{\partial x}\left(\frac{h_f^3 P_f}{12\mu_f \Re_g T_f} \frac{\partial P_f}{\partial x} \right) + \frac{\partial}{\partial z}\left(\frac{h_f^3 P_f}{12\mu_f \Re_g T_f} \frac{\partial P_f}{\partial z} \right) = U_{m(z)} \frac{\partial}{\partial x}\left(\frac{P_f h_f}{\Re_g T_f} \right) \tag{1}$$

where

$$U_m(z) = \frac{\Omega R_{S_o}}{2}\left(1 - e^{-\delta z}\right) + \alpha_\Omega \Omega R_{S_o} e^{-\delta z} \quad \text{and} \quad \delta = \frac{12\mu_f}{(\dot{m}_z h^2)_f} \tag{2}$$

(x, z) are the circumferential and axial coordinates on the plane of the bearing. $\Re_g$ is the gas constant, and the gas viscosity $\mu = \mu(T)$ is a function of the gas absolute temperature . The mean circumferential flow velocity $U_m(z)$ is proportional to shaft surface speed and evolves in the axial direction due to the imposed pressure gradient from the outer cooling flow [2]. α_Ω is an empirical inlet flow pre-swirl factor.

For a perfectly aligned journal, the film thickness (h_f) in a GFB with a mechanical preload (r_p) at an offset angle (Θ_p) is [3];

$$h_f = c - r_p \cos\left(\Theta - \Theta_p\right) + e_X \cos(\Theta) + e_Y \sin(\Theta) + w_d \tag{3}$$

where, c, e_X, e_Y, and w_d are the bearing radial clearance, journal center displacements (e_X, e_Y) and top foil elastic deflection, respectively. See Fig.B.1 for the geometry of a journal and arcuate top foil with mechanical preload, and their disposition in the Cartesian coordinate system (X ,Y).

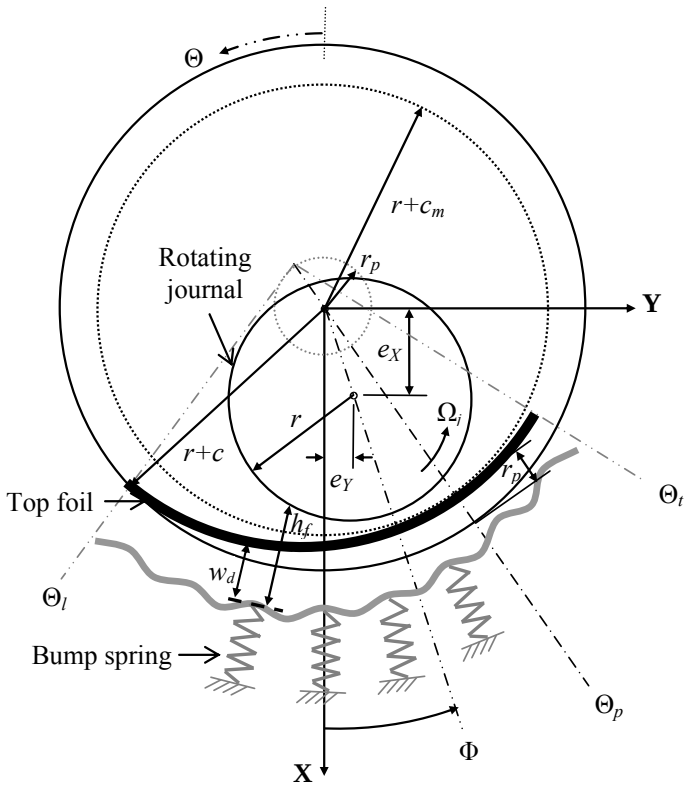

$r_p = c - c_m$
$r_p = 0$: Null preload
$r_p = c$: Journal – top foil contact

c: Radial (foil) clearance
c_m: Assembled radial clearance
h_f: Local film thickness considering, local aerofoil deflection, w_d

Fig. B.1. Geometry of a journal and arcuate top foil with mechanical preload

The numerical solution of Reynolds Eq. (1) implements a control volume – finite difference scheme with the exact advection model, Ref. [4], ensuring numerical accuracy and stability for operation at high journal rotational speeds, in particular. Figure.B.2 shows the configuration of a control volume. The balance of mass flow rates[1] through the control volume faces equal

$$\dot{M}_e - \dot{M}_w + \dot{M}_n - \dot{M}_s = 0 \tag{4}$$

where the indices *n, s, e, w* denote the north, south, east and west faces. The mass flow rates are

$$\dot{M}_e = -D_e\left(P_{f_E} - P_{f_P}\right) + U_{m(z)}\frac{h_{f_e}}{\Re_g T_{f_e}}\left(a_e P_{f_P} + b_e P_{f_E}\right)\Delta z \ ;$$

[1] Please note that Reynolds equation is just the mass continuity equation onto which the momentum transport equations for thin film flows are integrated into.

$$\dot{M}_w = -D_w\left(P_{f_P} - P_{f_W}\right) + U_{m(z)}\frac{h_{f_w}}{\Re_g T_{f_w}}\left(a_w P_{f_W} + b_w P_{f_P}\right)\Delta z\,; \tag{5}$$

$$\dot{M}_n = -D_n\left(P_{f_N} - P_{f_P}\right); \qquad \dot{M}_s = -D_s\left(P_{f_P} - P_{f_S}\right)$$

with the following definitions for the diffusion coefficients:

$$D_e = \frac{{h_{f_e}}^3 P_{f_e}}{12\mu_{f_e}\Re_g T_{f_e}} Cl_e\left(\frac{\Delta z}{\Delta x}\right);\; D_w = \frac{{h_{f_w}}^3 P_{f_w}}{12\mu_{f_w}\Re_g T_{f_w}} Cl_w\left(\frac{\Delta z}{\Delta x}\right); \tag{6}$$

$$D_n = \frac{{h_{f_n}}^3 P_{f_n}}{12\mu_{f_n}\Re_g T_{f_n}} Cl_n\left(\frac{\Delta x}{\Delta z}\right);\; D_s = \frac{{h_{f_s}}^3 P_{f_s}}{12\mu_{f_s}\Re_g T_{f_s}} Cl_s\left(\frac{\Delta x}{\Delta z}\right)$$

and

$$Cl_e = \frac{Cl'_e}{2} = \frac{\lambda_e}{2}\frac{\left(1+e^{\lambda_e}\right)}{\left(e^{\lambda_e}-1\right)};\; Cl_w = \frac{Cl'_w}{2} = \frac{\lambda_w}{2}\frac{\left(1+e^{\lambda_w}\right)}{\left(e^{\lambda_w}-1\right)};\; Cl_n = 1;\; Cl_s = 1; \tag{7}$$

with $$\lambda_w = \left(\frac{U_{m(z)}\Delta x}{{h_{f_w}}^2 P_{f_w}}\right);\; \lambda_e = \left(\frac{U_{m(z)}\Delta x}{{h_{f_e}}^2 P_{f_e}}\right) \tag{8}$$

as local *Peclet numbers* defining the flow condition through the faces of the control volume , i.e. the ratio of advection (shear) flow to pressure driven (Poiseuille) flow. The thin film gas pressures at the interfaces surrounding the control volume are interpolated as

$$\begin{aligned} P_{f_w} &= a_w P_{f_W} + b_w P_{f_P};\; P_{f_e} = a_e P_{f_P} + b_e P_{f_E} \\ P_{f_s} &= a_s P_{f_S} + b_s P_{f_P};\; P_{f_n} = a_n P_{f_P} + b_n P_{f_N} \end{aligned} \tag{9}$$

where $b's = 1 - a's$ and a is a function of the local *Peclet* number within the respective control volume.

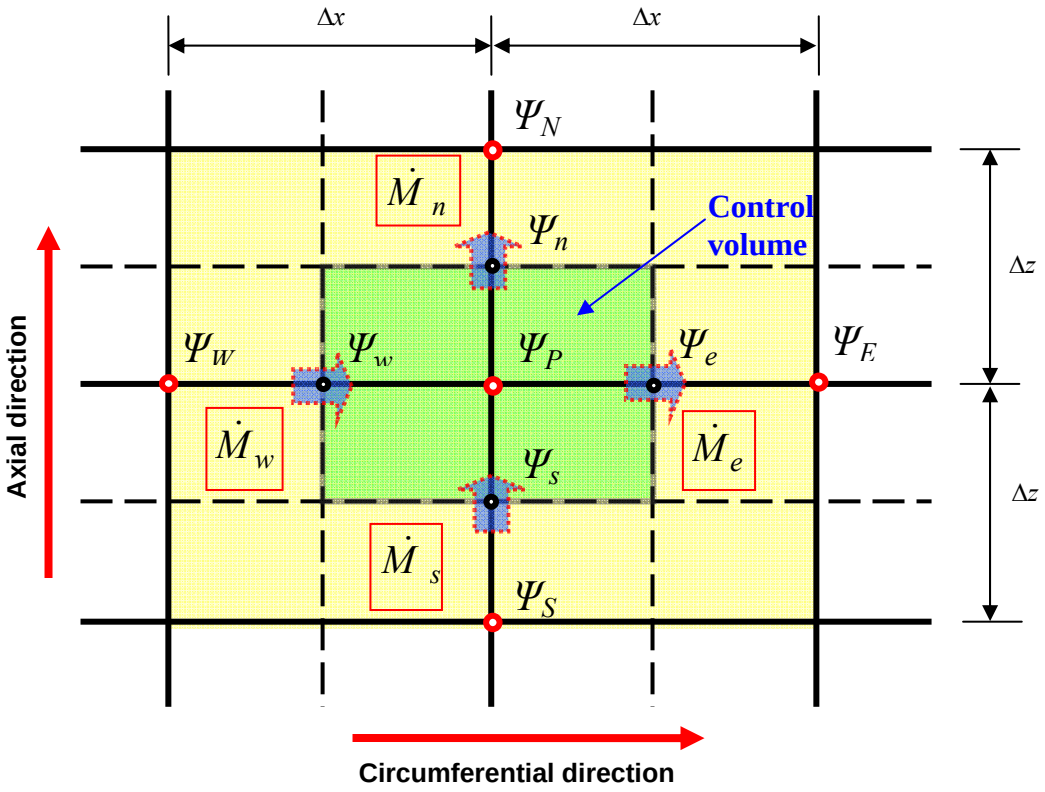

Fig. B.2. Configuration of control volume for integration of flow equations ($\Psi = P_f$ or T_f). Subscripts *E,W,N,S* for east, west, north, and south nodes; and subscripts *e,w,n,s* for east, west, north, and south faces of control volume.

Substituting Eqs. (6-9) into Eq. (4) and arranging leads to an algebraic equation for the nodal pressures:

$$A_w P_{f_W} + B_p P_{f_P} + C_e P_{f_E} - D_n P_{f_N} - D_s P_{f_S} = 0 \tag{10}$$

where

$$A_w = -D_w - U_{m(z)} \frac{h_{f_w} a_w}{T_{f_w}} \Delta z \;\; ; \quad C_e = -D_e - U_{m(z)} \frac{h_{f_e} b_e}{T_{f_e}} \Delta z \;\; ; \tag{11}$$

$$B_p = \left(D_e + D_w + D_n + D_s\right) + U_{m(z)} \left(\frac{h_{f_e} a_e}{T_{f_e}} - \frac{h_{f_w} b_w}{T_{f_w}} \right) \Delta z$$

Algebraic Eq. (10) for the control volume shown in Figure.B.2 is solved using the TDM algorithm [5], sweeping along the circumferential direction at a fixed axial (*z*) position. The process is iterative until the found pressure field does not vary within a certain tolerance and also

satisfying a minimum mass flow residual within each control volume. After completion of the iterative process, integration of the pressure field on the bearing surface renders the GFB reaction forces [6].

The bulk-flow thermal energy transport equation for steady-state conditions is [1]

$$c_{p_f}\left(\frac{\partial\left(\rho_f h_f U_f T_f\right)}{\partial x}+\frac{\partial\left(\rho_f h_f W_f T_f\right)}{\partial z}\right)+\bar{h}_{fF}\left(T_f-T_{F_i}\right)-\bar{h}_{Sf}\left(T_{S_o}-T_f\right)$$
$$=\left(U_f h_f\frac{\partial P_f}{\partial x}+W_f h_f\frac{\partial P_f}{\partial z}\right)+\frac{12\mu_f}{h_f}\left\{W_f{}^2+\frac{1}{3}U_m+\left(U_f-U_m\right)^2\right\} \tag{12}$$

where T_f, T_{S_o} and T_{F_i} are the thin film gas flow temperature, journal outer surface temperature, and the top foil inner surface temperature, respectively. (U_f, W_f) are the film flow velocity components along the circumferential and axial direction, respectively, and determined from the momentum transport equations. c_{p_f} denotes the gas specific heat, and gas density $\rho_f = P_f \big/ \Re_g T_f$.

Integration of Eq. (12) on the control volume in Figure B.2 leads to:

$$c_{p_f}\left[\begin{array}{l}\left(\rho_f h_f U_f T_f\right)^e \Delta z-\left(\rho_f h_f U_f T_f\right)^w \Delta z\\ +\left(\rho_f h_f U_f T_f\right)^n \Delta x-\left(\rho_f h_f U_f T_f\right)^s \Delta x\end{array}\right]+Q_S\Delta x\Delta z=\left(S_1+\Phi_f\right)\Delta x\Delta z \tag{13}$$

where $Q_S=\bar{h}_{fF}\left(T_f-T_{F_i}\right)-\bar{h}_{Sf}\left(T_{S_o}-T_f\right)$ is the heat flux from the thin film into the shaft and into the top foil front surface. $\Phi_f=\frac{12\mu_f}{h_f}\left\{W_f{}^2+\frac{1}{3}U_m^2+\left(U_f-U_m\right)^2\right\}$ is the mechanical power converted into heat, and $S_1=\left(U_f h_f\frac{\partial P_f}{\partial x}+W_f h_f\frac{\partial P_f}{\partial z}\right)$ is the (reversible) compression work.

Implementation of the upwind[2] scheme [5] for the thermal flux transport terms gives:

$$\left(\rho_f h_f U_f T_f\right)^e \Delta z=\dot{M}_e T_{f_e}=\left[\!\left[\dot{M}_e,0\right]\!\right]T_{f_P}-\left[\!\left[-\dot{M}_e,0\right]\!\right]T_{f_E}$$
$$\left(\rho_f h_f U_f T_f\right)^w \Delta z=\dot{M}_w T_{f_w}=\left[\!\left[\dot{M}_w,0\right]\!\right]T_{f_W}-\left[\!\left[-\dot{M}_w,0\right]\!\right]T_{f_P} \tag{14}$$

[2] A better numerical scheme, based on the exact advection model, will be implemented for next quarter. The current one follows prior work for bulk-flow models in high pressure annular seals.

$$\left(\rho_f\, h_f\, U_f T_f\right)^n \Delta x = \dot{M}_n T_{f_n} = \left[\!\left[\dot{M}_n, 0\right]\!\right] T_{f_P} - \left[\!\left[-\dot{M}_n, 0\right]\!\right] T_{f_N}$$

$$\left(\rho_f\, h_f\, U_f T_f\right)^s \Delta x = \dot{M}_s T_{f_s} = \left[\!\left[\dot{M}_s, 0\right]\!\right] T_{f_S} - \left[\!\left[-\dot{M}_s, 0\right]\!\right] T_{f_P}$$

where the mass flow rates are

$$\dot{M}_e = \left(\rho_f\, h_f\, U_f\right)^e \Delta z\,; \quad \dot{M}_w = \left(\rho_f\, h_f\, U_f\right)^w \Delta z\,; \tag{15}$$

$$\dot{M}_n = \left(\rho_f\, h_f\, W_f\right)^n \Delta x\,; \quad \dot{M}_s = \left(\rho_f\, h_f\, W_f\right)^s \Delta x$$

i.e., identical to those in Eq. (5). Above $\left[\!\left[A, B\right]\!\right]$ = max (*A,B*) . Substituting Eq. (14) into Eq. (12) and arranging leads to the algebraic equation for nodal temperatures:

$$A_{T_w} T_{f_W} + B_{T_p} T_{f_P} + C_{T_e} T_{f_E} + D_{T_N} T_{f_N} + D_{T_S} T_{f_S} = S_C^T \tag{16}$$

where

$$A_{T_w} = c_{p_f} \left[\!\left[\dot{M}_w, 0\right]\!\right]; \quad C_{T_e} = c_{p_f} \left[\!\left[-\dot{M}_e, 0\right]\!\right];$$

$$D_{T_N} = c_{p_f} \left[\!\left[-\dot{M}_n, 0\right]\!\right]; \; D_{T_S} = c_{p_f} \left[\!\left[\dot{M}_s, 0\right]\!\right]$$

$$-B_{T_p} = C_{T_e} + A_{T_w} + D_{T_n} + D_{T_s} + S_P^T\,; \tag{17}$$

and

$$S_P^T = \left(\bar{h}_{fF} + \bar{h}_{Sf}\right)\Delta x \Delta z\,; \quad S_C^T = -\left\{\left(\bar{h}_{fF} T_{F_i} + \bar{h}_{Sf} T_{S_o}\right) + S_1 + \Phi_f\right\}\Delta x \Delta z$$

The current analysis implements (laminar flow) heat convection coefficients ($\bar{h}_{fF}$, $\bar{h}_{Sf}$) that account for the development of a thermal boundary layer since, in actuality, temperature gradients do occur across the film thickness [1]. The thermal boundary layers reduce the heat convection to the rotating shaft or top foil when compared to the process in fully-developed flow, for example.

The mean *Nusselt* number over the flow domain with circumferential length ($l_x \sim 2\pi R_{Jo}$) is:

$$Nu_L = \frac{\bar{h}\, l_x}{\kappa} = 0.664\, \mathrm{Re}_L^{1/2}\, \wp_r^{1/3} \tag{18}$$

where $\mathrm{Re}_L = \frac{\rho_f l_x}{\mu_f}\frac{\Omega R}{2}$ is the shear flow Reynolds number, and $\wp_r = \frac{c_{p_f}\,\mu_f}{\kappa_f}$ is the *Prandtl* number representing the ratio of heat diffusion through momentum transport to heat conduction across the film thickness [7]. Note that the thermal conductivity (κ) in most gases is a function of temperature only.

The **boundary conditions** for the inner film gas pressure and temperature fields $\{P_f, T_f\}$ are[3]:

(a) at the inlet plane $z=0$, $\{\Theta_l \le \Theta \le \Theta_t\}$

$$P_f(\Theta,0,t) = P_{C_o};\ T_f(\Theta,0,t) = T_{C_o} \tag{19}$$

where (P_{C_o}, T_{C_o}) are the pressure and temperature of the *outer* cooling stream supplied at one end of the GFB.

(b) at the leading edge angle (Θ_l) of top foil, for $\{0 \le z \le L\}$,

$$P_f(\Theta_l,z,t) = P_O(\Theta_l,\ z);\quad T_f(\Theta_l,z,t) = T_{f_I}(\Theta_l) \tag{20}$$

with $T_{f_I} = f\left(T_O(\Theta_l), T_f(\Theta_t,z,t)\right)$, and $\{P_O, T_O\}$ as the gas pressure and temperature underneath the top foil (outer flow cooling stream).

(a) at the trailing edge angle (Θ_t) of top foil, for $\{0 \le z \le L\}$,

$$P_f(\Theta_t,z,t) = P_O(\Theta_t,z) \tag{21}$$

with the *exit* temperature leaving the top foil, $T_{f_e} = T_f(\Theta_t,z,t)$, determined by solving Eq. (16).

Note that the inlet temperature T_{f_I} at the top foil leading edge (Θ_l) results from mixing of a fraction of the *hot* film stream leaving the top foil with temperature T_{f_E} with the externally supplied cold outer stream flow at temperature $T_{O(z)}$.

(b) at the exit plane, $z=L$, $\{\Theta_l \le \Theta \le \Theta_t\}$

[3] Reynolds equation for the pressure field is of elliptic type, thus requiring of boundary conditions on the entire closure of the flow domain. On the other hand, the temperature transport equation is of parabolic type with specified boundary conditions at the inlet plane(s) where the gas flow is supplied. In addition note that due to the asymmetry in temperature conditions, a pressure field symmetric about the bearing middle plane, i.e. $Pf(z+ \frac{1}{2} L) = Pf(z)$, $0<z<\frac{1}{2} L$, is physically implausible. Ref. [10] takes the incorrect assumption.

$$P_f\left(\Theta, L, t\right) = P_a \tag{22}$$

where P_a denotes ambient temperature. The exit film temperature $T_f\left(\Theta, L, t\right)$ is determined from solution of the thermal energy transport Eq. (16).

(e) $P_f \geq P_a$ enforced. Note that top foil detachment doest not allow for gas pressures to fall below ambient pressure [2,3,6]. Hence, (fresh or cold) gas flowing from the axial sides of the bearing into the gas film is unlikely to occur.

In actuality, in a simple GFB a fresh stream of gas flow is naturally drawn into the thin film at the gap between the top foil leading and trailing edges. Hence, flow and thermal energy mixing processes occur at this location, as depicted in Figure B.3. Let $\left(\dot{m}_{Supply}, T_{Supply}\right)$ be the gas flow at supply conditions, while $\left(\dot{m}_{up}, T_{up}\right)$ is the flow leaving the trailing edge at a higher temperature. A fraction λ of the upstream flow mixes with the fresh or incoming gas stream. Simple mass conservation and energy balances determine the inlet mass flow $\dot{m}_{Inlet}$ at the leading edge of the top foil and with temperature T_{Inlet}, i.e.,

$$\dot{m}_{Inlet} = \lambda\, \dot{m}_{up} + \dot{m}_{Supply} \tag{23}$$

$$\dot{m}_{Inlet} T_{Inlet} = \lambda\, \dot{m}_{up} T_{up} + \dot{m}_{Supply} T_{Supply} \tag{24}$$

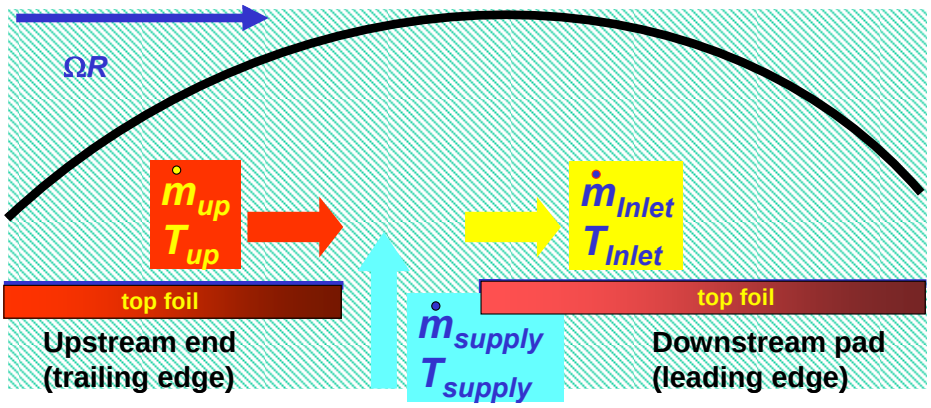

Fig. B.3. Schematic view of thermal mixing conditions at gap in between trailing and leading edge of top foil.

Recall that λ denotes the fraction of upstream gas flow leaving at the trailing edge of the top foil and re-entering the thin film of the GFB at the leading edge of the top foil. The thermal

mixing parameter λ (<1) depends on the bearing configuration and on the strength of an externally imposed cooling flow. **That is, λ is an empirical parameter**. Low values of λ ensure cool operating conditions, i.e. $T_{Inlet} \sim T_{Supply}$. On the other hand, $\lambda \sim 1$ makes for a poor bearing design with no replenishment of fresh gas and too large temperature rises. From the equations above,

$$T_{Inlet} = \frac{\lambda \dot{m}_{up} T_{up} + \dot{m}_{Supply} T_{Supply}}{\lambda \dot{m}_{up} + \dot{m}_{Supply}} \tag{25}$$

Other considerations

Without an outer cooling flow stream, the heat transfer on the back of the top foil is by natural convection and further conduction into the bearing through the bump strip layers. In this **simplistic** scenario, the heat flow model is fully described by an overall or equivalent heat transfer coefficient $\bar{h}_{eq_{Bo}}$ that represents a multilayer conduction/convection. The heat flow convected by the film into the top foil inner surface is conducted through the top foil and further conducted and advected into the bearing outer surface through the bump strip layers, i.e.

$$\frac{1}{\bar{h}_{fB}} = \frac{1}{\bar{h}_{eq_{Bo}}} = \frac{1}{\bar{h}_{fF}} + \frac{1}{\frac{\kappa_F}{\Delta_{t_F}}} + \frac{R_{F_i}}{R_{B_{eq}} \frac{\kappa_F}{\Delta_B} + \frac{1}{\frac{1}{R_{F_o} \bar{h}_{FO}} + \frac{1}{R_{B_i} \bar{h}_{OB}}}} + \frac{R_{F_i} \ln\left(\frac{R_{Bo}}{R_{Bi}}\right)}{\kappa_B} \tag{26}$$

where the convection coefficient ($\bar{h}_{fF}$) is a convection coefficient accounting for heat fluxes from the gas film into the top foil inner surface. κ_F and κ_B are thermal conductivities for foil and bearing housing, respectively. R's are top foil ($R_{Fi,o}$) and bearing ($R_{Bi,o}$) radii - inner and outer. $\bar{h}_{FO}$ and $\bar{h}_{OB}$ are natural heat convection coefficients accounting for heat fluxes from the top foil outer surface to the outer gap and from the outer gap to the bearing housing inner surface, respectively. A bump *equivalent* radius $R_{B_{eq}} = \frac{\Delta_{t_B} N_B}{\pi}$ denotes the narrow contact area (/axial length) of N_B bumps with thickness Δ_{t_B} and height Δ_B.

Conversely, an outer cooling stream with a large flow rate takes away most of the heat from the back of the top foil, with little conduction into the bearing. In this case, the heat flow reduces to the simple expression

$$\frac{1}{\bar{h}_{eq_O}} = \frac{1}{\bar{h}_{fF}} + \frac{\Delta_{t_F}}{\kappa_F} + \frac{R_{F_i}}{R_{F_o}\bar{h}_{FO}} \tag{27}$$

as also given by Peng and Khonsari [10].

When the inner cooling gas stream flowing through the hollow shaft is regarded as a sink of thermal energy, an overall or equivalent heat transfer coefficient $\bar{h}_{eq_c}$ that represents a multilayer heat conduction/convection from the gas film into the shaft outer surface and then to the inner cooling flow though the shaft wall, i.e.

$$\frac{1}{\bar{h}_{eq_c}} = \frac{1}{\bar{h}_{Sf}} + \frac{R_{So}\ln\left(\frac{R_{Si}}{R_{So}}\right)}{\kappa_S} + \frac{R_{So}}{\bar{h}_{Sc}R_{Si}} \tag{28}$$

Figure A.4 (Appendix A) shows the various heat flow paths (Q's) and a simple representation in terms of thermal resistances. **Appendix A** details each of the heat flow and their relevant physical description.

NUMERICAL SOLUTION PROCEDURE

The current thermohydrodynamic analysis extends the capabilities of the computational software *2DXLGFBpress*® [2] to predict the gas film temperature from solution of the thermal energy transport equation. The gas viscosity is proportional to the temperature, and hence, it affects the generation of hydrodynamic pressure within the gas film.

In brief, the original *2DXLGFBpress*® predicts the performance of generation I and II GFBs with side gas pressurization. Predictions from the numerical model have been validated against published test data, see Ref. [2] for example. The program integrates a limiting GFB 1D-pressure field [9] as a starting (guess) field prior to performing the numerical analysis towards solution of the two dimensional nonlinear Reynolds equation, The structural properties of the top foil and underlying bump strip layers are collected in a global stiffness matrix which is decomposed into upper and lower triangular parts prior to computations with the gas film model, see Ref. [3].

Figure B.4 presents a flow chart for operation of the computational program for GFB thermohydrodynamic analysis, from hereon referred as **2DGFB_HT®**. For given input operating conditions, the limiting speed 1D-pressure field and journal eccentricity serve to initiate the numerical solution of the steady state film flow equations (pressure and temperature). The solution procedure solves simultaneously the Reynolds equation (mass flow continuity) and thermal transport equations along a fixed axial coordinate. The forward marching procedure solves at a fixed axial location, Eq. (10) for film pressure, and next Eq. (16) for film temperature, over the set of control volumes extending along the bearing circumference. Gas film properties, density and viscosity are updated, prior to marching *downstream* to the next set of control volumes. The procedure is iterative satisfying stringent constraints on the maximum differences in pressure and temperature fields.

Note that the temperature field affects the operating bearing clearance due to shaft thermal growth, and also the foil support structural stiffness due to changes in the mechanical properties of the bearing cartridge, shaft and foil components. These important changes are taken into account rigorously as the iterative solution progresses towards its final converged state.

In the process, an outer iteration loop with a Newton-Raphson scheme updates the equilibrium journal position that generates the hydrodynamic gas pressure creating a reaction force balancing the specified static load. Lastly, dynamic force coefficients, stiffness and damping, are obtained from first-order pressure fields obtained from solving linear perturbed Reynolds equation (to be detailed in later progress reports).

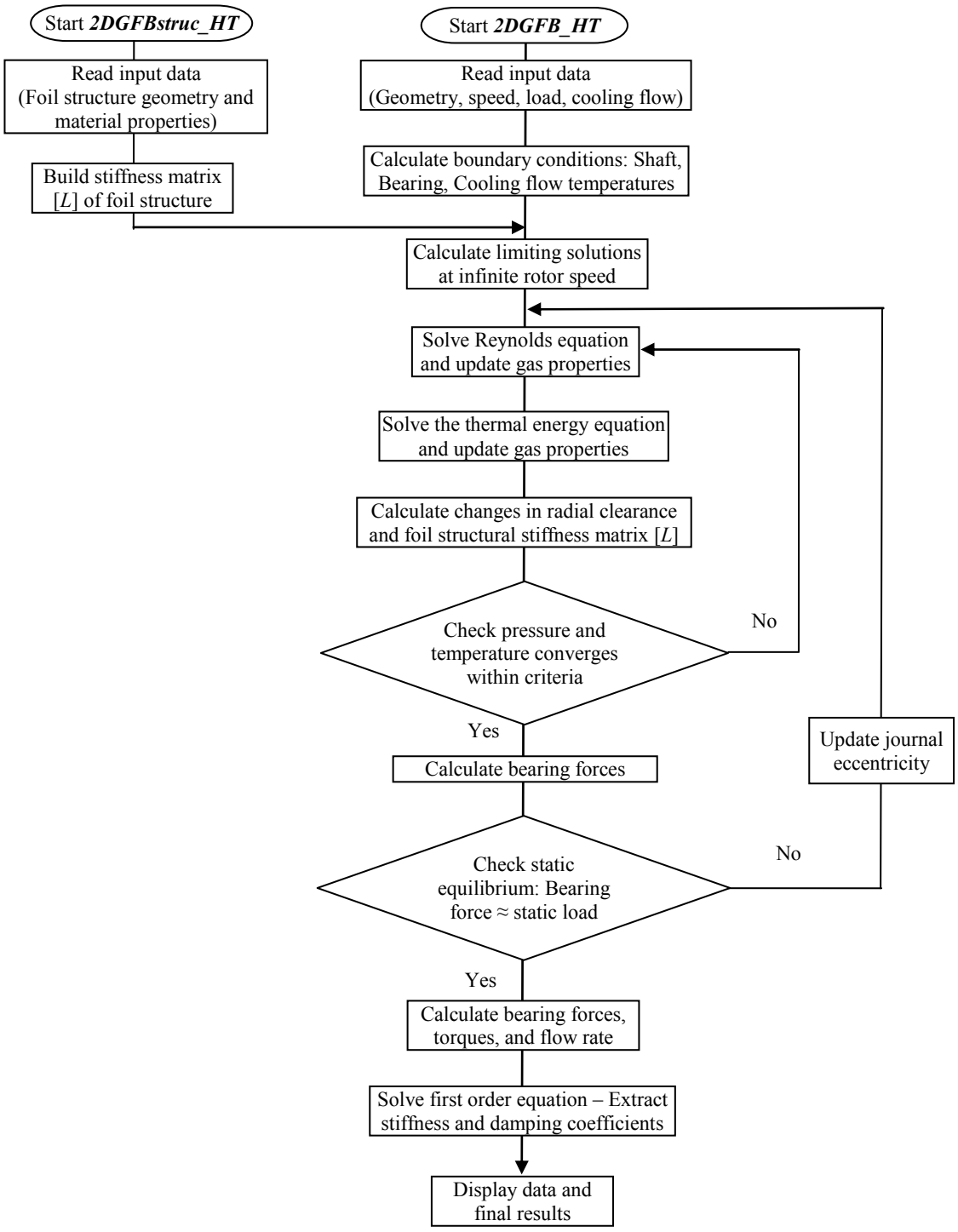

Fig. B.4. Flow chart illustrating the operation of THD GFB computational program 2DGFB_HT®

NOMENCLATURE

c	Thin film radial clearance, a function of temperature [m]
c_p	Gas specific heat at constant pressure [I/kg-K]
D	Diameter [m], D=2 R
e_X, e_Y	Journal eccentricity components [m], $e = \sqrt{e_X^2 + e_Y^2}$
h	film thickness [m]
$\bar{h}$	Heat convection coefficient [W/m^2-K]
L	Bearing axial width [m]
l_x	Pad circumferential length, $R(\Theta_t - \Theta_l)$ [m]
Nu	*Nusselt* number
P	Gas pressure [Pa]
R	Radius [m]
$\Re_g$	Ideal gas constant [J/kg-K]
r_p	Preload [m]
S_C, S_T	Centrifugal growth and thermal expansion [m]
T	Bulk Temperature [°C]
t	Time [s]
U,W	Bulk-flow gas velocities in circumferential (x) and axial (z) direction
U_m	Mean circumferential flow velocity [m/s]
w_d	top foil transverse deflection [m]
X,Y,Z	Inertial Cartesian coordinate system [m]
$x = R\,\Theta, z$	Coordinate system on plane of bearing [m]
α_T	Thermal expansion coefficient [-]
α_Ω	Inlet pre-swirl factor for circumferential velocity [-]
κ	Thermal conductivity [W/m-K]
ρ	Gas density [kg/m^3]
λ	Thermal inlet mixing ratio [-]
μ	Gas viscosity [Pa-s]
ν	Poisson's ratio [-]

$\wp_r$	*Prandtl* number, $\wp_r = \dfrac{c_p\,\mu}{\kappa}$
Θ	Circumferential coordinate [rad]
Ω, ω	Rotor angular velocity and whirl frequency [rad]

Subscripts

l,t,p	Leading and trailing edge of top foil, and offset position
f	Thin gas film
i, o	Inner and outer
O	Outer flow region
S	Shaft (journal)
B	Bearing
F	Foil
a	Ambient

REFERENCES

[1] San Andrés, L., 2007, "Thermohydrodynamic Bulk-Flow Model in Thin Film Lubrication," Lecture Notes # 10 in Modern Lubrication Theory, available at http://phn.tamu.edu/me626.

[2] Kim, T. H., 2007, "Analysis of Side End Pressurized Bump Type Gas Foil Bearings: A Model Anchored to Test Data," Texas A&M University, Ph. D. Dissertation, College Station, TX.

[3] San Andrés, L., and Kim, T. H., 2007, "Improvements to the Analysis of Gas Foil Bearings: Integration of Top Foil 1D and 2D Structural Models," ASME Paper No. GT2007-27249.

[4] Faria, M., and San Andrés, L., 2000, "On the Numerical Modeling of High speed Hydrodynamic Gas Bearing," ASME Journal of Tribology, **122**, pp 124-130.

[5] Patankar, S. V., 1980, *Numerical Heat Transfer and Fluid Flow*, Hemisphere Publishing Corporation, McGraw Hill.

[6] Kim, T. H., and San Andrés, L., 2008, "Heavily Loaded Gas Foil Bearings: a Model Anchored to Test Data," ASME J Gas Turbines Power, **130**, 012504.

[7] Holman, J. P., 1990, *Heat Transfer*, McGraw Hill, New York, pp. 235-241.

[8] Peng, Z-C., and Khonsari, M. M., 2006, "A Thermohydrodynamic Analysis of Foil Journal Bearings," ASME J. Tribol., **128**, pp. 534-540.

[9] Kim, T.H., and L. San Andrés, 2006, "Limits for High Speed Operation of Gas Foil Bearings," ASME J. Tribol., **128**, pp. 670-673.

APPENDIX C. GFB THERMAL MODEL PREDICTIONS COMPARED TO PUBLISHED TEST DATA

Predictions versus Test Data in Radil and Seszotek [1]

Radil and Zeszotek [1] present measurements of temperature in a III generation FB for a number of operating conditions, including changes in load and rotational speed, and with the environment (room) temperature at 21 °C. The test GFB has an axial length L=41 mm and a diameter D=50 mm. Note, however that Ref. [1] does not detail[1] the foil material nor the bump strips geometry and disposition. For an applied static load increasing from 9 N to 222, and after reaching steady state (15 minutes or more), thermocouples tack welded beneath certain bumps record metal temperatures. The measurements evidence a quick increase in temperature as soon as the rotor spins due to a large bearing preload (tight clearance). Note that the bearing dead weight is just 9N. The measured temperature increases as the rotor speed increases and as the static load increases. Peak temperature is measured along the bearing mid-plane at the heavily loaded zone (loading direction) and not at the bearing side edges where the film thickness is minimal. Measurements also show significant axial thermal gradients which increases in rotor speed, in direct opposition to predictions in Ref. [2].

The present study retakes foil material properties and bump dimensions similar to those of a generation I GFB [3], with some published data taken from Refs. [1, 4], in order to predict the bearing temperatures measured in Ref. [1]. Table 1 displays the bearing geometry and operating conditions for the GFB analyzed. The table notes various assumed values and considerations.

[1] This deficiency is not unusual since foil bearing technology is guarded closely by its manufacturers. Most unusual is the ability of prior analyses to predict closely the measurements without exact knowledge of the bearing geometry and operating conditions. See Refs. [2,5,6] for example.

Table C.1. Geometry and operating conditions of simple GFB

Parameters[2]	Value / comment	
Bearing cartridge		
Bearing inner radius, $R_{Bi}=D/2$	25 mm	Ref. [1]
Bearing length, L	41 mm	Ref. [1]
Bearing cartridge thickness, t_B	5 mm	Assumed
Nominal radial clearance, c	20 μm	Assumed
Top foil and bump strip layer		
Top foil thickness, Δ_{t_F}	127 μm	Ref. [4]
Bump foil thickness, Δ_{t_B}	127 μm	Ref. [4]
Bump half length, l_B	1.778 mm	Assumed
Bump pitch, s_0	4.064 mm	Assumed
Bump height, Δ_B	0.580 mm	Assumed
Number of bumps, N_b x strips, N_s	39 x 1	Assumed
Bump foil Young's modulus, E	200 GPa	
Bump foil Poisson's ratio, v	0.31	
Bump foil stiffness, k_B*	10.4 GN/m^3	
Gas properties at 21 °C		
Gas Constant, $\Re_g$	287 J/(kg-°K)	
Viscosity, μ	1.73×10^{-5} Pa-s	
Conductivity, κ	0.0257 W/m°K	
Density, ρ	1.164 kg/m^3	
Specific heat, c_p	1,020 J/kg°K	
Ambient pressure, P_a	1.014 x 10^5 Pa	

* Calculated using Iordanoff's formulas in Ref. [7]

The gas properties in Table C.1 are nominal at ambient temperature (~21 °C). In the analysis, gas viscosity (μ) and conductivity (κ) change with gas temperature, i.e., $\mu = 4\times10^{-8}\ T_{\circ K} + 6.57\times10^{-6}$ and $\kappa = 7.0\times10^{-5}\ T_{\circ K} + 4.2\times10^{-3}$ [8]. The gas specific heat c_p = 1,020

[2] Refs. [9,10] show material properties for the Inconel 718 bearing cartridge, Inconel X750 top foil and bump strip layer, and air at 21 °C, respectively.

J/kg°K does not change significantly with temperature. For example, c_p varies from 1,005 J/kg °K at -150 °C to 1,067 J/kg°K at 400 °C [8].

During analysis, centrifugal growth (S_C) of the rotating shaft reduces the actual bearing clearance as the rotor speed (Ω) increases. The shaft growth depends on the shaft geometry and material properties [11]:

$$S_C = \frac{R_{So}\rho_s\Omega^2}{8E_S}\left\{(1-\nu_s)A_1 + (1-\nu_s)A_2 - \left(1-\nu_s^2\right)R_{So}^2\right\} \qquad (1)$$

$$A_1 = \left(R_{So}^2 + R_{Si}^2\right)(3+\nu_s) \qquad A_2 = R_{Si}^2(3+\nu_s)$$

where E_s, ν_s, and ρ_s are the shaft elastic modulus, Poisson ratio, and density, respectively. The shaft has an outer radius R_{So}; and if hollow, an inner radius R_{Si}. Note that the shaft growth $S_C \sim \Omega^2$. The growth is much larger for a hollow shaft with a large inner diameter, i.e. a thin wall. Figure C.1 shows the predicted centrifugal growth versus rotor speed for Inconel 718 shaftx (solid and hollow). The graph evidences the rapid growth of the rotor OD for a hollow thin walled shaft. Hence, journal design must consider this effect to prevent failure due to shaft (thermal) seizure, as pointed out in Ref. [4].

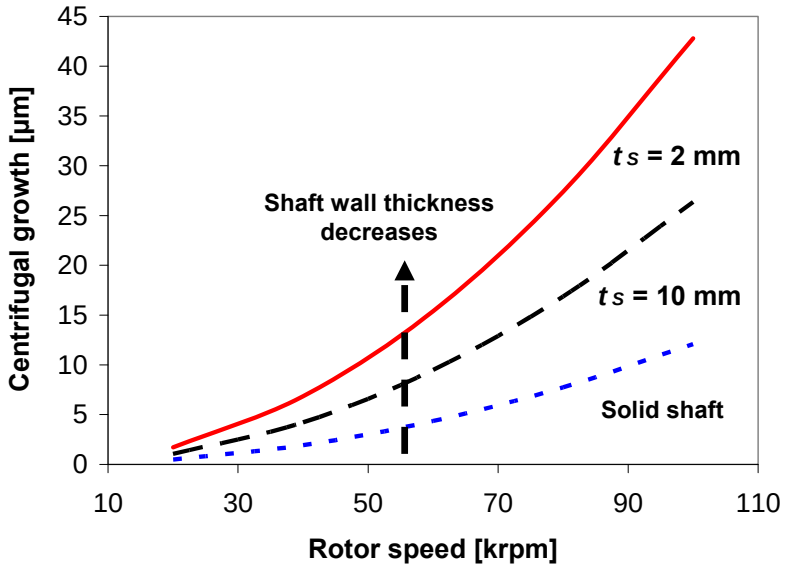

Fig. C.1. Shaft centrifugal growth versus rotor speed. Solid shaft and two hollow shafts (two wall thicknesses). Material Inconel 718. Shaft outer diameter of 50 mm, wall thickness $t_s = R_{So} - R_{Si}$

The shaft (or bearing) thermal expansion (S_T) is proportional to the temperature difference (ΔT) through the material thermal expansion coefficient (α_T) [11], i.e.

$$S_T = \alpha_T (R_{So} - R_{Si}) \Delta T \tag{2}$$

Although test shaft geometry and operating conditions in Ref. [1] are not fully known, predictions are still obtained assuming:

- solid (Inconel 718) shaft (R_{So} =25 mm, R_{Si} =0 mm)
- Ambient air surrounding shaft and bearing at (T_{supply}) = 21 °C (294.3 K)
- Isothermal shaft (T_S) at 21 °C
- Constant temperature of outer diameter bearing cartridge at T_{Bo}=21 °C.
- Thermal mixing parameter of λ=0.65. No cooling flow is forced underneath the top foil. Hence, the thermal gradient is from the hot gas film into the shaft and into the bearing cartridge.
- Heat transfer coefficients from the film into the top foil and from film into the shaft are $\bar{h}_{fF} = \bar{h}_{Sf}$ = 20 W/m^2°K, respectively. These coefficients are representative for thin film gas flows.

For increasing rotor speeds, 20-50 krpm, Figure C.2 shows the predicted peak film temperature at the bearing mid-plane (circumferential angle ~190°) and test data from Ref. [1] versus static load. Symbols denote the test data[3] while continuous lines represent the THD model predictions. The maximum load W=222 N represents a specific pressure of 1.08 bar (15.9 psi). As expected, the peak film temperature grows as the static load increases and as the rotor speed increases. Note that both predicted and experimentally obtained peak temperatures are higher than ambient temperature, i.e., $T_f >>$ 21 °C, even for operation with a small load of just 9 N. This large temperature rise within the film is an indicative of poor

[3] The test values do not strictly represent film temperatures. In the experiments, the temperatures shown in Figure C.2-C.4 are recorded at the outer surface of the bump strip layer around the junction with the top foil [1].

supply conditions ($\lambda=0.65$), typical in generation I GFBs and showing the absence of a forced pressure fed gas flow on one side of the bearing. As the static load increases to 222 N, the film peak temperature increases mildly. Note that the predicted centrifugal growth is insignificant, i.e., max. 3 μm at 50 krpm for a solid shaft.

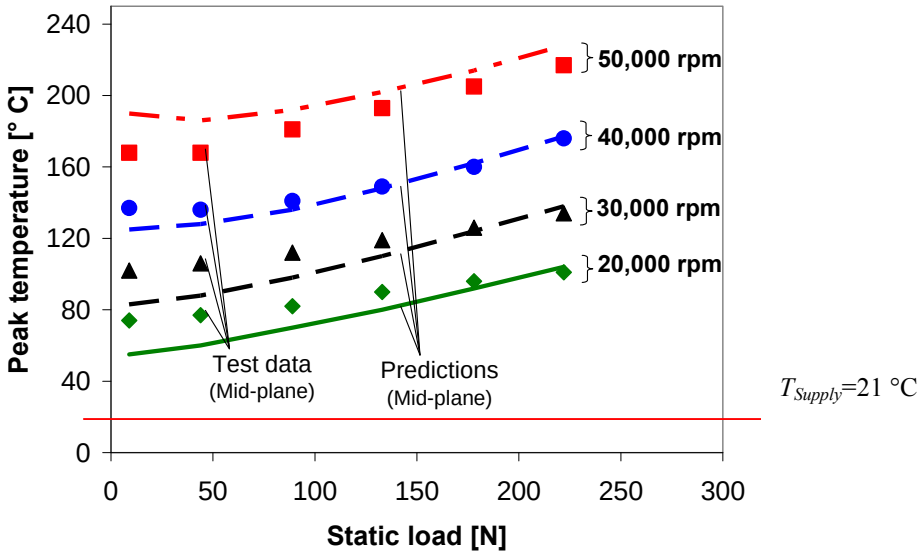

Fig. C.2. Predicted peak film temperature versus static load for increasing rotor speeds. Supply air (T_{Supply}), shaft (T_S), and bearing OD (T_B) temperatures at 21 °C. Comparison to test data [1]

Figure C.3 depicts the predicted gas film peak temperatures at the GFB mid-plane and near side edge versus static load for two rotor speeds, 20 krpm and 40 krpm. The peak temperature increases as the rotor speed increases and as the static load increases. In general, the difference in film temperatures at the mid-plane and edge (axial thermal gradient) increases as the rotor speed increases. Both measurements and predictions show the film temperature is largest at the bearing mid-plane, hence denoting the absence of an axial flow cooling path. The predicted temperatures correlate favorably with the test data. Most importantly note that the peak film temperature nearly doubles as the journal speed also doubles, irrespective of the applied load.

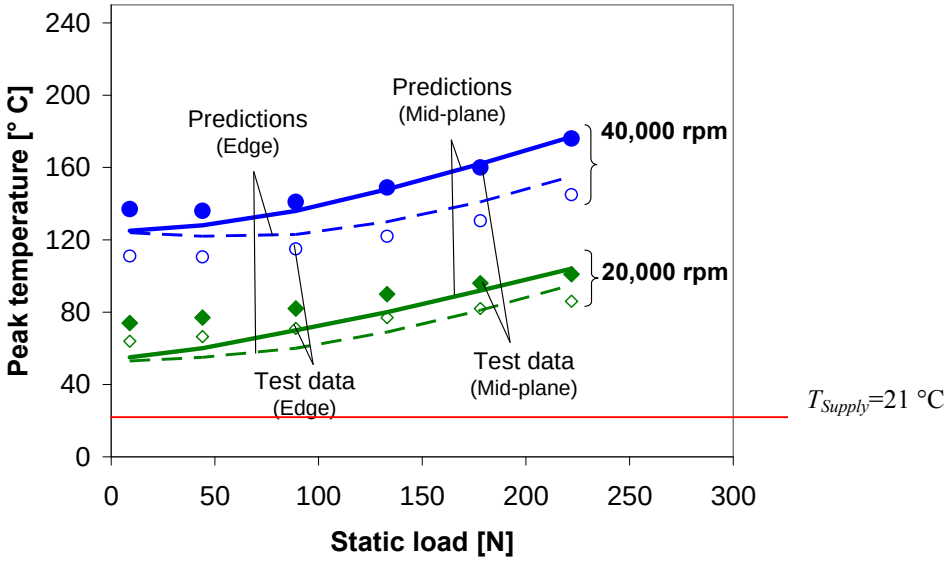

Fig. C.3. Predicted bearing mid-plane and edge film temperatures versus static load at circumferential location of 180 ° for two rotor speeds, 20 krpm and 40 krpm. Supply air (T_{Supply}), shaft (T_S), and bearing OD (T_B) temperatures at 21 °C. Comparison to test data [1]

At a static load of 133 N, (W/LD=0.65 bar), Figure C.4 shows the predicted gas film peak temperature distribution along the bearing axial plane ($0<z<L$) for increasing rotor speeds. The film temperature achieves its maximum value at the bearing mid-plane, and drops slightly at the side edges (circumferential angle ~190°). The predictions, in the absence of a forced axial cooling flow path, show a temperature profile that is symmetric about the bearing mid-plane, i.e. $T_f(z)=T_f(L-z)$ for $0<z<\frac{1}{2}L$. On the other hand, the test data shows a degree of asymmetry [1]. The predictions are in good agreement with the test temperatures, in particular at the speed of 40 krpm.

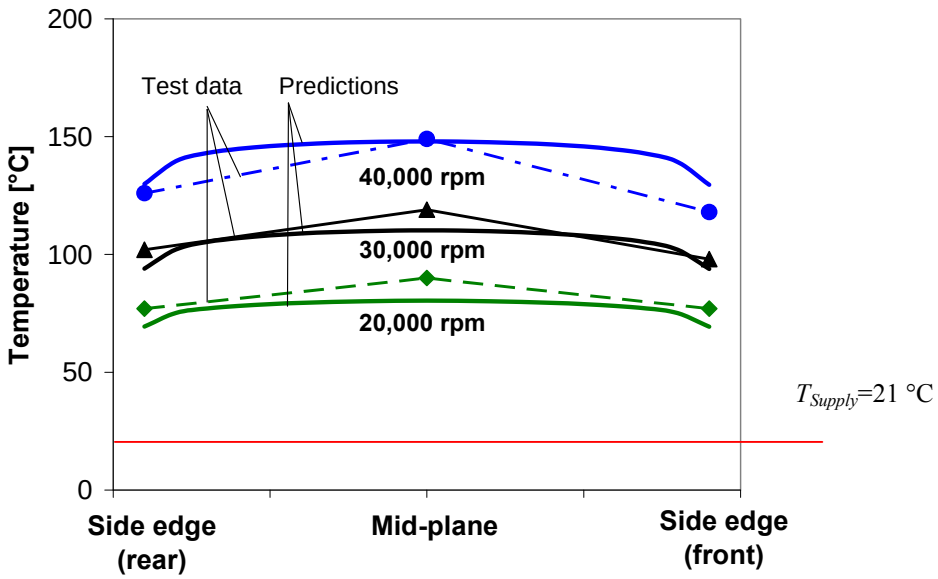

Fig. C.4. Predicted axial film temperature profile for three rotor speeds and a static load of 133 N. Supply air (T_{Supply}), shaft (T_S), and bearing housing (T_B) temperatures at 21 °C. Comparison to test data [1]

REFERENCES

[1] Radil, K. C. and Zeszotek, M., 2004, "An Experimental Investigation into the Temperature Profile of a Compliant Foil Air Bearing," STLE Tribol. Trans., **47**(4), pp 470-479.

[2] Peng, Z-C., and Khonsari, M. M., 2006, "A Thermohydrodynamic Analysis of Foil Journal Bearings," ASME J. Tribol., **128**, pp. 534-540.

[3] Ruscitto, D., Mc Cormick, J., and Gray, S., 1978, "Hydrodynamic Air Lubricated Compliant Surface Bearing for an Automotive Gas Turbine Engine I-Journal Bearing Performance," NASA CR-135368.

[4] Dykas, B., and Howard, S. A., 2004, "Journal Design Consideration for Turbomachine Shaft Supported on Foil Air Bearings," STLE Tribol. Trans. **47**, pp. 508-516.

[5] Salehi, M., Swanson, E., and Heshmat, H., 2001, "Thermal Features of Compliant Foil Bearings – Theory and Experiments," ASME J. Tribol., **123**, pp. 566-571.

[6] Feng, K., and Kaneko, S., 2008, "A Study of Thermohydrodynamic Features of Multiwound Foil Bearing Using Lobatto Point Quadrature," ASME Paper No. GT2008-50110.

[7] Iordanoff, I., 1999, "Analysis of an Aerodynamic Compliant Foil Thrust Bearing: Method for a Rapid Design," J. Tribol., **121**, pp. 816-822.

[8] Air Properties, http://www.engineeringtoolbox.com/air-properties-d_156.html, Accessed February 13, 2008.

[9] Inconel 718, http://www.espimetals.com/tech/inconel718.pdf, Accessed February. 12, 2008.

[10] Inconel X-750, http://www.hightempmetals.com/techdata/hitempInconelX750data.php, Accessed February. 12, 2008.

[11] Timoshenko, S. P. and Goodier, J. N., 1970, *Theory of Elasticity*, McGraw-Hill, pp. 80-83.

APPENDIX D. STALL TORQUE, POWER, AND COASTDOWN TIME IN DRIVE MOTOR: NO LOAD CONDITION

Figure D.1 depicts a schematic view of the setup to estimate the motor stall torque at no load condition. An ad-hoc device, a simple balanced lever, is affixed on one end of the motor shaft. While power to the motor controller (drive) turns on with a fixed set frequency (varying from 10~60 Hz with 5 Hz increments), the *holding* torque is measured by adding known weights at one end of a balance lever. Hence, the equivalent torque is $D \times F$, i.e., (distance between the motor shaft center and one end of a balance lever, D) × (force from added weight, $F = m \times g$). Note that the maximum *holding torque* is regarded as the *stall torque* of the motor. Figure D.2 shows the estimated motor stall torque versus the motor controller frequency. The figure also depicts the current from the motor controller versus frequency.

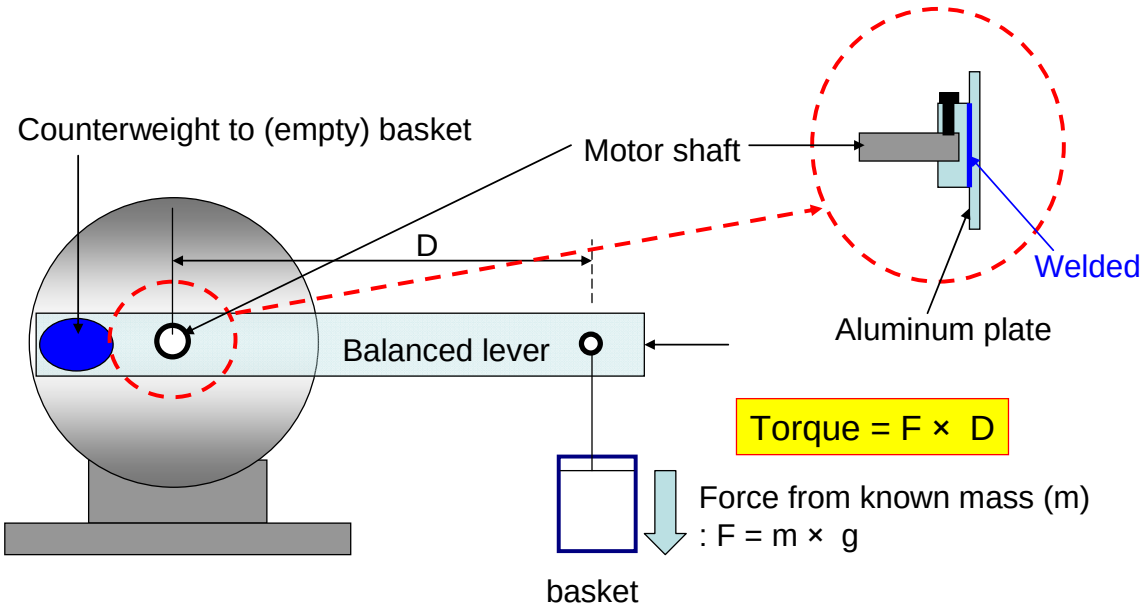

Fig. D.1 Schematic view of test setup to measure stall torque in drive motor

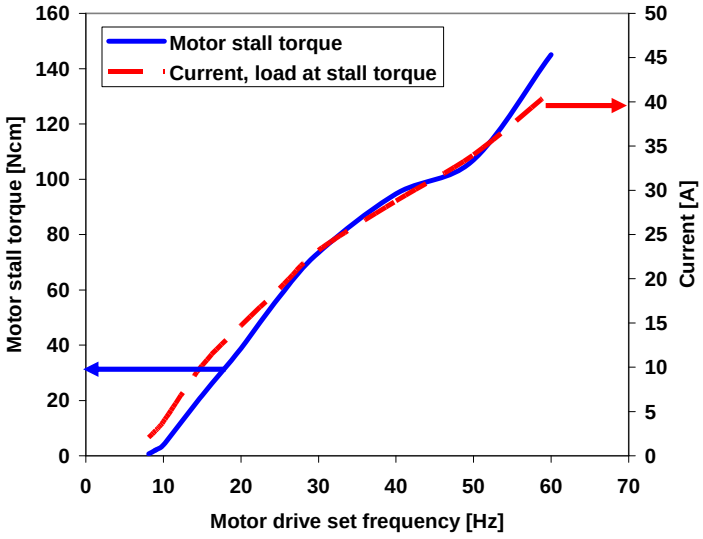

Fig. D.2 Motor stall torque and current versus drive set frequency. No load condition.

While operating the motor, the motor drive displays the current inverter operating status including output frequency (Ω), output current (A), and output voltage (V). Figure D.3 depicts the recorded output current and voltage of the drive motor (without any load). The current increases abruptly as rotor speed reaches 3 krpm; and steadily raises with speed from 9A to 12A. The drive controller provides a linearly increasing voltage that gives also a linearly increasing motor speed. Figure D.4 shows the calculated electric input power ($P=I\times V$) of the motor drive for increasing motor speed. Input power to the motor is almost linearly with speed increases. The characteristics are typical of an electrical motor.

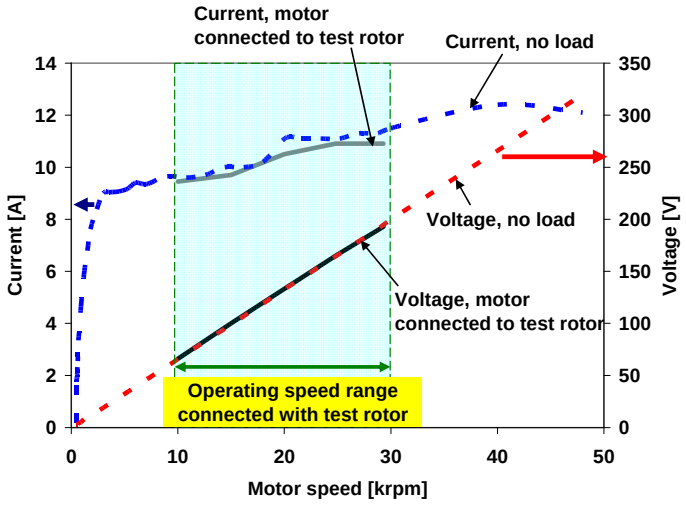

Fig. D.3 Motor drive output current and voltage versus speed with and without connection to test rotor.

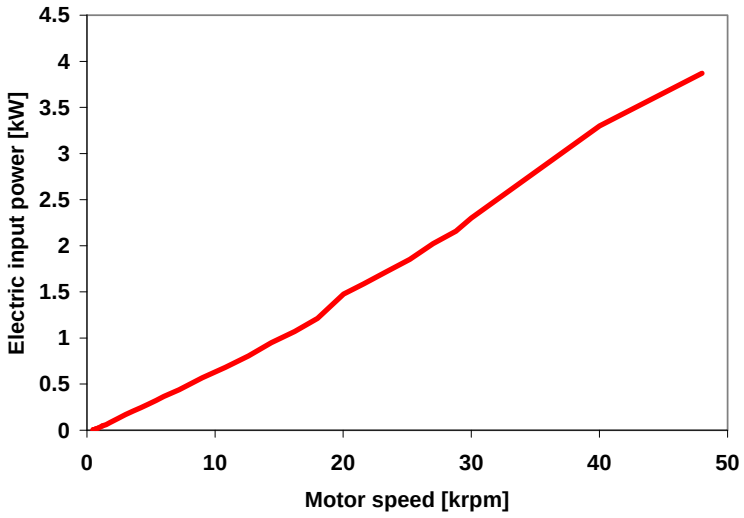

Fig. D.4 Electric input power to drive motor (*P= I×V*) versus motor rotational speed. No load condition.

Figure D.5 shows the recorded coast down speed of the motor versus time for various motor cut-off speeds. Operation is at ambient temperature, ~21ºC, and without a load connected to motor. Note the large coast down time, well beyond 4 minute (270~280 second), for the motor to decelerate to rest from a cut-off speed regardless of motor cut-off speed, i.e., 48, 40, 30, 20 krpm.

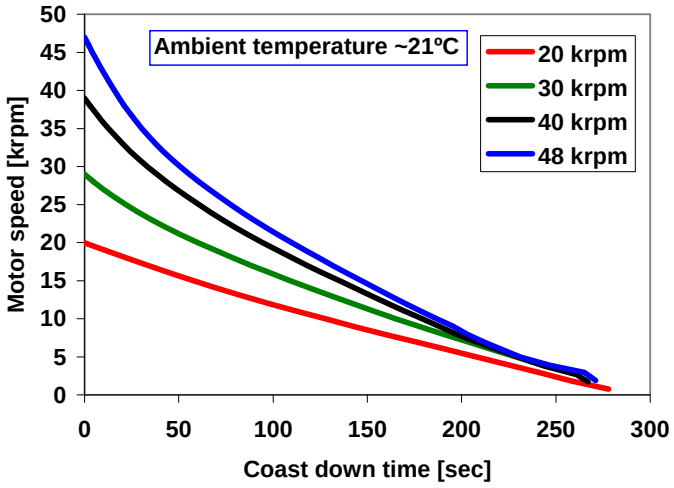

Fig. D.5 Recorded coast down motor shaft speed versus time. Cut-off speeds of 20, 30, 40, 48 krpm. Motor power off after 40 minute operation. Ambient temperature at 21ºC.

APPENDIX E. LATERAL STIFFNESS AND INERTIA OF FLEXIBLE COUPLING

Static load-deflection tests on the flexible coupling aid to measure its stiffnesses. Figure E. 1 shows the measured static load versus coupling displacement coupling. The estimated coupling lateral stiffness is 4421 N/m which is an order of magnitude smaller than the test GFB stiffness coefficients [15.16].

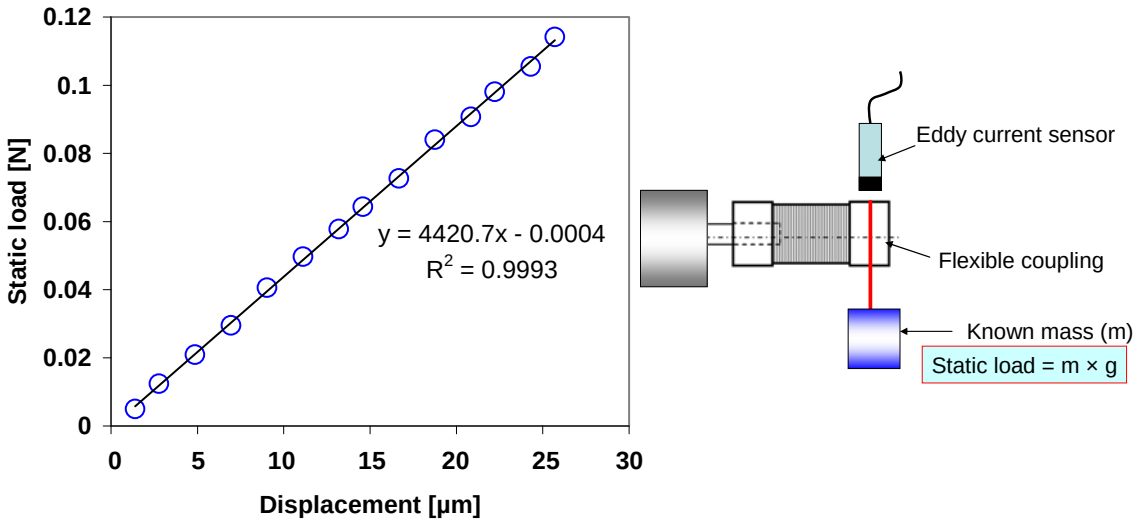

Fig. E.1 Measured flexible coupling displacement versus applied static load. Estimated lateral stiffness of 4421 N/m (uncertainty: 14 N/m).

Mass moments of inertia are derived by measuring the period of natural oscillation *(T)* of the flexible coupling suspended from long strings, as shown in Fig. E.2. The mass moment of inertia, transverse or polar, is

$$I = \frac{mg}{L}\left[\frac{r' T}{2\pi}\right]^2$$

where m is the coupling mass, g is gravitational acceleration, L is the length of the strings, and r' is the distance from the coupling center of rotation to the location where a string hangs. The measured transverse and polar moment of inertias for the flexible coupling are 4.96×10^{-6} kg·m^2 and 2.99×10^{-6} kg·m^2, respectively.

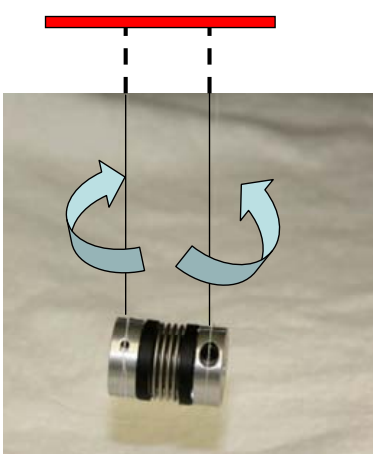

Transverse moment of inertia

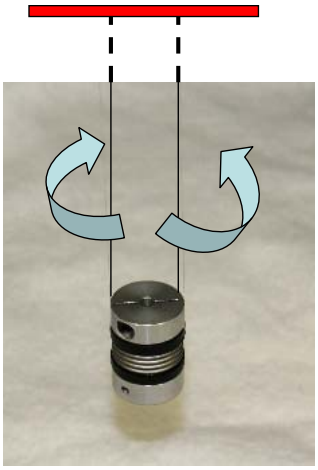

Polar moment of inertia

Fig. E.2 Setup to measure mass moments of inertia: flexible coupling

APPENDIX F. ROTOR OUTER SURFACE TEMPERATURE AT INCREASING HEATER TEMPERATURES: ROTOR OUT OF ITS BEARINGS

The rotor, away from the test rig, hangs from four steel wires. The cartridge heater fits loosely into the hollow portion of the shaft (gap of 4.75mm). The rotor outer surface is exposed to ambient conditions. Temperatures at the rotor OD are recorded for increasingly warmer heater conditions, temperature T_{hs} from 50°C to 400°C with 50°C increments.

Figure F.1 depicts the recorded OD temperatures along the test rotor for increasing heater temperatures (T_{hs}). The figure includes a photograph of the rotor with labels showing the location of the recorded temperatures. To obtain steady state temperature conditions, the heater is powered on during one hour for each heater set temperature (T_{hs}). A high temperature K-type surface probe records the shaft surface temperature. As T_{hs} increases, there is a significant temperature gradient along the rotor axis.

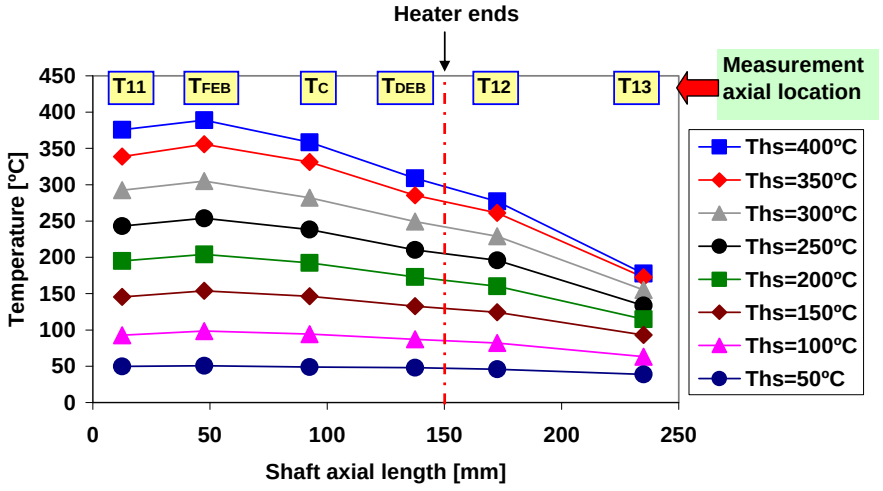

(a) Recorded shaft surface temperatures

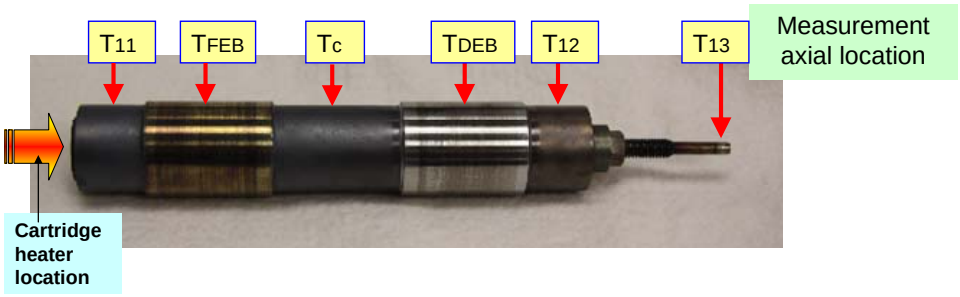

(b) Measurement axial location

Fig. F. 1 (a) Recorded shaft surface temperatures versus axial location for increasing heater set temperature (T_{hs}), and (b) measurement axial locations. Ambient temperature: 21°C.

APPENDIX G. NATURAL FREQUENCIES OF TEST ROTOR ON ITS BEARINGS

Two miniature accelerometers (sensitivity: 5mV/g) are magnetically affixed to the test rig; one on the free end rotor OD, and the other atop either the flexible coupling, Fig. G.1(a), or the connecting rod, Fig. G.2(b). The frequency range (±5%) for the sensors is 1~10k Hz. A thin steel rod delivers impact loads to the system. Figures G.1 and G.2 depict the FFT of the recorded accelerations. The insets in the figures show the locations of the accelerometers and impact application. Within the operating speed of the current test rig (< 30 krpm = 0.5 kHz), the distinctive peak amplitude at 0.48 kHz (= 28.8 krpm) shows the fundamental natural frequency of the test rotor-bearing system.

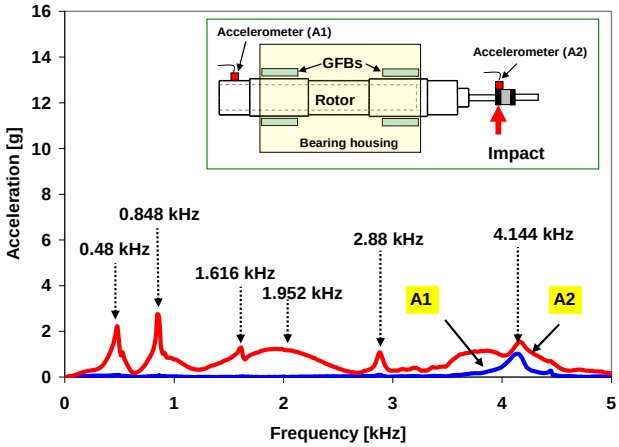

(a) Impact location: flexible coupling, sensor locations: rotor free end (A1) and flexible coupling (A2)

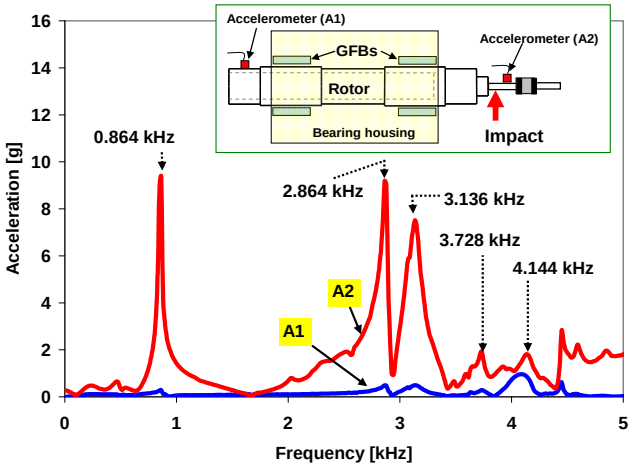

(b) Impact location: connecting rod, sensor locations: rotor free end (A1) and connecting rod (A2)

Fig. G.1 Acceleration spectra at rotor free end and connecting rod due to impact loads on coupling. Uncertainty in frequency: 16 Hz. No shaft rotation. Ambient temperature.

APPENDIX H. TEST CONDITION 4: ROTOR AND BEARINGS STEADY STATE TEMPERATURES

Test condition #		Rotor speed condition	Imbalance conditions	Axial cooling flow conditions	Heater set temperature conditions	Test hours	Rig enclosure
Cond. 4	Rotor imbalance response test (**High temperature**)	Coast down from 30 krpm	Baseline	No cooling	No heating	1h 15'	Open
					100ºC	1h 37'	
					200ºC	1h 40'	
					300ºC	1h 32'	
					360ºC	1h 35'	

For test condition 4, and under thermal steady state conditions, Figure H.1 depicts the temperature raise on the free end (FE) and drive end (DE) rotor surfaces (T_{11} and T_{12}) and at the FE and DE bearing cartridges (T_1 and T_6) versus heater temperature (T_{hs}). Note that the test condition represents no axial cooling flow and the rotor is at its baseline imbalance. Test conditions 5 and 6 (not shown in the figure) show almost the same temperature raise as test condition 4, i.e., there is no notable difference in steady state temperature among test conditions 4-6.

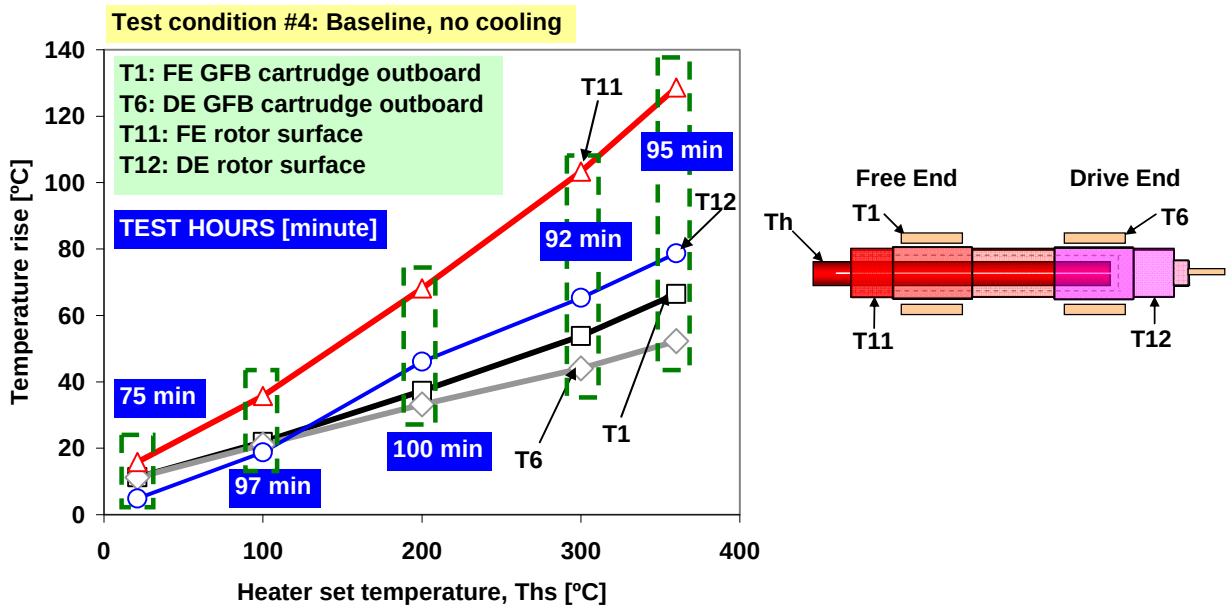

Fig. H.1 Test condition 4: Temperature raise on FE and DE rotor surface and FE and DE FB cartridges versus heater set temperature. Rotor speed of 29.3 krpm.

The measurements evidence the remarkable temperature gradient along the rotor. Incidentally, the rotor temperature is much colder than the heater set temperature. The measurements reproduce conditions found in for example turbocharger rotors.

APPENDIX I. BREAKAWAY TORQUE OF ROTOR ON TEST BEARINGS AT INCREASING SHAFT TEMPERATURES

The breakaway torque of the test rotor supported on the GFBs is determined using a similar approach as in with the measurement of motor stall torque (no load) detailed in Appendix D. Presently, the measurements are conducted while the system is at thermal equilibrium for various increasing set heater temperatures. The motor is not connected to the test rotor

Figure I.1 depicts the estimated breakaway torque of the rotor on the GFBs versus the cartridge heater temperature (T_{hs}). The figure also depicts the temperature raises at the rotor surface on the free end (FE) and drive end (DE), (T_{11} and T_{12}), and the FE and DE bearing cartridges (T_1 and T_6). The rotor break away torque increases with heater temperature. Note that the torque is, with excellent confidence, a quadratic function of the heater temperature (T_{hs}) (R^2~0.999).

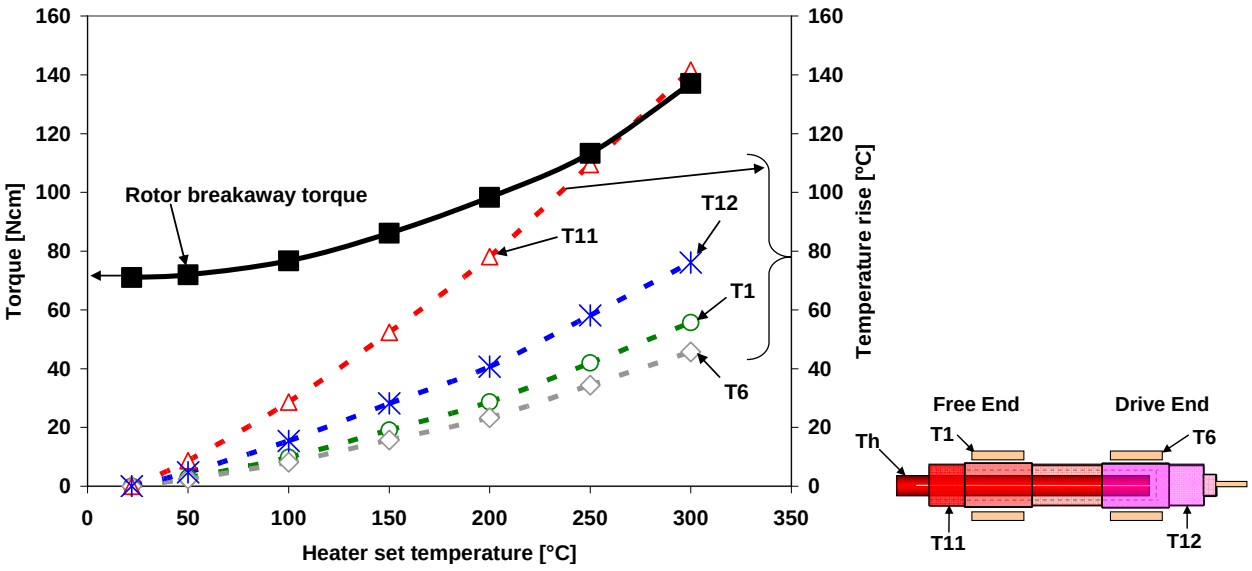

Fig. I.1 Test rotor breakaway torque versus heater set temperature Uncertainty: 0.012 N-cm. Ambient temperature: 22°C. (FE & DE rotor and bearing temperatures included).

APPENDIX J: PREDICTED SYNCHRONOUS STIFFNESS AND DAMPING COEFFICIENTS FOR FREE END GFB

Figures J.1 and J.2 present the predicted synchronous stiffness and damping coefficients versus rotor speed for the free end GFB at increasing cartridge heater temperature up to 360 °C.

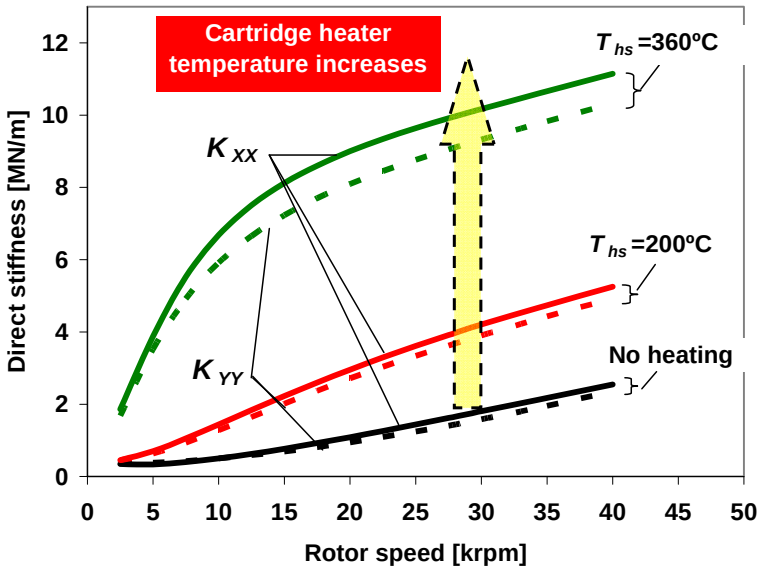

(a) Direct stiffness

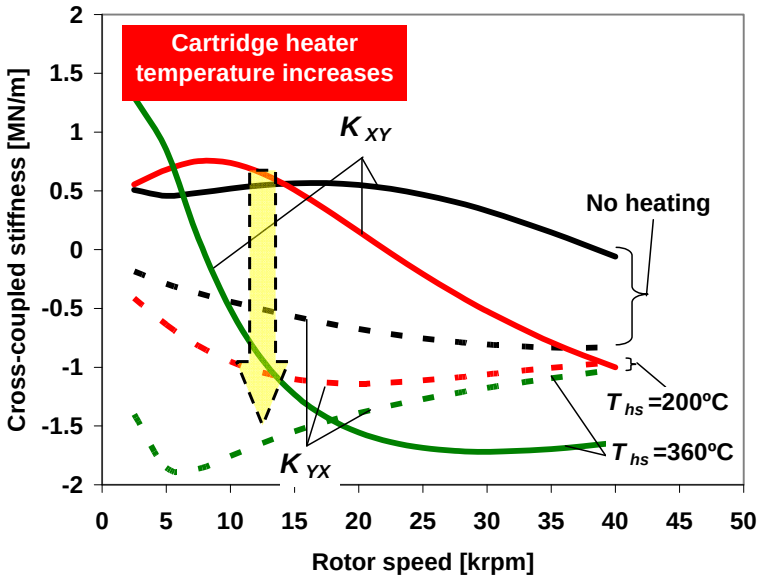

(b) Cross-coupled stiffness

Fig. J.1 (a) Direct stiffness and (b) cross-coupled stiffness for free end GFB versus rotor speed for operation at ambient condition (no heating) and with cartridge heater set temperature (T_{hs}) at 200°C and 360°C. Static load 3.6 N. No forced cooling flow.

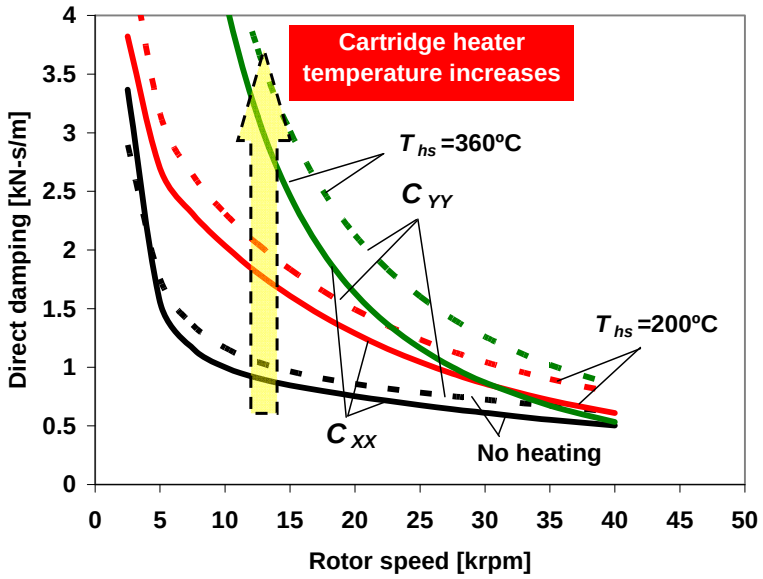

(a) Direct damping

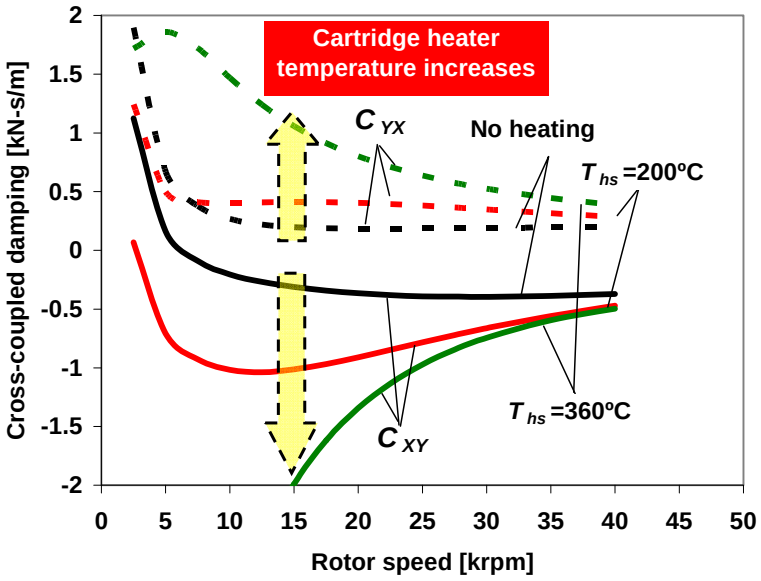

(b) Cross-coupled damping

Fig. J.2 (a) Direct damping and (b) cross-coupled damping for free end GFB versus rotor speed for operation at ambient condition (no heating) and with cartridge heater set temperature (T_{hs}) at 200 °C and 360 °C. Static load 3.6 N. No forced cooling flow.

APPENDIX K: TOP FOIL TEMPERATURE FOR OPERATION WITH COOLING FLOW: PREDICTIONS AND TEST DATA IN SALEHI ET AL. [1]

Salehi et al. [1] report measurements of temperature in a III generation GFB for a number of operating conditions, including changes in static load, rotor speed, and cooing air flow rate. Ambient temperature is~21°C. In the tests, K-type thermocouples record *bearing* temperatures on the outer surface (back) of the top foil. The test GFB has axial length L=75 mm and diameter D=100 mm. The bearing radial clearance is estimated at ~100 μm, after subtracting the journal sleeve deformation due to interference fit with the shaft core. Table K.1 details the dimensions and materials for the bearing cartridge, top foil and bump strip layer, and gas operating conditions. The table notes either a source or a experienced assumption for each parameter listed.

Table K.1. Geometry and operating conditions of GFB and solid shaft [1]

Parameters*	Value	comment
Bearing cartridge and shaft (Inconel 718, assumed)		
Bearing inner radius, $R_{B_i}=D/2$	50 mm	Ref. [1]
Bearing length, L	75 mm	Ref. [1]
Bearing thickness, t_B	20 mm	assumed
Nominal radial clearance, c	100 μm	Ref. [1]
Top foil and bump strip layer (Inconel X750, assumed)		
Top foil thickness, Δ_{t_F}	127 μm	assumed
Bump foil thickness, Δ_{t_B}	127 μm	assumed
Bump half length, l_B	1.27 mm	assumed
Bump pitch, s_0	3.125 mm	assumed
Bump height, Δ_B	0.63 mm	Ref. [1]
Number of bumps, N_b × strips, N_s	100 x 1	assumed
Bump foil Young's modulus, E	207 GPa	Assumed
Bump foil Poisson's ratio, ν	0.28	Assumed
Air properties at 294.3 K (21 °C) and ambient pressure, P_a =1 bar		
Gas Constant, $\Re_g$	287 J/(kg-K)	
Density, ρ	1.164 kg/m^3	
Viscosity, μ	$(4\times10^{-8}\,T+5\times10^{-6})$ Pa-s	
	1.82×10^{-5} Pa-s at 294.3 K	
Conductivity, κ	$(7.0\times10^{-5}\,T+0.0042)$ W/(m-K)	
	0.0257 W/(m-K) at 294.3 K	
Specific heat, c_p	$(0.0996\,T+1009.3)$ J/(kg-K)	
	1,020 J/(kg-K) at 294.3 K	

* Reference [2] details material properties for air. Reference [3] details material properties for Inconel 718 bearing cartridge and shaft and Inconel X750 top foil and bump strip layer.

Note that Ref. [1] does not give complete information on the materials and geometry of neither the test bearing, nor the cartridge, nor the rotor.

Table K.2 shows the THD model predictions of GFB static load parameters and temperature raise for eight test cases reported in Ref. [1]. In the predictions, the operating clearance is determined from thermal changes in the material properties and the components' thermal and centrifugal growths. A thermal mixing parameter λ=0.65 [4] represents the thermal energy mixing with replenishment of fresh gas at the leading edge (Θ_l) of the top foil. Cooling air and ambient temperature ($T_{Co}=T_\infty$) at 274.3 K (21 °C) are assumed.

Figure K.1 presents a comparison of the predicted (back of) top foil temperature and measurements in Ref. [1] for the test cases listed in Table 2. In general, the predicted top foil temperature agrees well with the test data for the broad ranges of rotor speeds, static loads, and cooling flow rates. Note that test data without a cooling gas stream is not provided in Ref. [1].

Table K.2. Thermohydrodynamic model predictions of static load performance and peak film and top foil temperature raises for test GFB [1]

Case No.	Speed (krpm)	Load (N)	Cooling air (L/min)	Journal eccentricity (μm)	Attitude angle (deg)	Minimum film thickness (μm)	Centrifugal growth (μm)	Net thermal growth (μm)	Peak film temp raise (° C)	Top foil temp raise (° C)
1	15	418	500	89.0	13.8	7.9	2.1	2.3	38.7	22.6
2	15	667	510	92.9	9.8	4.4	2.2	3.4	56.7	33.1
3	20	386	700	83.3	16.8	11.34	3.7	2.5	44.5	23.5
4	20	760	1130	90.9	10.2	5.2	3.7	3.4	76.7	33.8
5	25	462	1000	80.5	17.0	11.6	5.8	3.1	61.6	28.8
6	25	1020	1200	88.7	9.4	4.6	5.8	5.4	116.3	50.7
7	30	1005	1330	82.9	10.75	6.1	8.4	6.4	132.4	56.2
8	30	1334	1360	86.0	8.7	3.9	8.4	7.7	162.2	68.3

APPENDIX L. MEASURED SHAFT DEFLECTIONS FOR INCREASING APPLIED STATIC LOADS

Figure L.1 depicts the measured shaft deflections for increasing static loads. In these measurements, the test bearing is removed from the shaft and the load cell directly pushes the shaft OD while the installed eddy current displacement sensor measures the corresponding shaft deflection. The representative (overall) stiffnesses[1] of the test shafts for configurations 1 through 3 are 23.3 MN/m, 8.75 MN/m, and 16.5 MN/m, respectively. The shaft stiffnesses obtained, in particular for configurations 1 and 2, are significantly larger than the experimentally derived FB stiffnesses. Not so for the bearing with a large preload (configuration 3).

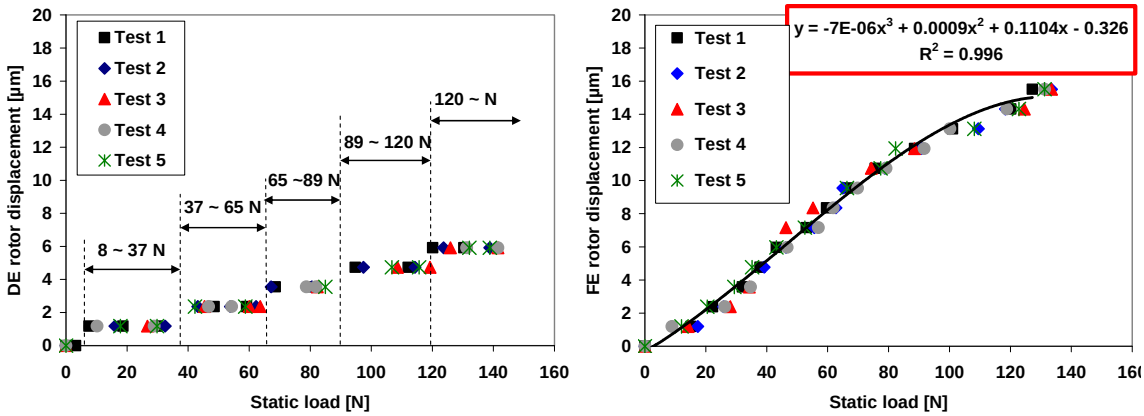

(a) Shaft in configuration 1 (b) Shaft in configuration 2

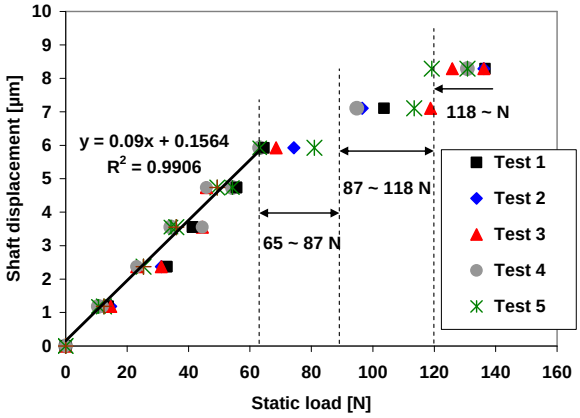

(c) Shaft in configuration 3

Fig. L.1 Measured shaft deflections versus static load (Shafts for configurations 1-3)

[1] The representative shaft stiffness is calculated from (maximum static load)/(maximum displacement), i.e., ~140N/6µm, ~140N/16µm, and ~140N/8.5 µm for test configurations 1 through 3, respectively.

APPENDIX M. SPECIFICATIONS AND COST OF EQUIPMENT AND INSTRUMENTATION

Table M.1 Specifications and cost of equipment and instrumentation – high temperature rotor GFB test rig

Item	Specification	Vendor	Model #	Total cost	Delivery
Fiber optic displacement sensor	Tip up to 482°C, cable up to 340°C, sensitivity 2.2mV/μm($1,820×7)	Philtec	RC60-C1T2T9	$12,740	Dec. 07
Infrared thermometer + accessory (mount & laser sighting viewer)	Up to 1370°C, D/S Ratio 68:1, 5Vdc output, adjustable emissivity ($550×2) + $295	OMEGA	OS552-V1-1	$1,295	Dec. 07
Portable infrared thermometer	Up to 538°C, adjustable emissivity	OMEGA	OSXL653,	$100	Dec. 07
Infrared thermo gun		OMEGA	OS423-LS	$148	01/05/08
Thermocouple (K type)	Up to 1090°C, ceramic insulation with Inconel Overbraid ($54×7)	OMEGA	XCIB-K-2-5-10	$378	Jan. 08, Jan. 09
Thermocouple indicator	Up to 1090°C, resolution 0.6°C($195×6)	OMEGA	DP116-KF1	$1,170	Jan. 08
Heater controller	Programmable 1/8 DIN digital panel meter	OMEGA	CNi853	$310	Jan. 08
High temperature foil bearing	1.44" diameter and 1.1" length (with High temperature coating) (2,500×2)	Miti	2nd generation	$5,000	Apr. 08
XY Table with encoder and two axis readout	Travel: 3" X 3" (with encoders) Resolution: 1μm	Velmex	AXY4009 W1	$ 3,753	Mar. 08
High speed motor	9.5kW at 65krpm	KAES	MOO1C80905	$4,000	Jul. 08
High speed shipping (Intl)	DHL shipping	DHL Express (USA)		$353.34	Aug. 08
Thermocouple (K type)+ Miniature Thermocouple Connectors Flat Pin	Up to 480°C, glass braid insulation ($58×4) ($2.25×6, pin)	OMEGA	5SC-GG-K-30-36, SMPW-K-F	$245.5	Apr. 08, Jan. 09
Insulated thermocouple wire	30m type K duplex insulated wire	OMEGA	PR-K-24-SLE-100	$56	Jan. 09
Cartridge heater	Max. 1.6 kW with 240V	OMEGA	CSH-4101600/240	$76.44	Jul, 08
Cartridge heater	Max. 1 kW with 240V	Thermal Solutions Controls & Indicators	N7A16-10586	$80	Aug. 07
Ceramic fiber paper	Up to 1,200°C	Refractories Incorporated	Kaowool 500	$300	Nov. 07
Hose/connector+AC adapter for flow meter	Air hose and universal AC adapter	Bryan hose and gasket, best buy		$53	May, 08
Steel plate	Cover for instrumentation case 1/8"x4'x8' Smooth Plate cut to length	Mack Bolt and Steel		$150	Jun. 08
Spindle drive	Power source for motor, input 380~480V, 3 phase, 50/60Hz	GMN	90-00124-8048-0000	$4,740	Jul. 08
Heater wire, fuse, switch	Aluminum box, fuse holder and connection, fuse, switch	Mid-State Electronic Supply, McMaster		$159.5	Feb. 08, Jun. 08
Flexible Coupling	Rated torque 1.0 N-m, torsional stiffness 320 N-m/rad($160×3)	R+W coupling technology	MK2/10/33	$480	Sep. 07
Water jet well pump, fittings, hoses	¾ HP, 78 psi, 57L/min	Home Depot	Flotec FP4022	$438.15	Jan. 09
Digital gas mass flow meter, power supply	Max. 500L/min, accuracy ±1.5% of full scale	OMEGA	FMA1844, FMA178PW	$1080	Feb. 09
Socket set screw	Imbalance mass 4-40, ½ length	Ace Bolt &		$4.57	Dec. 08

		Screw Co.			
Step clamp, adjustable height step block	Fixture of heater and bearing support housing	McMaster-Carr	4999A31, 5002A2	$76.17	Dec. 08
Fittings	Connection of gas flow meter	Botco		$4.52	Feb. 09
Power supply	Power of infrared thermometer, 90-264VAC, 24VDC output	OMEGA	PSR-24S	$120	Feb. 09
Reflective tape	For optical tachometer, 1.5m roll, 12 mm wide	OMEGA	HHT-RT-5	$13	Jan. 09
Surface probe	6” length, 1/8” dia.	OMEGA	SPHT-K-6	$45	Jan. 09
Tools	Test rig assembly and maintenance	Harbor freight tools		$257.77	Jan. 09
Switch box, wires	Power system of water pump	Mid-State Electronic Supply, Inc.		$52.47	Jan. 09
Super glue, tape, gloves	Fixture of reflective tape, holding high temperature shaft	Home Depot		$8.78 +$22.53	Jan. 09, Feb. 09
Cost to NASA GRC			Total:	**$37,733.11**	
Shaft + Ni-Cr coating	1.44” diameter (with HT coating)	KIST	High speed rotor	$0 ×1	Dec. 08
High temperature foil bearing	1.44” diameter and 1.1” length	KIST	1st generation	$0 ×4	Dec. 08
Foil bearings repair	1.5” diameter and length (without coating)	Foster Miller Tech.	2nd generation	$3,000 (1,500×2)	Nov. 07
Benchtop thermometer	10-channel benchtop thermometer, dedicated thermocouple input with analog	OMEGA	MDSSi8A-TC	$520×1	Jun. 08
Spindle drive power	Install 480 Volt, 30, 50AMP Power	Texas A&M University	Room134	$465	Aug. 08
Cost other source	(PI incentive)		Total:	**$3,985**	
Hollow shaft	For Miti GFB rotordynamic tests	Vilas Motor Works		$890	Jan. 09
Solid shaft, bearing housing	For KIST GFB static and dynamic load tests.	Vilas Motor Works		$635	Feb. 09
Water tank	65Gallon plastic water tank	Tractor Supply, Co.	Room134	$126	Aug. 09
Paid with TRC resources			Total:	**$1,651**	
Total cost				**$43,369.1**	